Doctoral Dissertation

Development of ICP-etched Scanning Nitrogen-Vacancy Center Probes for Local Magnetic Imaging

Wang Yifei

Supervisor: Toshu An

Graduate School of Advanced Science and Technology

Japan Advanced Institute of Science and Technology

(Materials Science)

June 2025

Abstract

In recent years, the nitrogen-vacancy (NV) centers in diamonds have been studied by a large number of researchers for their quantum properties. The spin states in the negatively charged NV can be excited by a laser to generate fluorescence and their magnetic resonances split by the external magnetic fields are detected via the optically detected magnetic resonance (ODMR). Therefore, the NV center can be used as a probe to measure stray magnetic fields from magnetic materials and to elucidate magnetic structures. Compared to other magnetometers, the NV center magnetometer is becoming increasingly used due to its high sensitivity and nanoscale spatial resolution.

In this research, the $^{14}N^{+}$ implanted diamond was fabricated via a focused ion beam (FIB) and attached to a quartz tuning fork as a scanning NV center probe with a diameter down to about 500 nanometers. Furthermore, to increase the performance of the fabricated probe, the inductively coupled plasma (ICP) etching was considered to be applied to the probe. We did the ICP etching on the probe for a few tens of nanometers, then measured the Rabi oscillation and spin coherence properties before and after the ICP etching process to evaluate the performance of the probe.

The fabricated scanning NV probe combined with an atomic force microscopy (AFM) was used to detect the stray fields from the magnetic samples, such as Bismuth Lutetium iron garnet (BLG) and Yttrium iron garnet (YIG). The magnetic structures (magnetic domains) from these magnetic samples can be monitored by the magneto-optic Kerr effect (MOKE) microscope and imaged by the fabricated NV-AFM system. Moreover, the bubble-shaped magnetic domains (bubble domains) from the magnetic samples were formed by applying external fields. This kind of domain from low-field magnetic samples could not be imaged by the fabricated probe clearly unless increasing the performance of the probe, for example, via the ICP etching process with around 25 nm.

In a word, this research focuses on the development of a high-performance scanning NV center probe in order that we can detect and image the stray field from the magnetic samples.

Keywords: NV center, scanning probes, focused ion beam, ICP etching, spin properties, magnetic samples, stray fields, magnetic domains

Contents

List of figures

Chapter 1
Introduction

1.1 Background

Over the past few decades, scanning probe sensing techniques have undergone significant development and have been extensively applied to the detection and imaging of magnetic samples. These techniques have played a crucial role in nanoscale characterization, allowing researchers to investigate material properties with high spatial resolution [1] [2]. Various microscopy techniques, such as atomic force microscopy (AFM) [3] [4], scanning tunneling microscopy (STM) [5], magnetic force microscopy (MFM) [6], and superconducting quantum interference device (SQUID) [7] microscopy, have been developed and integrated with scanning probes to enhance their detection capabilities. These advancements have led to significant improvements in the study of magnetic phenomena at the nanoscale, enabling the observation of intricate magnetic structures and interactions that were previously inaccessible.

Despite their remarkable contributions to magnetic sensing and imaging, traditional scanning probe techniques have inherent limitations that restrict their effectiveness in certain applications. For instance, AFM and STM are widely recognized for their ability to provide high-resolution imaging of surface topography; however, they lack the sensitivity required to detect weak magnetic fields effectively [4] [8]. On the other hand, MFM, while capable of imaging stray magnetic fields, has limitations in detecting certain types of magnetic structures due to its reliance on tip-sample interactions [9]. SQUID microscopy, renowned for its extremely high magnetic sensitivity, suffers from relatively low spatial resolution due to the large size of its superconducting loop. These constraints highlight the need for a new sensing approach that combines both high spatial resolution and high magnetic sensitivity to overcome these limitations [10].

To address these challenges, researchers have turned to nitrogen-vacancy (NV) center probes as a promising solution for high-resolution and high-sensitivity quantum sensing [11] [12] [13] [14]. NV centers are point defects in diamond consisting of a substitutional nitrogen atom adjacent to a carbon vacancy. These defects exhibit exceptional optical and spin properties, making them highly suitable for quantum sensing applications. The ground-state spin levels of NV centers can be manipulated and read out via optically detected magnetic resonance (ODMR), where an external magnetic field causes Zeeman splitting [15] of the spin states. This quantum property enables NV centers to function as highly sensitive magnetometers capable of detecting even extremely weak magnetic fields with nanoscale resolution.

The integration of NV centers with scanning probe techniques has led to the development of scanning NV center probes, which can be used for high-precision imaging of magnetic domains. By attaching NV centers to a quartz tuning fork and combining them with AFM, researchers can bring the NV sensors into close proximity with the sample surface, enabling nanoscale imaging [16]. This technique, often referred to as NV-AFM, has been successfully employed to visualize intricate magnetic structures with unprecedented spatial resolution and sensitivity. For example, magnetic domain structures from various magnetic materials can be observed using the magneto-optic Kerr effect (MOKE) microscope [17] and further imaged with the NV-AFM system [18]. This approach offers a non-invasive and highly sensitive means of probing magnetic phenomena at the nanoscale.

One of the significant advantages of NV-AFM over conventional quantum sensing techniques is its ability to operate under ambient conditions, including room temperature and atmospheric pressure. Unlike other quantum systems that require cryogenic temperatures or vacuum environments to maintain coherence, NV center probes retain their quantum properties in practical experimental settings. This advantage simplifies the experimental setup and broadens the range of applications for NV-based sensing techniques. In particular, the ability to function under ambient conditions makes NV center probes highly attractive for applications in biology, where non-invasive imaging of magnetic nanoparticles and biomarkers is essential for advancing medical diagnostics and therapeutic research.

The versatility of scanning NV center probes extends across multiple scientific disciplines. In physics, they have been employed to study complex magnetic structures such as magnetic domains [19] [20], skyrmions [21], and quantum materials, providing insights into fundamental properties that are difficult to observe using conventional methods. In quantum computing research, NV center probes are utilized for characterizing qubits, identifying noise sources, and assessing decoherence mechanisms at the nanoscale. These capabilities are crucial for the advancement of scalable quantum systems. In the field of biology [22], scanning NV center probes enable high-resolution imaging of magnetic nanoparticles and biomolecules within cells, facilitating the development of innovative magnetic resonance-based diagnostic techniques.

As research in NV center-based quantum sensing continues to progress, efforts are being made to enhance the performance of scanning NV center probes, particularly in terms of spatial resolution and sensitivity. By refining NV center fabrication techniques, improving probe stabilization, and optimizing readout methods, researchers aim to push the boundaries of nanoscale magnetic sensing [23]. The continued development of NV-based quantum sensing technologies is expected to drive new discoveries and technological innovations, opening up exciting possibilities for future applications in materials science, condensed matter physics, and biomedical research.

In this dissertation, we focus on the development and fabrication of scanning NV center probes in-house to overcome the limitations of commercially available probes. A notable

commercial product, the Q-nami probe (Fig. 1.1.(a)), demonstrates excellent performance for magnetic detection [24]. For example, Q. Sun and his group achieved the magnetic domain evolution upon increasing external field (Fig. 1.1.(b)) [25], and A. Finco with his group achieved the skyrmions imaging via the Q-nami probe (Fig. 1.1.(c)) [26].

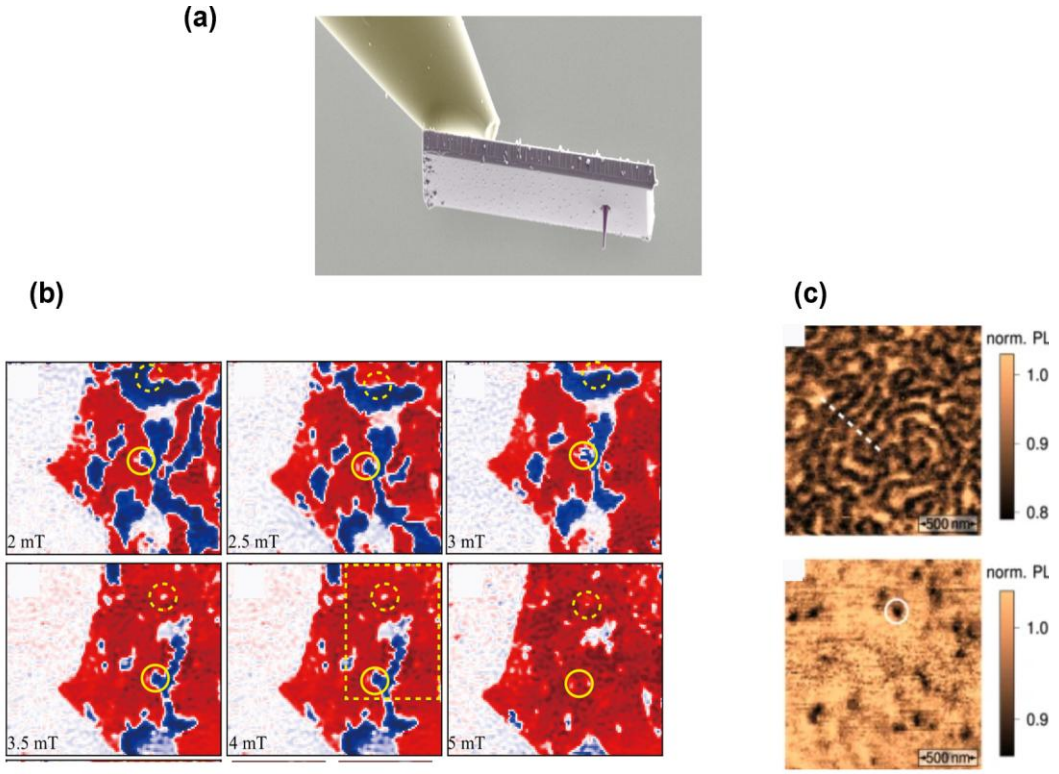

Fig. 1.1.(a) The Q-nami probe from qnami.ch. (b) The magnetic domain evolution upon increasing the external field. (c) PL quenching image of spin state and skyrmions.

However, the Q-nami probe presents challenges such as high costs and long shipping times due to its European origin. To address these issues, we have developed a cost-effective and efficient method for fabricating NV diamond probes using laser cutting and the focused ion beam (FIB) process [27]. Dr. Kainuma, the former member of our laboratory, fabricated a scanning NV center pillar probe with 1.3 μm diameter and imaged the magnetic domains from magnetic tape successfully (Fig. 1.2).

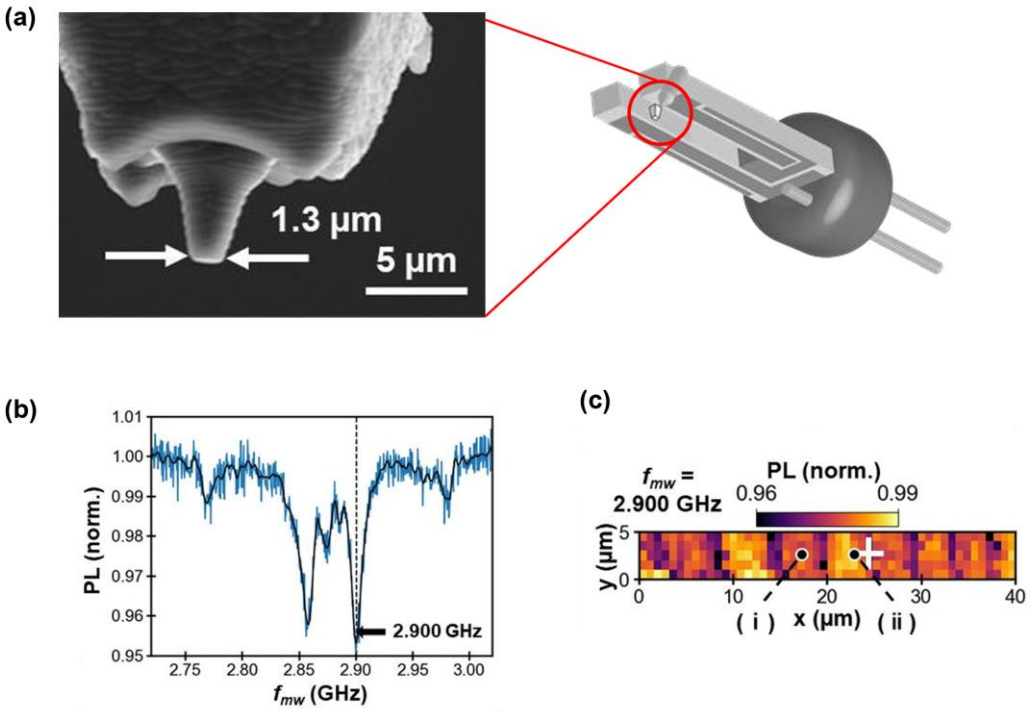

Fig. 1.2.(a) The fabricated scanning NV center probe from Dr. Kainuma. (b) The ODMR spectrum imaged during the AFM scanning. (c) PL image of a magnetic tape imaged by the fabricated scanning NV center probe.

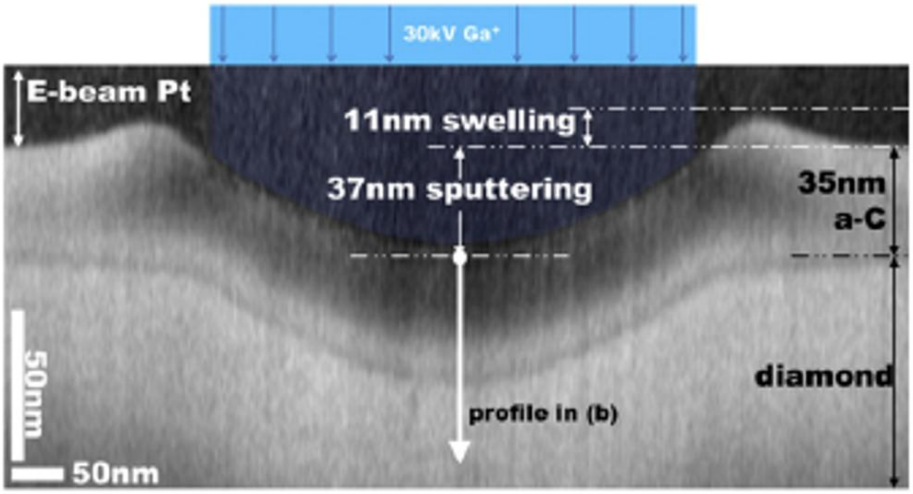

Fig. 1.3. The amorphous carbon residual damage caused by the FIB process.

Our fabricated NV center probes have been successfully employed for imaging magnetic domains in various samples. However, during the FIB milling process, Ga^+ ions induce residual damage and surface defects in the form of amorphous carbon (Fig. 1.3) [28], which degrade the diamond's and NV center's properties and in cases where the magnetic field is weak or the probe performance is suboptimal, the imaging results have been less clear. To enhance the probe's performance, we are currently exploring the use of inductively coupled plasma (ICP) etching [29]to recover and improve the quality of NV diamond tips. This process is expected to refine the probe's sensing capabilities, enabling more precise magnetic domain imaging and expanding the applicability of scanning NV center probes to a wider range of magnetic samples.

Through continued advancements in fabrication and optimization, scanning NV center probes hold the potential to revolutionize nanoscale magnetic sensing and imaging, providing unprecedented insights into the magnetic properties of materials and biological systems. As research progresses, we anticipate that NV center-based quantum sensing will become a cornerstone technology for next-generation scientific discoveries and applications.

1.2 Outline of the dissertation

This dissertation is composed of six chapters, covering the principles of my research, the work I focused on, and the results from my work.

Chapter 2 introduces the concept of the NV, which plays a central role throughout my research. Readers will gain insight into the structure and properties of the NV, as well as its applications within my research, as discussed in the following chapters.

Chapter 3 explains the details of how a diamond can be fabricated into a scanning NV center probe, which can be used for magnetometry. This chapter also introduces a method called ICP etching to increase the performance of the fabricated probe. The performance change of the probe was observed after the ICP etching process.

Chapter 4 shows how the FIB-fabricated NV center diamond will be attached to a quartz tuning fork and combined with AFM as a scanning NV center probe.

Chapter 5 focuses on the application of the fabricated scanning NV center probe. The fabricated probe can be used to image the stray field from the magnetic samples, allowing the obtaining of magnetic domain images from the magnetic samples.

Chapter 6 summarizes the results of my research and discusses the potential future improvements.

Chapter 2
The nitrogen-vacancy (NV) center in diamond

The diamond shows a face-centered cubic (FCC) crystal structure with an arrangement of carbon atoms, where each atom forms four strong covalent bonds with four neighboring carbon atoms [30]. The nitrogen-vacancy (NV) center in a diamond is a defect structure where one carbon is substituted by one nitrogen atom with a neighboring carbon vacancy [31]. From the diagram of the NV structure, it's known that the NV axis could have four directions [111], $[\bar{1}1\bar{1}]$, $[1\bar{1}\bar{1}]$, and $[\bar{1}\bar{1}1]$. The angle between one NV axis and one NC axis is 109.5 ° [32]. In this chapter, we would like to introduce the properties of this unique defect center in diamond.

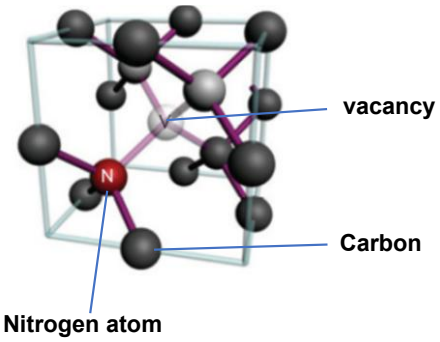

Fig. 2.1. The NV center in a diamond crystal structure. The red ball is the nitrogen atom, the white ball is the carbon vacancy, and the black balls are carbon atoms. The NV is aligning in the [111] direction [58].

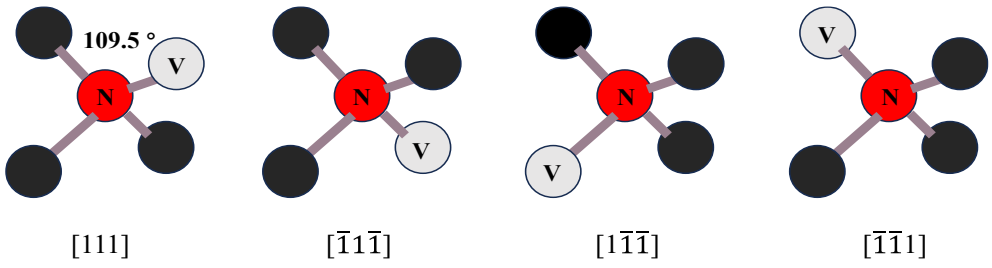

Fig. 2.2. The four directions [111], $[\bar{1}1\bar{1}]$, $[1\bar{1}\bar{1}]$, and $[\bar{1}\bar{1}1]$ of the NV axes.

2.1 Properties of NV center

For the electronic structure of the NV center, the nitrogen atom provides two electrons, and the dangling bonds from the carbon atoms around the vacancy provide three electrons, which make the NV negatively charged as NV^- when they are captured by the lattice. Although there are still neutral and positively charged NV^0 and NV^+ that exist in the NV, the NV^- is widely studied and used due to its stable optical and spin properties and magneto-optically active [33] [34].

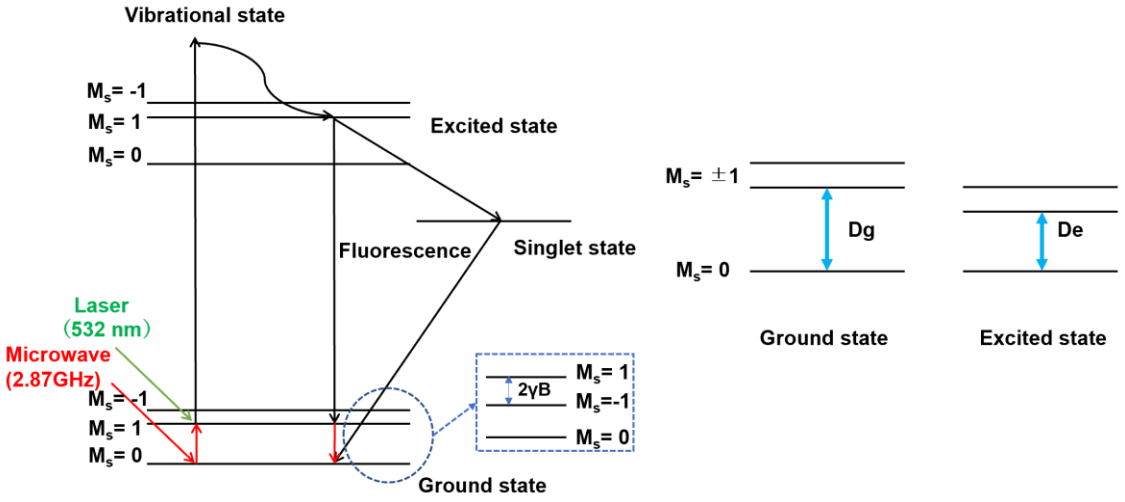

Fig. 2.3. The energy level diagram of NV^- in diamond. It has a triple ground state and a triplet excited state with $m_s = 0$ and $m_s = \pm 1$

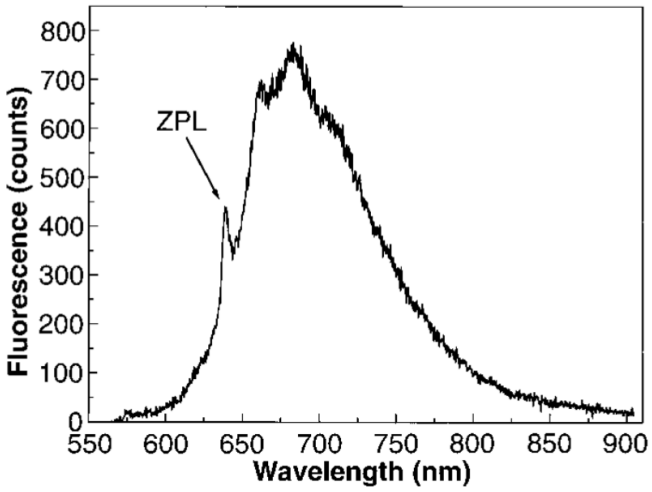

Fig. 2.4. The fluorescence spectrum of the NV center. A small peak can be observed at wavelength 638 called zero phonon line (ZPL) [36].

Fig. 2.3 shows the energy level diagram of the NV^- in diamond. The NV^- center has a symmetry electronic ground state $|g\rangle$ ($^3A_2$) and a symmetry excited state $|e\rangle$ (^3E), both of which are spin-triplet (S = 1) states and separated by 1.945 eV. At zero magnetic field, ground and excited triplet states can be further separated into three spin sub-levels $m_s = 0$ $|0\rangle$ and $m_s = \pm 1$ $|1\rangle$ states by $D_g = 2.87$ GHz and $D_e = 1.42$ GHz respectively, where D is the zero-field splitting [35]. From the Fig. 2.4, we can know that the resonant wavelength of the ground state is 638 nm, which is called the zero-phonon line (ZPL) [36]. This means that the ground state can be excited by light with a wavelength under 638 nm. In this research, we use the laser with a 532 nm wavelength to achieve the excitation.

When the ground state is transitioned to the excited state by irradiation of a 532 nm laser pulse, it emits fluorescence with a wavelength of 632 nm. Then, when the excited $m_s = \pm 1$ state relaxes, it has a probability to relax through a metastable singlet state $|s, {}^1A_1\rangle$ in the relaxation process, with the change of angular momentum due to spin-orbit interaction. Phosphorescence can be detected during this relaxation process because the relaxation is via vibrational modes. Finally, the singlet state relaxes to the ground state $|g, m_s = 0\rangle$ [37].

Although the electron in $|e, m_s = \pm 1\rangle$ state can decay through the metastable singlet state, which is important for the magneto-optic behavior of the NV center, the electron in $|e, m_s = 0\rangle$ state mainly decays by fast radiative transition. Therefore, around 30% optical contrast between $m_s = 0$ and $m_s = \pm 1$ states can be observed. The spin states can be read optically by counting the number of fluorescence photons emitted from excited states [38]. Fig. 2.5 presents a histogram of photon counts for an NV center excited from the $m_s = 0$ and $m_s = \pm 1$ spin states. During the laser pulse irradiating, the photon emission initially shows a sharp peak with the help of rapid radiative transitions, followed by a slower recovery phase due to singlet state decay [39]. This graph illustrates the contrast in fluorescence intensity between the $m_s = 0$ and $m_s = \pm 1$ states.

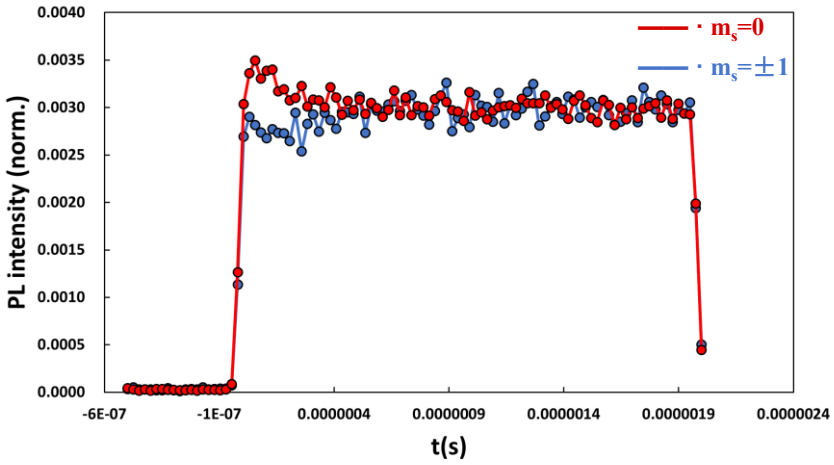

Fig. 2.5. A time-resolved luminescence during a laser pulse. It plots the photon counts from the $m_s = 0$ (red) and $m_s = \pm 1$ (blue) states from the NV center.

2.2 Optically detected magnetic resonance (ODMR)

The optically detected magnetic resonance (ODMR) is a simple and basic technique used to probe the spin states of NV centers by sweeping the microwave field during the relaxation process [40] mentioned in Chapter 2.1. When the frequency of the microwave resonates with the $m_s = \pm 1$ state, the intensity of the fluorescence reduces due to the transition from the $|g, m_s = 0\rangle$ state to $|g, m_s = \pm 1\rangle$ state. Because we can plot the fluorescence intensity as mentioned in Chapter 2.1, by counting the number of fluorescence photons, a significant dip can be observed from the plotted image, which is called the ODMR spectrum (Fig. 2.6).

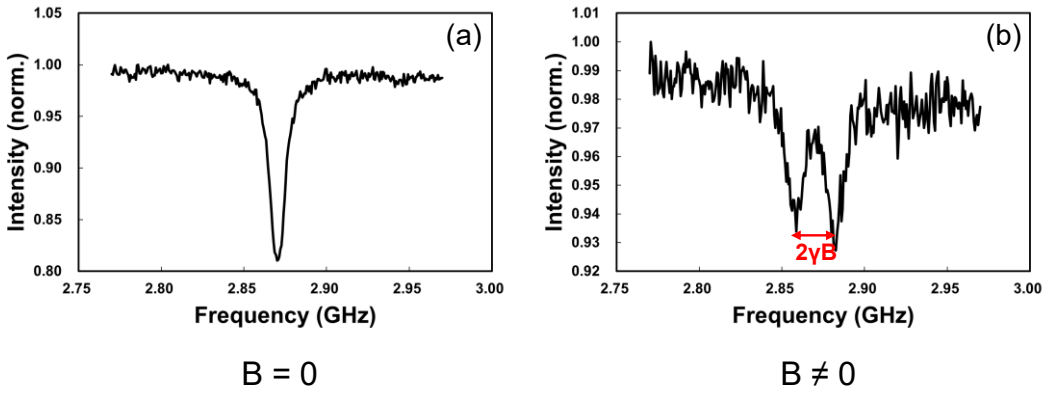

Fig. 2.6. The ODMR spectra. (a) Without an external magnetic field. (b) Applied an extra magnetic field. The frequency separation between two resonances is 2γB.

When an external magnetic field is applied, we can find that one dip from the ODMR spectrum splits into two dips. The reason is that the degeneracy of the magnetic field $m_s = \pm 1$ state is lifted due to the Zeeman effect [41] so that the $m_s = \pm 1$ state splits into two states $m_s = +1$ and $m_s = -1$. This results in resonance transitions for the $m_s = +1$ and $m_s = -1$ states appearing as distinct Lorentzian dips [42] at lower and higher frequencies, respectively, relative to the zero-field splitting of $D_g = 2.87$ GHz. The separation of the two dips' frequency can be defined by $2\gamma B$, where $\gamma = 2\pi \times 28$ GHz/T is the electron gyromagnetic ratio and B is the magnetic field that is parallel to the NV axis [43]. Therefore, when the magnetic field is stronger, we can observe the broader separation of the resonance frequencies from the ODMR spectrum.

We can use the NV center spin Hamiltonian to explain the relation between the spin state and the magnetic field, which is defined by [44]:

$$\frac{H}{h} = DS_z^2 + \gamma \mathbf{B} \cdot \mathbf{S} + E \cdot (S_x^2 - S_y^2) \tag{2.1}$$

Where D = 2.87 GHz is the zero-field splitting, S is the NV electron spin (S_x, S_y, and S_z

are Pauli matrices [45], γ is the electron gyromagnetic ratio [46], B is the magnetic field that is parallel to the NV axis, and E is the strain field. Therefore, changes in the external field and parameters will be measured and influence the Hamiltonian. Moreover, not only the magnetic field but also some other perturbations such as temperature, strain, and pressure can vary the D parameters, so that the NV spin can detect the changes in them [47] [48] [49].

According to the properties mentioned above, the NV center is sensitive to the external magnetic field and thus can be used as a sensing tool to detect the weak external magnetic field with high sensitivity and spatial resolution [50].

2.3 Rabi oscillation

As mentioned in Chapter 2.2, the NV spins can transition between the $m_s = 0$ and $m_s = \pm 1$ states while applying a microwave at the resonance frequency. And if the $m_s = \pm 1$ states split to $m_s = +1$ and $m_s = -1$ states by an external magnetic field, the electrons will reach the $m_s = +1$ or $m_s = -1$ state from the $m_s = 0$ state, then go back to the $m_s = 0$ state, which is called two level system. We can visualize this two-level system by using the Bloch sphere (Fig. 2.7) [51].

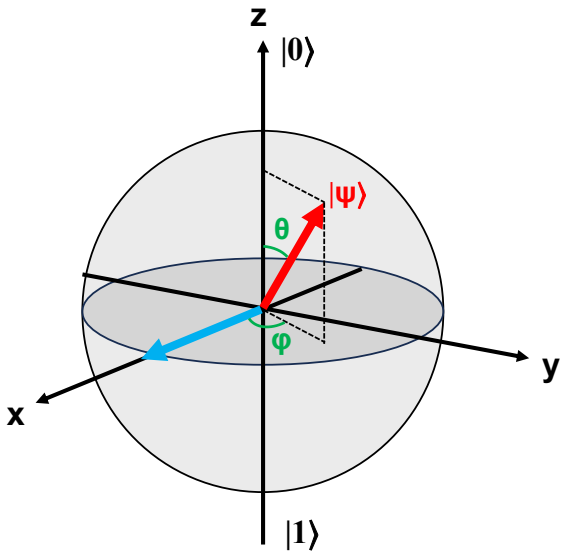

Fig. 2.7. The Bloch sphere for NV state. The $|0\rangle$ state is on up side and the $|1\rangle$ state is on down side. The red arrow represents the spin state with angle θ to the z axis and angle φ to the y axis. The blue arrow represents the microwave field.

The Bloch sphere is a geometrical representation of the state of a two-level quantum system as points on the surface of a sphere. A rotating frame of reference can be understood as a stationary coordinate system relative to a frame rotating around the z-axis

with a specified frequency ω. The up pole represents the $|0\rangle$ ($m_s = 0$) level, while the down pole represents the $|1\rangle$ ($m_s = +1$ or $m_s = -1$) level. One general state $|\psi\rangle$ between these two levels can be defined as [52]:

$$\Psi = \alpha|0\rangle + \beta|1\rangle \tag{2.2}$$

with complex coefficients α and β, and the normalization constraint requires the $|\alpha|^2 + |\beta|^2 = 1$. In order to express the state in polar coordinates, the x, y, and z axes can be defined by:

$$x = r\sin\theta\cos\varphi;\ y = r\sin\theta\sin\varphi;\ z = r\cos\theta \tag{2.3}$$

where r is the radius of the sphere, θ is the angle of rotation, and φ is the phase. Therefore, we can define the $|\psi\rangle$ as:

$$\Psi = \cos\left(\frac{\theta}{2}\right)|0\rangle + e^{i\varphi}\sin\left(\frac{\theta}{2}\right)|1\rangle \tag{2.4}$$

where $\theta \in (0, \pi)$ and $\varphi \in (0, 2\pi)$. And the magnetic field B with a frequency ω is pointing along the x-axis.

When we apply a continuous resonant microwave pulse to the NV spins, an oscillation occurs between the $|0\rangle$ and $|1\rangle$, which is called Rabi oscillation [53]. The probability P (t) of the state during the transition can be defined via Rabi oscillation frequency $\Omega_R = \sqrt{(\omega - \omega_0)^2 + \omega_x^2}$ as [54]:

$$P(t) = \left(\frac{\omega_x}{\Omega_R}\right)^2 \sin^2\left(\frac{\Omega_R t}{2}\right) \tag{2.5}$$

where the ω_0 and ω_x are the frequencies from the magnetic field **B**. We can calculate the Rabi oscillation from the probability P (t) of the $m_s = 0$ state.

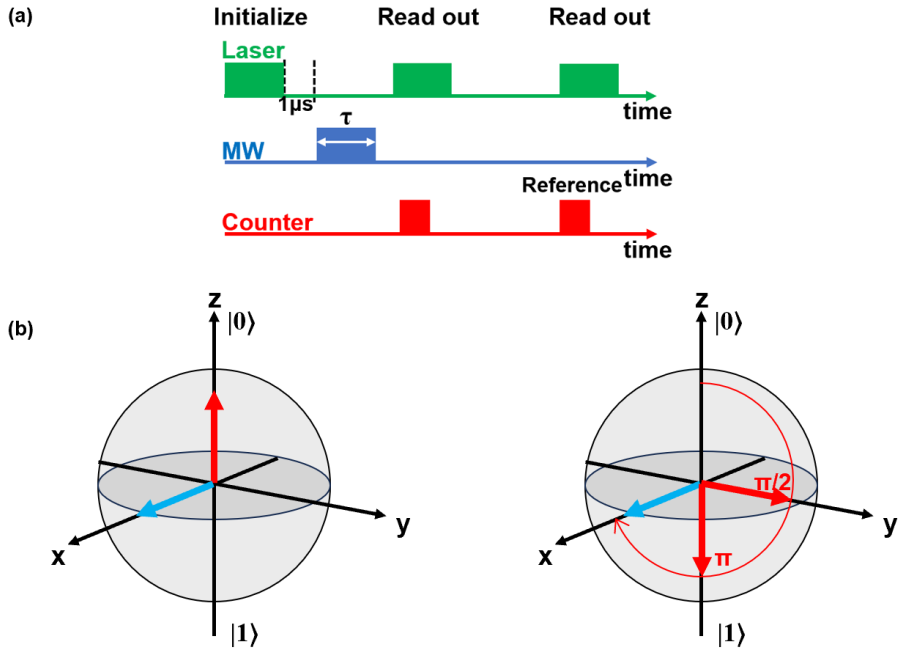

Fig. 2.8. (a) Sequence for Rabi oscillation measurement. (b) Bloch sphere of NV spin. Left is the initial condition at $m_s = 0$, and right is that the spin rotates for π/2 and π pulse.

The Rabi oscillation can be detected and plotted via a laser pulse by counting the electrons from the state [55]. In our research, we initialize the NV spin by the laser pulse so that it is polarized at $m_s = 0$. Then, with the applying of pulsed microwave with a duration τ at resonant frequency, we can read out the counts of fluorescence by irradiating the laser pulse again (Fig. 2.8 (a)). The second counter was set as a reference. During this measurement, we can understand from the Bloch sphere that the spin at $|0\rangle$ can be flipped to $|1\rangle$ by the microwave for a duration, which is called π pulse (Fig. 2.8 (b)) [56]. We can decide the π pulse through the Rabi oscillation spectrum plotted after the measurement (Fig. 2.9). The Rabi oscillation frequency Ω_R is proportional to the microwave power, therefore, we can change the π pulse by adjusting the microwave power. If we apply a half π pulse (π/2) to the spin state, it will reach the superposition between the $|0\rangle$ and $|1\rangle$ state at $(|0\rangle + |1\rangle)/\sqrt{2}$ [57].

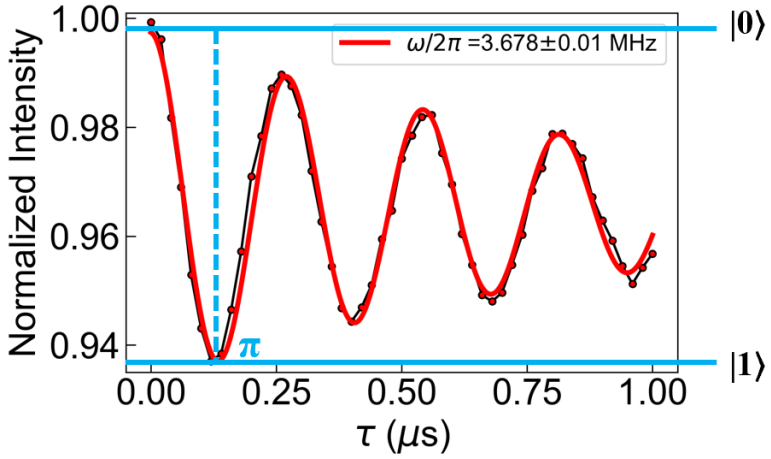

Fig. 2.9. The Rabi oscillation spectrum shows the oscillation between the $|0\rangle$ and $|1\rangle$. The π pulse can be determined from the frequency as 0.156 μs.

2.4 Decoherence and relaxometry measurements

The NV center spin is known to have a long coherence time up to milliseconds at room temperature [58]. However, with the influence of noise, fields, and other perturbations, the spin will lose its coherence, and the time to maintain the coherence is called decoherence [59]. The transition probability P(t) hence decays due to the decoherence, which can be defined during time t as:

$$P(t) = \frac{1}{2}(1 - e^{-\chi(t)}) \tag{2.6}$$

where $\chi(t)$ is the decoherence function [60]. For spin echo that will be introduced later, the decoherence function can be written as [61]:

$$\chi(t) = \frac{2}{\pi}\int_0^{\infty}\gamma^2 S(\omega)\left|\frac{sin^2(\omega t/4)}{\omega/4}\right|^2 d\omega \quad (2.7)$$

where S(ω) is the noise function. The noise function can be defined by the noise signal V(t) as:

$$S(\omega) = \int_{-\infty}^{\infty} e^{-i\omega t}\langle V(t'+t)V(t')\rangle dt \quad (2.8)$$

where t' is the average function time and V(t) is the stochastic signal.

In order to connect the noise function S(ω) with the decoherence decay (relaxation) rate Γ, relaxometry is used as a unique technique. The relaxometry is based on the calculation of the probability between the $|0\rangle$ and $|1\rangle$, and for calculating the probability, we can first expand the stochastic signal V(t) as:

$$V(t) = \frac{1}{2\pi}\int_{-\infty}^{\infty} d\omega\left\{V(\omega)e^{-i\omega t} + V^{\dagger}(\omega)e^{i\omega t}\right\} \quad (2.9)$$

where $V(\omega) = V^{\dagger}(-\omega)$. Then, the probability amplitude of $c_1(t)$ can be calculated by:

$$c_1(t) = -i\int_0^t dt' \langle\psi_1|\hat{H}_v(\omega)|\psi_0\rangle e^{i(\omega_{01}-\omega)t'}$$

$$= -i\langle\psi_1|\hat{H}_v(\omega)|\psi_0\rangle\frac{e^{i(\omega_{01}-\omega)t}-1}{i(\omega_{01}-\omega)} \quad (2.10)$$

where the $\hat{H}_v(\omega)$ is the Hamiltonian about V(ω) and ω_{01} is the transition energy between the $|0\rangle$ and $|1\rangle$ state. And then we can also get:

$$|c_1(t)|^2 = \left|\langle\psi_1|\hat{H}_v(\omega)|\psi_0\rangle\right|^2\left(\frac{sin[(\omega_{01}-\omega)t/2]}{(\omega_{01}-\omega)/2}\right)^2$$

$$\approx 2\pi\left|\langle\psi_1|\hat{H}_v(\omega)|\psi_0\rangle\right|^2 t\delta(\omega_{01}-\omega) \quad (2.11)$$

because at the ω_{01} peak, the sinc function approaches a δ function. Therefore, the overall frequency of the decoherence decay (relaxation) rate Γ can be defined as:

$$\Gamma = \frac{1}{\pi}\int_0^{\infty} d\omega 2\pi\frac{\partial|c_1(t)|^2}{\partial t}$$

$$= \frac{1}{\pi}\int_0^{\infty} d\omega 2\pi\left|\langle\psi_1|\hat{H}_v(\omega)|\psi_0\rangle\right|^2\delta(\omega_{01}-\omega)$$

$$= 2\left|\langle\psi_1|\hat{H}_v(\omega_{01})|\psi_0\rangle\right|^2$$

$$= 2\gamma^2 S_{V_{01}}(\omega_{01})\,|\langle\psi_1|\sigma_v/2|\psi_0\rangle|^2 \quad (2.12)$$

where the $S_{V_{01}}$ is the spectral density of the componets of the V(t), and the σ_v is Paouli matrix.

In this chapter, two kinds of relaxometry, T_2 coherence time and T1 relaxometry are introduced in the following, and the measurement of them is discussed in this dissertation.

2.4.1 T_2 coherence time

NV centers in diamond suffer from decay of coherence, and the decay time is called T_2 coherence time, which contributes to the sensitivities of quantum sensors [62]. In order to measure the spin coherence time of the NV center, we can apply a sequence of pulses (Fig. 2.10 (a)) to the NV spin, and this processing can be shown through the Bloch sphere (Fig. 2.10 (b)) [63].

The spin of the NV center is initialized into the $|0\rangle$ state by using a green laser. Then we apply the first $\pi/2$ pulse from the microwave to the NV spin so that the spin can lie down in the x-y plane. At this time, the spin state accumulates phase due to interactions with magnetic fields during the free evolution time. After that, a π pulse is applied to flip the spin by 180°, and the free evolution time is reversed, effectively canceling out the phase errors accumulated in the first half of the evolution time. Finally, another $\pi/2$ pulse is applied so that the spin can go back to the $|0\rangle$ state. And as a reference, a $3\pi/2$ pulse can also be applied as a final pulse [64].

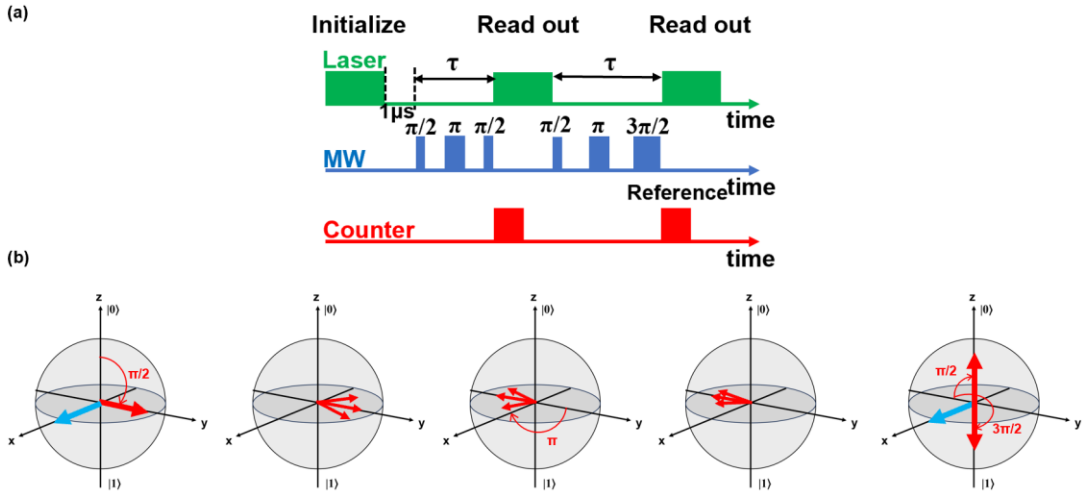

Fig. 2.10.(a) Sequence for T_2 coherence time measurement. (b) Bloch sphere of T_2 coherence time protocol.

2.4.2 T_1 relaxometry

T_1 relaxation time shows the transition rate between $|0\rangle$ state and $|1\rangle$ state [65]. The transition rate is measured by initializing the sensor at time $t' = 0$ and reading the transition probability after $t' = t$ without further manipulation of the quantum system. The transition rate can be written by [61]:

$$(T_1)^{-1} = \frac{1}{2}\gamma^2 S_V(\omega_0)$$

Where T_1 is the relaxation time.

This relaxation process is influenced by interactions with the lattice or local environment, such as temperature or spin noise [66] [67]. The T_1 time is typically much longer than T_2 and is a critical parameter for determining the NV center's sensitivity and operational stability in various applications like detecting the presence of magnetic ions, spin waves in magnetic films, and performing spectroscopy of electronic and nuclear spins [68].

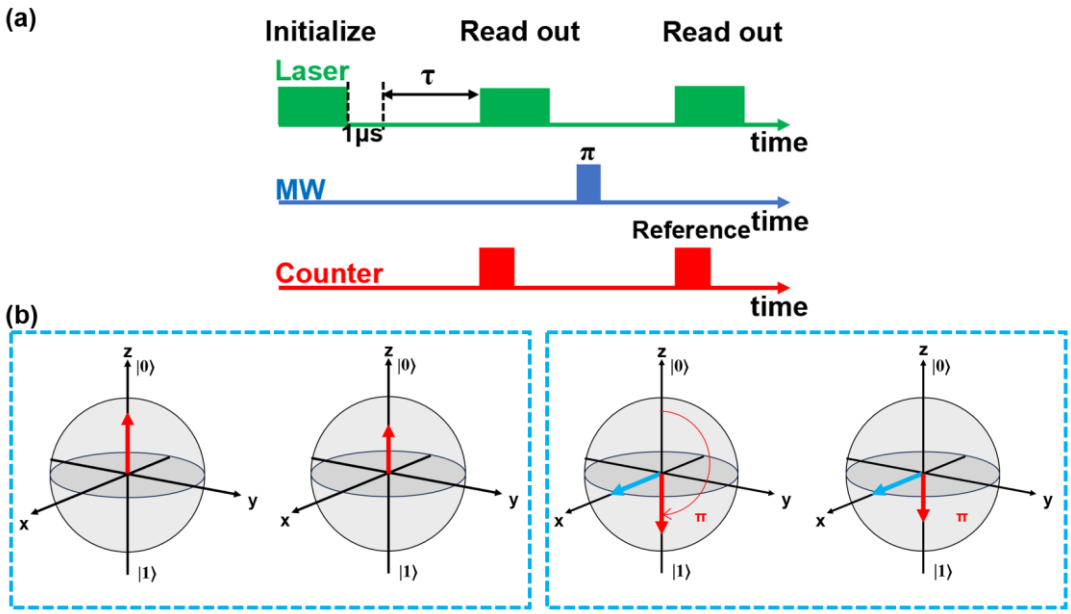

Fig. 2.11.(a) Sequence for T_1 relaxation time measurement. (b) Bloch sphere of T_1 relaxation time protocol.

Chapter 3
Fabrication of NV center probes

3.1 Diamond preparation

3.1.1 Fabrication of NV centers by N^+ ion implantation

In order to fabricate an NV center probe, an electronic grade type-IIa diamond with (100) orientation from Element Six company was bought and prepared.

The diamond (2 mm × 2 mm × 0.5 mm) was polished to around 50 μm thickness and then implanted with $^{14}N^+$ at the energy of 30 keV and dosage of 1×10^{12} ions/cm^2 by the ion implantation device (Fig. 3.1.(a)). After that, the diamond was annealed at 900 ℃ for 2 hours by the infrared ray lamp heating device (Fig. 3.1.(b)), and then NV centers were generated [69]. According to the simulation of SRIM [70], the NV center layer is formed about 40 nm beneath the diamond surface. Finally, the diamond with NV centers was cleaned by mixed acid (HNO_3 and H_2SO_4 in a ratio of 1:3) at 220 ℃ for 30 minutes and washed with pure water. These processes were shown in Fig. 3.2.

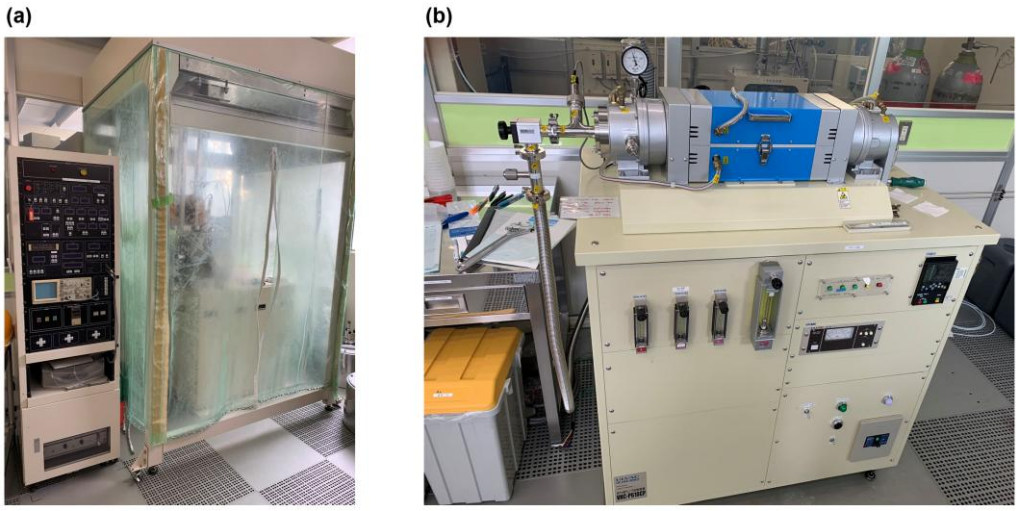

Fig. 3.1.(a) The ion implantation device in JAIST. (b) The infrared ray lamp heating device in JAIST.

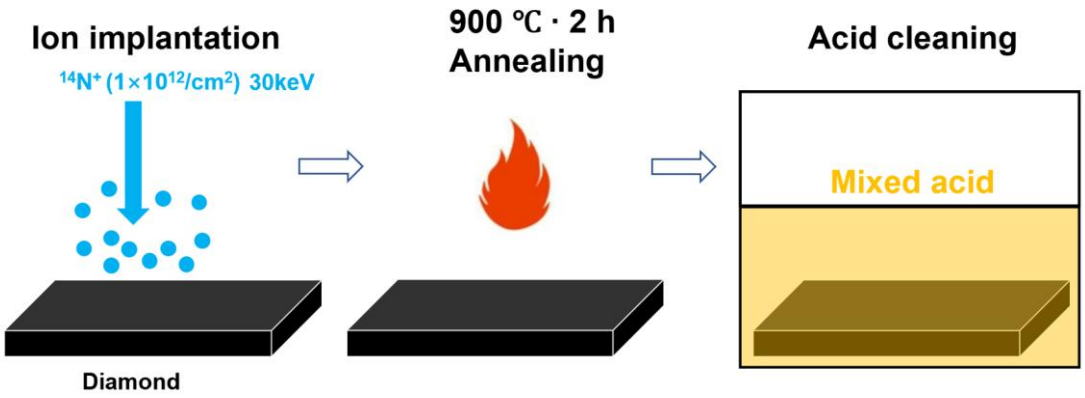

Fig. 3.2. The diagram for the process of NV centers fabrication. The processing includes nitrogen ion implantation, annealing, and mixed acid cleaning.

3.1.2 Fabrication of the triangular prism (TP) diamond

After the creation of NV centers, the diamond was fixed on a carbon substrate (Fig. 3.3.(a)) and cut into triangular shape pieces, which were named the triangular prism (TP) diamond, via laser (Fig. 3.3.(b)) by Syntek company.

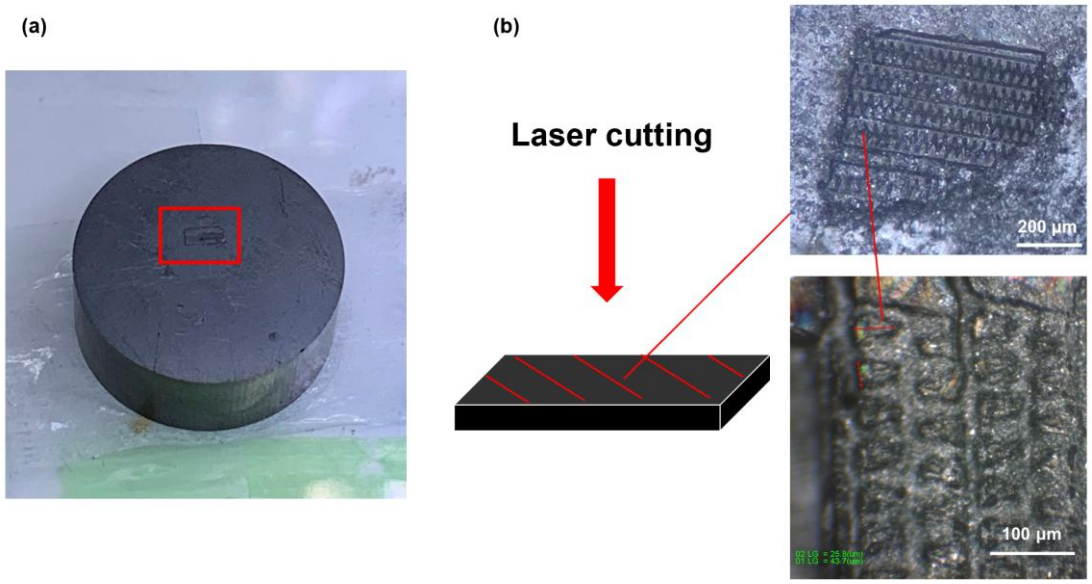

Fig. 3.3.(a) The diamond with NV centers (red rectangular part) is fixed on a carbon substrate. (b) The diamond is cut into triangular pieces by Syntek company via laser.

We used a tweezer to cut off one of the TP diamonds, picked it up by a tungsten-attached rod with a micromanipulator, and put it in a plastic gridding box. Then we add

one drop of acetone to remove the carbon covering on the TP diamond. After the cleaning, the TP diamond was picked up and placed on a glass substrate (Fig. 3.4.(a)). To avoid moving, we added a little fluoroelastomer glue around the corner of the TP diamond and heated it for 2 hours at 100 ℃ (Fig. 3.4.(b)). Finally, a quartz tube was placed close to the TP diamond and fixed with fluoroelastomer glue, as a marker, to remind us of the position of the TP diamond during the processing afterward (Fig. 3.4.(c)).

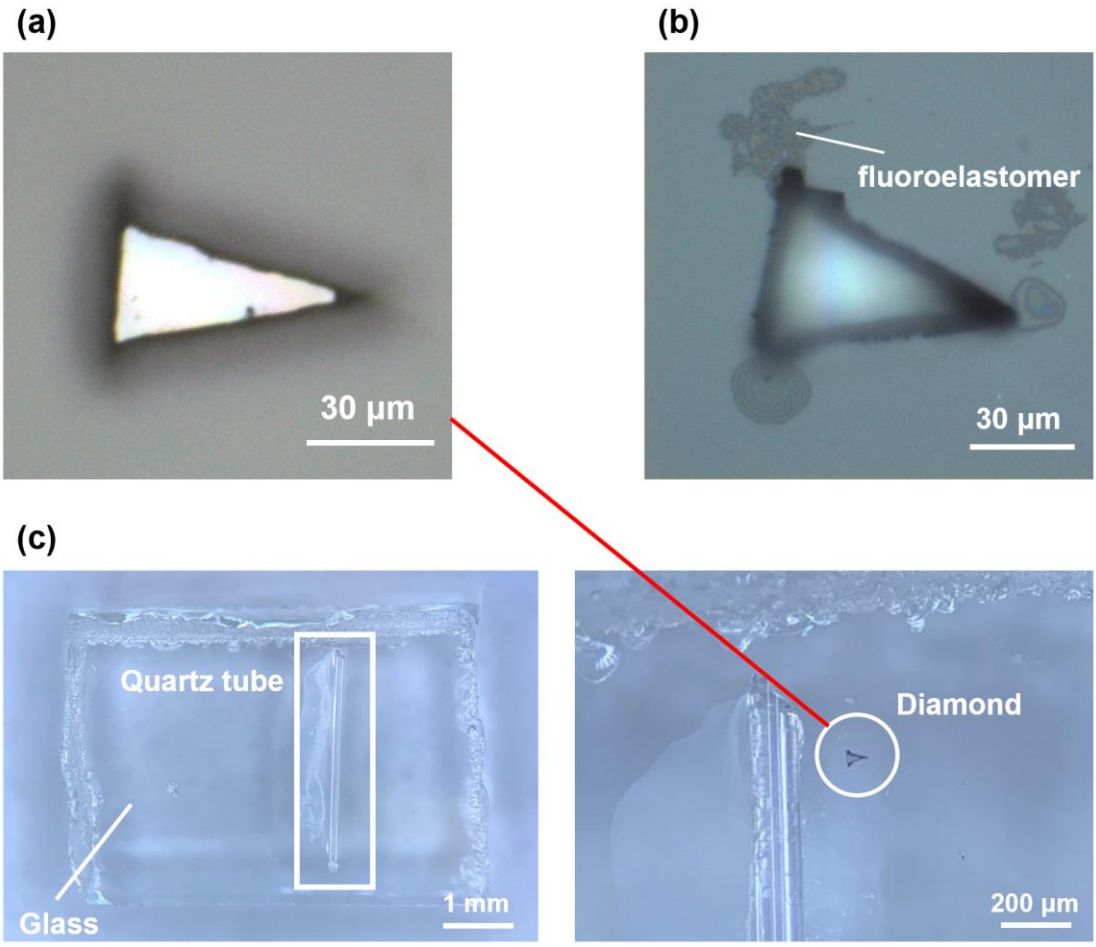

Fig. 3.4.(a) The cleaned TP diamond is placed on a glass. (b) A small amount of fluoroelastomer is put at the corner of the TP diamond to fix it. (c) A quartz tube (red rectangular part) is fixed on the glass by fluoroelastomer as a marker, and the TP diamond is placed close to the tube.

Then, we checked the photoluminescence (PL) images (Fig. 3.5.(a)) [71] and ODMR images (Fig. 3.5.(b)) of the TP diamond to confirm the existence of NV centers through a homemade microscope system.

By the way, because during the whole processing of diamond fabrication, the small size TP diamond could be lost easily, we usually prepare more than 2 pieces of TP diamond at the same time.

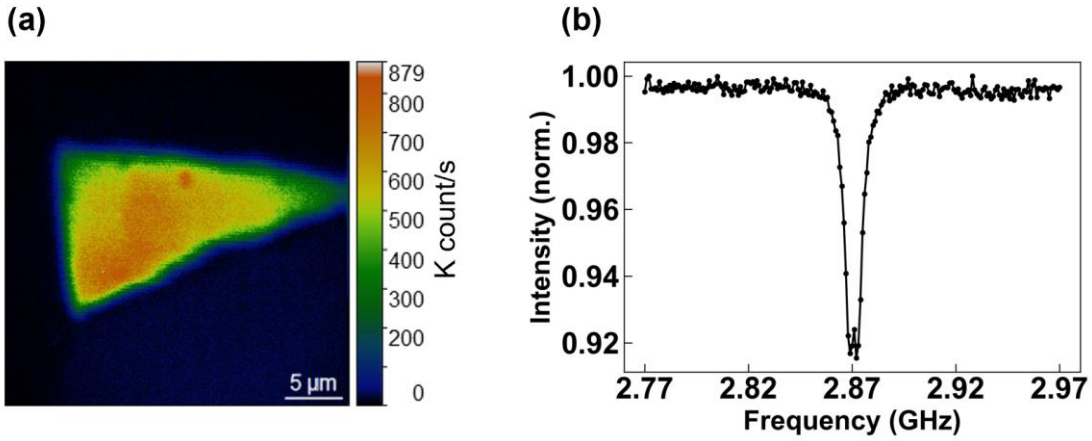

Fig. 3.5.(a) The PL image of the TP diamond. (b) The ODMR spectrum of the TP diamond

3.2 Process of probes' fabrication

3.2.1 Pt-Pd coating on the TP diamond

In order to protect the NV centers from the damage of ions during the milling process [72], it is necessary to cover a protective film on the TP diamond. Therefore, we first dropped a droplet of polyvinyl alcohol (PVA) (Fig. 3.6.(a)) on the diamond, so that after drying, a layer of PVA film remained on the diamond surface. Then, the TP diamond was placed on a sputtering device E-1030 (Fig. 3.6.(b)) and a 160 nm thickness Platinum-Palladium (Pt-Pd) coating was deposited on the surface of the TP diamond. The side view of the PVA and Pt-Pd coating on the TP diamond is shown in Fig. 3.6.(c).

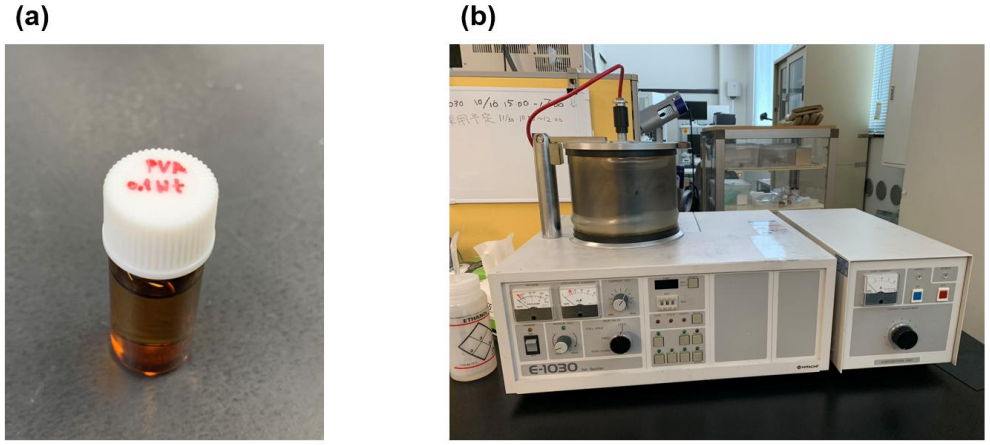

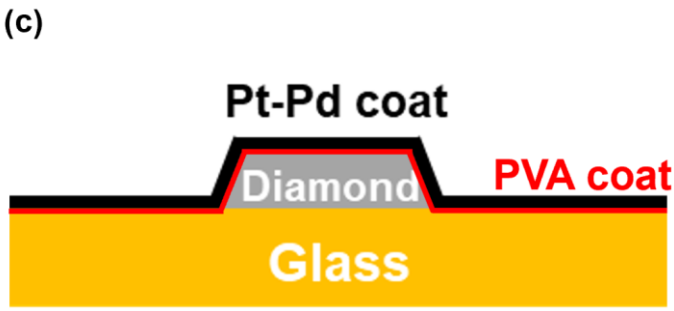

Fig. 3.6.(a) The 0.1wt% PVA. (b) The sputtering device E-1030 in JAIST. (c) The side view of the coating on the TP diamond that is fixed on a piece of glass.

3.2.2 Fabrication of pillars by focused ion beam (FIB)

With the protection of PVA and Pt-Pd layers, the diamond was able to be milled into a probe with a pillar shape by focused ion beam (FIB) process via FIB device SMI-3050 (Fig. 3.7.(a)).

FIB is a technique that uses a highly focused beam of Gallium (Ga^+) ions to mill materials with extremely high precision. When Ga^+ ions from the high energy beam (30 keV) hit the diamond, the carbon atoms from the surface of the diamond will be removed with a sputtering process (Fig. 3.7.(b)) [73] [74].

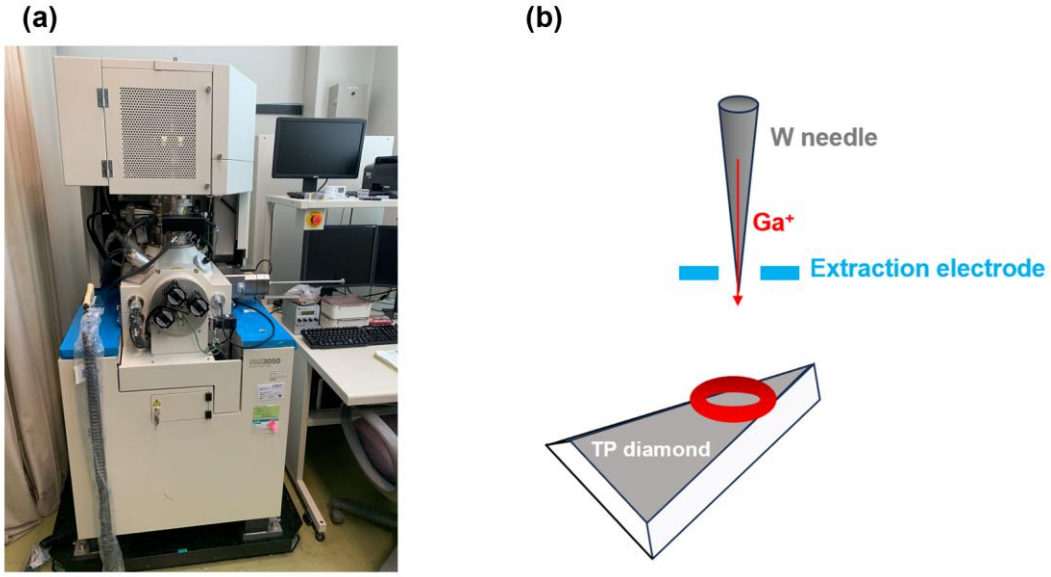

Fig. 3.7.(a) The FIB device SMI-3050 from Hitachi company. (b) The principle of the FIB process.

3.8.(a)) to mill the most parts of the TP diamond surface with around 15 μA current so that only one cuboid pillar (around 4 μm × 4 μm × 5 μm) remained on the surface of TP

diamond. Then, we milled the remaining pillar using a donut-shaped pattern (inner diameter is 1 μm) (Fig. 3.8.(b)) with around 800 pA current so that a cylinder-shaped pillar with 1 μm diameter and 1.6 μm height was fabricated (Fig. 3.8.(c)) [75]. We can combine FIB and scanning ion microscopy (SIM) to image the diamond after the milling process (Fig. 3.8.(d)) [76].

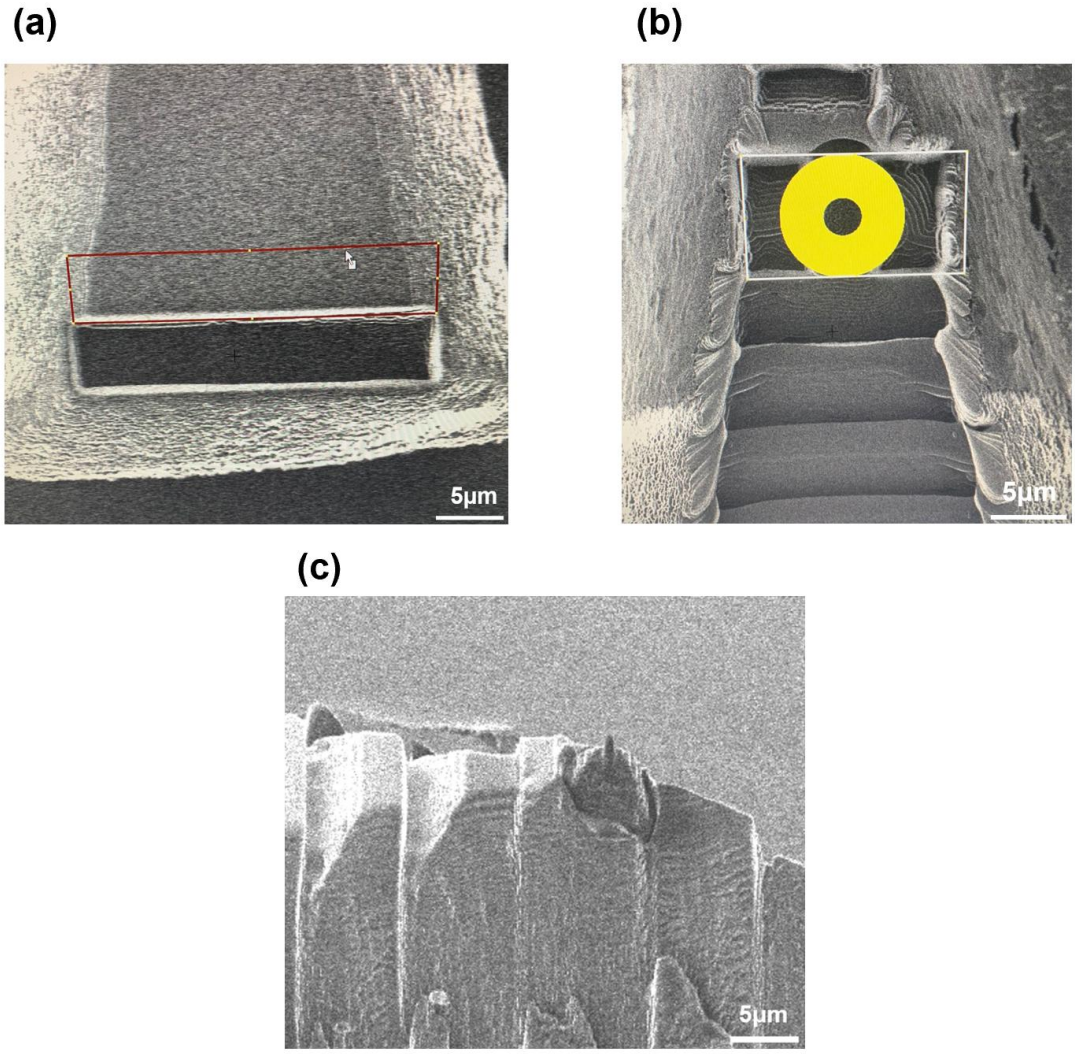

Fig. 3.8.(a) The rectangular pattern cut on the TP diamond. (b) The donut-shaped pattern cut on the TP diamond. (c) The side view after finishing the FIB process.

However, during the FIB milling process, Ga^{+} ions can leave residual damage and surface defects in the form of amorphous carbon, which can affect the diamond's properties. Therefore, the real diameter of the pillar is less than 1 μm (around 800 nm), and we need to find some ways to recover the properties of the probe [77] [78].

3.2.3 Removal of Pt-Pd coated layer by aqua regia acid

After the FIB process, the glass substrate with a TP diamond was placed inside a small culture dish. We prepared the aqua regia acid with the mixture of HNO_3 and HCl in a ratio of 1:3 and dropped the aqua regia acid into the small culture dish with a pipette until the TP glass substrate was totally submerged. Then we heated the culture dish at 60 ℃ for about 15 minutes so that the Pt-Pd coating was totally removed (Fig. 3.9.(b)) [79]. Finally, we removed the aqua regia acid by pipette, took out the glass substrate, and put it into another small culture dish with pure water inside. After around 5 minutes of standing time, we took out the glass substrate, and the removal of Pt-Pd coating was finished (Fig. 3.9.(a)).

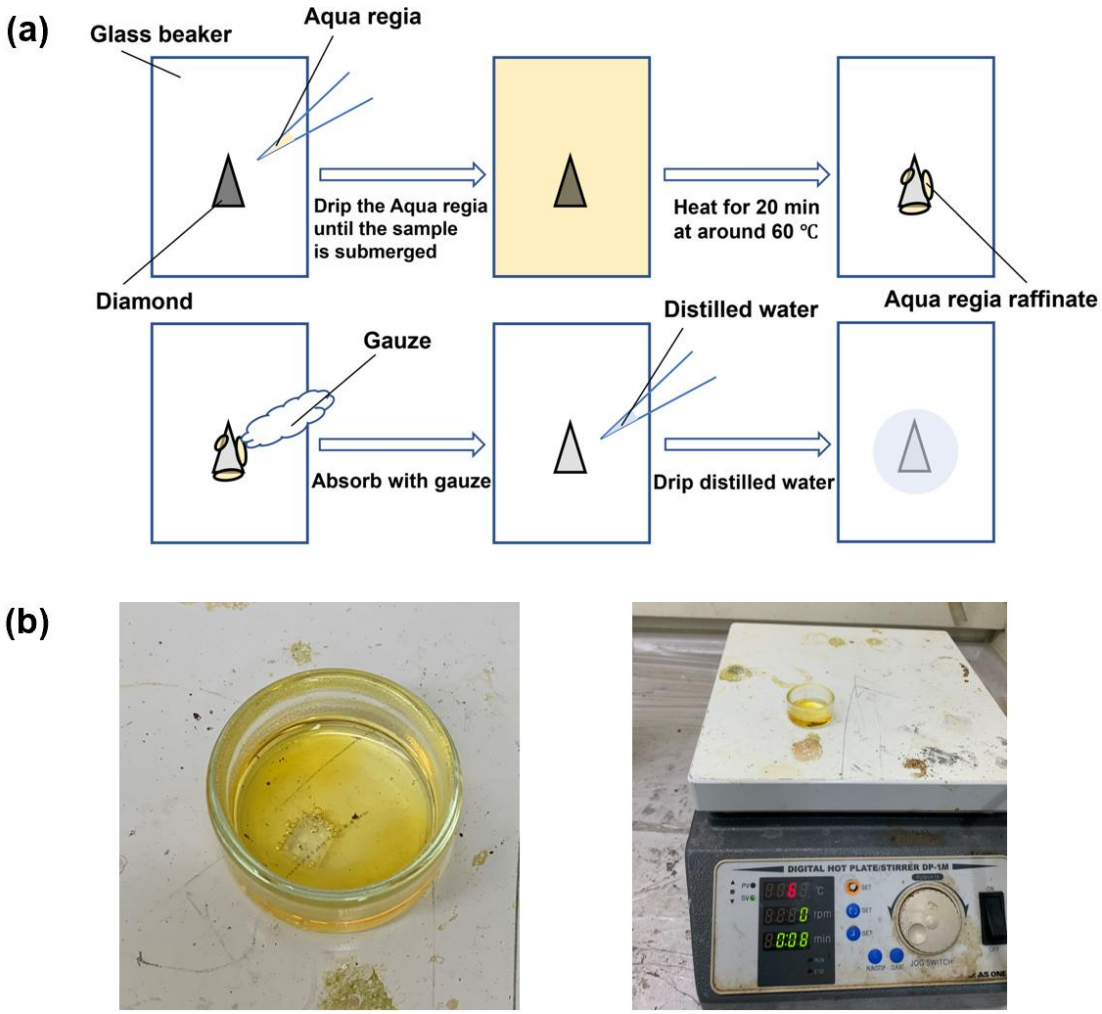

Fig. 3.9.(a) The acid cleaning process. (b) The fabricated diamond is put into the aqua regia and heated under 60 ℃.

3.3 Inductively coupled plasma (ICP) etching on TP diamond

As mentioned in Chapter 3.2, after the FIB process, some residual damages that affected the properties of NV centers were left on the milled pillar. Therefore, we tried to find a way to recover the properties of NV centers after the FIB process, and eventually, we decided to do inductively coupled plasma (ICP) etching on the pillar for a few nanometers.

To confirm the effect of the ICP etching process, firstly the ODMR, Rabi oscillation, spin echo, and T_1 relaxation of the pillar were measured before the ICP etching process. Then we applied ICP etching on the pillar and did the same measurements again under the same conditions. The results before and after ICP etching are discussed below.

3.3.1 The principle of ICP etching on TP diamond

ICP etching is a high-density plasma etching technique with a high etching rate, high precision, and selectivity to achieve efficient, anisotropic etching. It is widely used in nanofabrication, especially for materials that are chemically inert and difficult to etch, such as diamonds. Diamonds are chemically inert and highly resistant to etching. However, ICP etching can achieve effective diamond etching with the help of gases like oxygen and designed plasma parameters. During the ICP etching process, a plasma is generated by inductive coupling. Radiofrequency (RF) power is applied to an inductive coil, which ionizes a gas like oxygen to create a dense plasma. A separate RF bias is applied to the sample stage vertically, which attracts the ions toward the sample surface.

It is known that the repeated formation of mesa structures degrades the electronic properties of devices so that the ICP etching may damage the surfaces of diamonds. To develop a fabrication method for diamond devices that maintains diamond's unique electrical properties, it is essential to estimate the extent of this damage and optimize the processing parameters accordingly. Therefore, soft ICP etching is expected to etch the diamond for researchers [80] [81].

Soft ICP etching is a technique used to achieve gentle, low-damage etching with minimal impact on the underlying material properties, while standard ICP etching uses high-power plasma to maximize the etch rates. Therefore, soft ICP etching operates with carefully reduced power and conditions to control the etching process more delicately [82].

In this research, soft ICP etching was used to etch the diamond pillars. The diamond was placed on the sample holder inside the ICP chamber, and the low RF power (around 300 W) was applied to ignite the injected mixture of O_2 and CF_4 gas so that the plasma

was generated to be used for etching. The power of RF bias was reduced (even down to 0 W) to minimize the ion acceleration toward the diamond. Then, due to the reaction between plasma and the carbon atoms on the diamond surface, the diamond started to be etched (Fig. 3.10) [83].

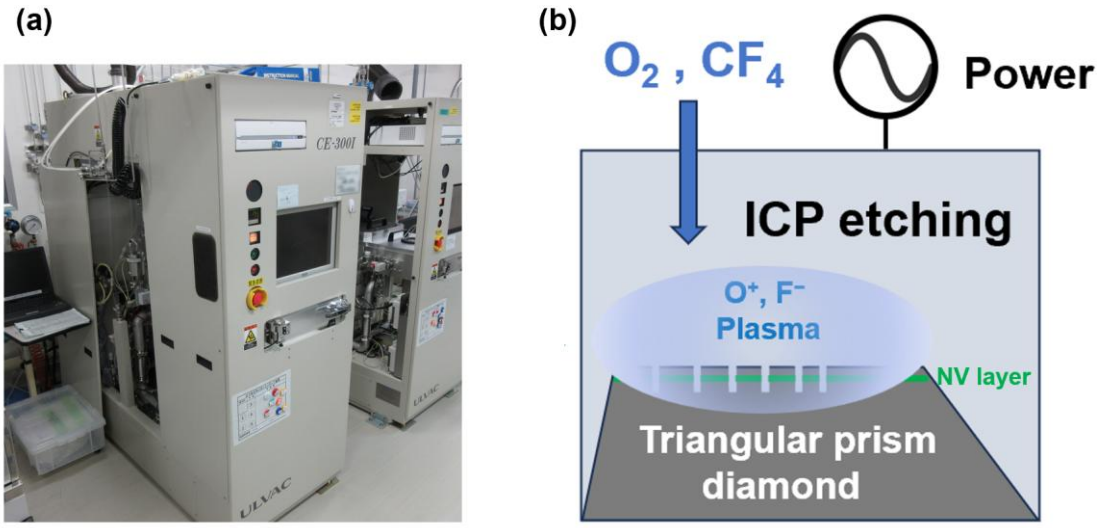

Fig. 3.10.(a) The ICP etching device CE-300I from Ulvac company (https://unit.aist.go.jp/g-quat/Qufab/Qufab_en/devices3.html). (b) The ICP etching process.

3.3.2 The preparations for measurements

Two TP diamonds, TP1 (Fig. 3.11.(a)) and TP2 (Fig. 3.11.(b)), were prepared following Chapters 3.1 and 3.2 for this measurement. The difference point is that we milled 6 pillars with different diameters on the TP1 diamond. According to the pattern, the diameters of the 6 pillars should be 4.8 μm, 2.9 μm, 1.9 μm, 1 μm, 0.75 μm, and 0.57 μm, while the virtual diameters were smaller because of the FIB residual damages. These pillars were measured and then etched 15 nm by ICP etching so that the diameters of the pillars were even smaller and the NV centers were closer to the diamond surface. After the measurement, we etched them with another 15 nm and did the measurement again.

For TP2 diamond, we just milled one 0.9 μm pillar on the diamond and did 25 nm ICP etching on it only once. We still did the same measurement as TP1 diamond before and after the ICP etching process.

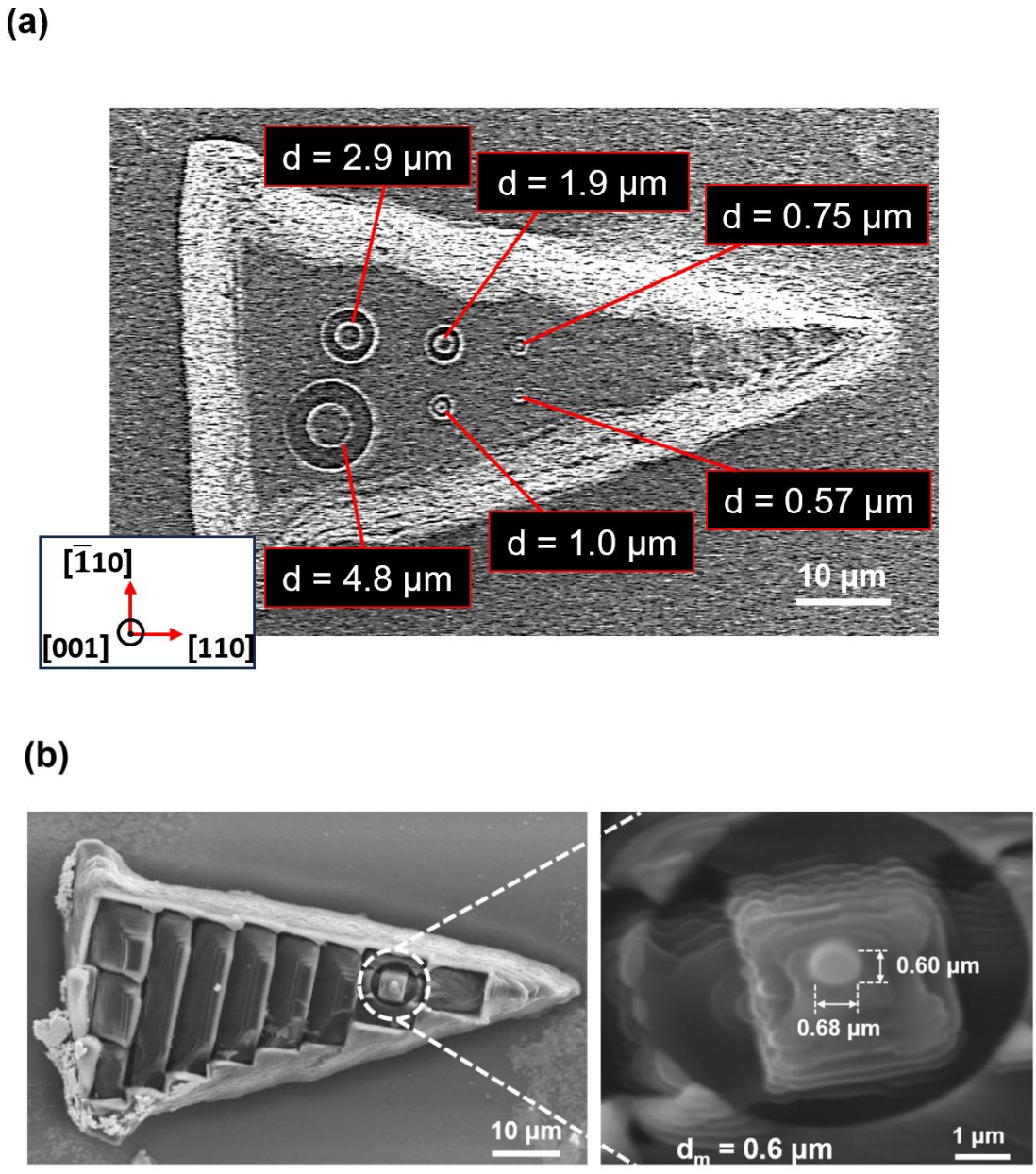

Fig. 3.11.(a) SIM image of TP1 diamond with 6 pillars. (b) SEM image of TP2 diamond with one pillar.

3.3.3 The measurements before and after ICP etching

Before the ICP etching, we put the diamond on a sample holder that connected with microwave (Fig. 3.12.(a)) and took the PL images and did measurements of ODMR, Rabi oscillation, spin echo, and T_1 relaxation for each pillar via pulse measurement device (Fig. 3.12.(b)).

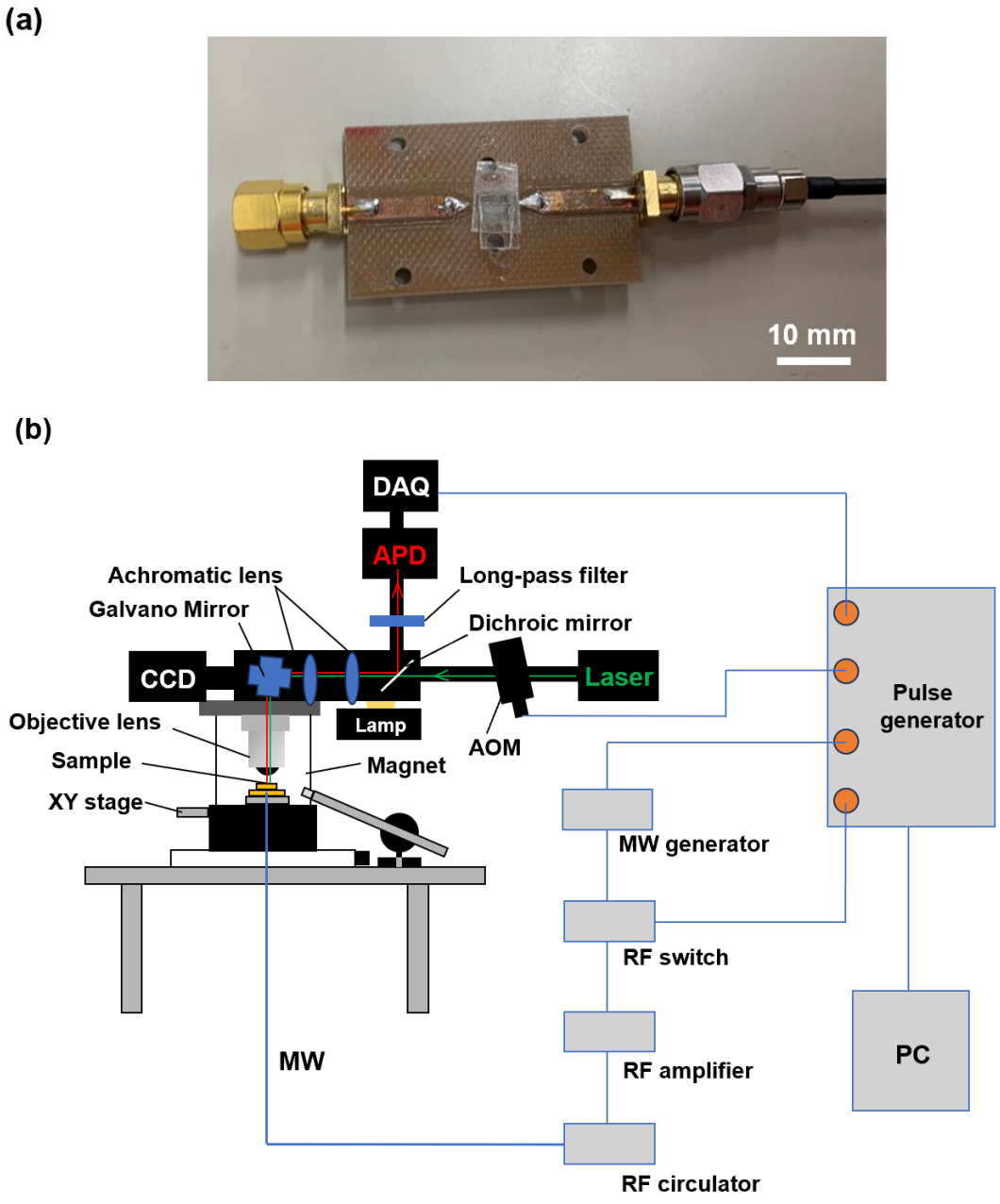

Fig. 3.12. (a) The sample holder that is connected with MW. (b) The pulse measurement device from An's Lab.

To achieve the measurement, we set up a magnet (Fig. 3.13) around the sample to apply a magnetic field. We can adjust the direction of the magnet so that the direction of the magnetic field can be parallel to the NV axis [84] [85].

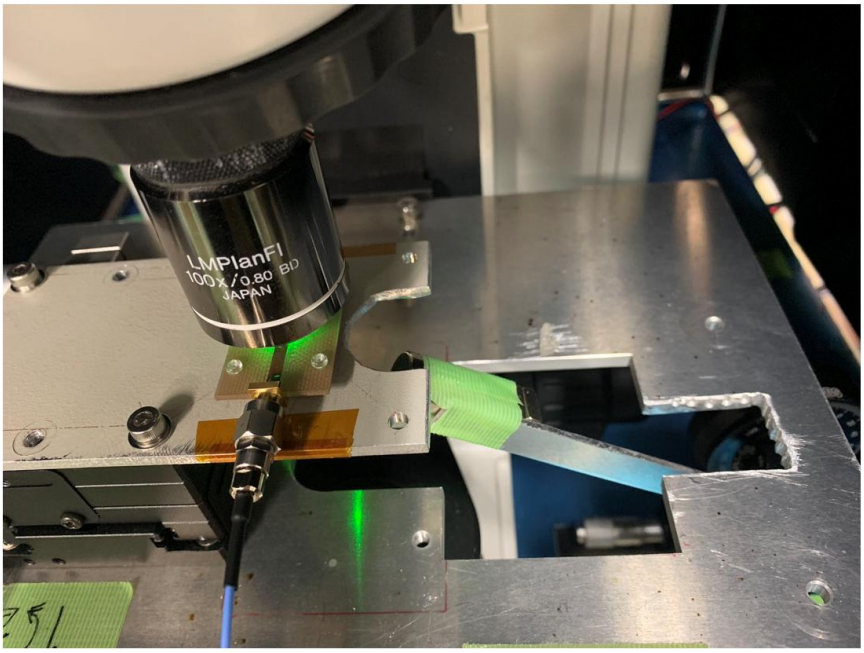

Fig. 3.13 The magnet is adjusted and close to the sample.

Then we did ICP etching on TP1 diamond with 15 nm and TP2 diamond with 25 nm. After the ICP etching process, the same measurements were done under the same conditions. Moreover, we did the 2nd ICP etching on TP1 diamond with 15nm and did the measurement again so that the total ICP etching depth for TP1 diamond is 30 nm.

3.3.4 Results and discussion

To compare the results before and after the 1st ICP etching process with 15 nm, we can find that the PL counts are higher, the ODMR is more clearly split into 4 dips, the Rabi oscillation contrast is higher, and the T_1 relaxation is longer. As for the 1 μm pillar, we could do the fitting of the T_1 relaxation time. For the 0.75 μm pillar, it became measurable. And for the 0.57 μm pillar, we started to get the PL image. As mentioned in Chapter 3.1, the depth of the NV centers was 40 μm, while after the 15 nm ICP etching process, the depth became 25 μm so that the NV centers were close to the diamond surface

However, after the 2nd ICP etching process, the conditions became worse. Therefore, it's possible to make a conclusion that the ICP etching process with 20-25 nm should be

optimized for Rabi contrast, T_2 coherence time, and T_1 relaxation time of the NV centers in TP diamond. The results of measurements of 4.8 μm, 2.9 μm, 1.9 μm, 1 μm, 0.75 μm, and 0.57 μm pillars are shown in Fig. 3.14 ~ Fig. 3.25.

.

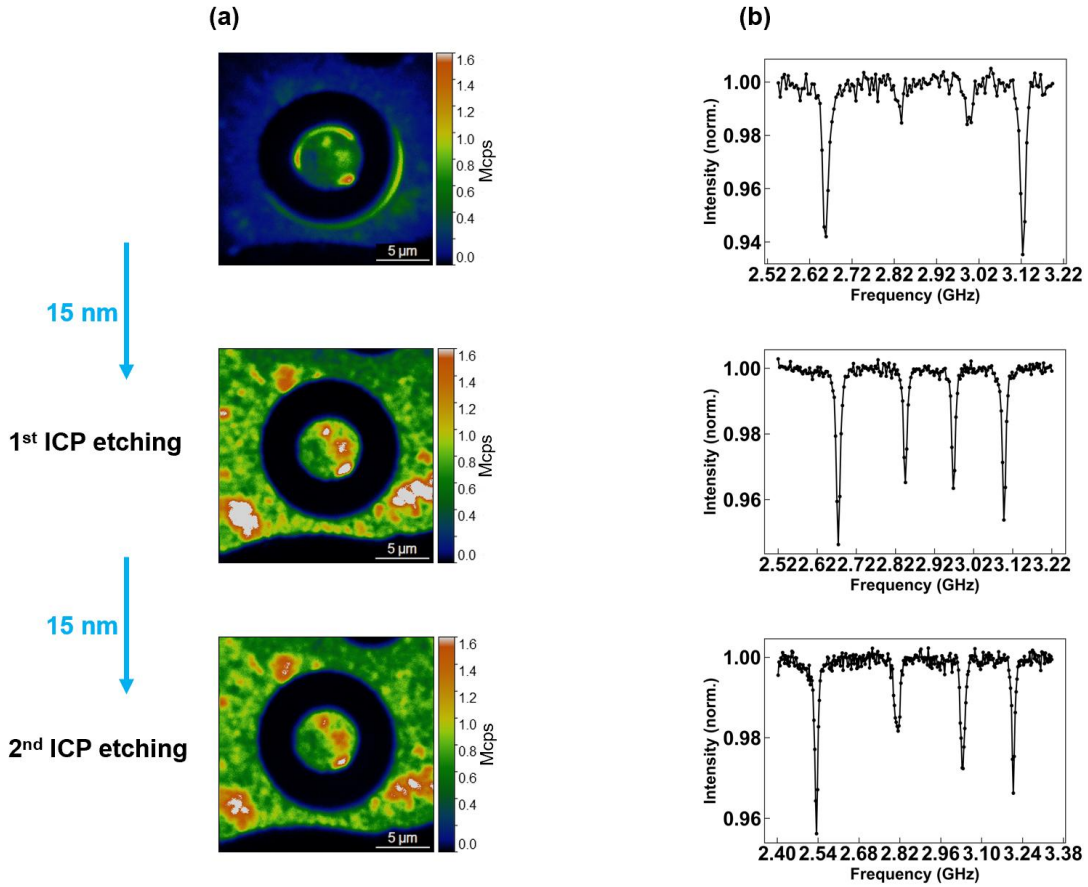

Fig. 3.14.(a) The PL images of 4.8 μm pillar before, after ICP etching with 15 nm, and after ICP etching with 30 nm. (b) The ODMR spectra of 4.8 μm pillar before, after ICP etching with 15 nm, and after ICP etching with 30 nm.

From the PL images of the 4.8 μm pillar, we can find that after the ICP etching process with 15 nm, the PL counts become larger from 1.6 M counts/s to 2.4 M counts/s, and the bright rim feature at the edge of the pillar disappears. However, after the ICP etching process with 30 nm, the counts drop a little. From the PL image before the ICP etching process, we could find that the intensity of the area without FIB is much lower than the pillar, which is because we used a different Galvano mirror at the beginning of the experiment so that the scan region is smaller. When we changed to another mirror, the intensity of the pillar and outer part became similar.

The ODMR spectra contrast didn't change so much, which is because other PL sources besides NV^-, probably NV^0, have also slightly increased due to the ICP etching, which influenced the ODMR dip contrast as the background noise.

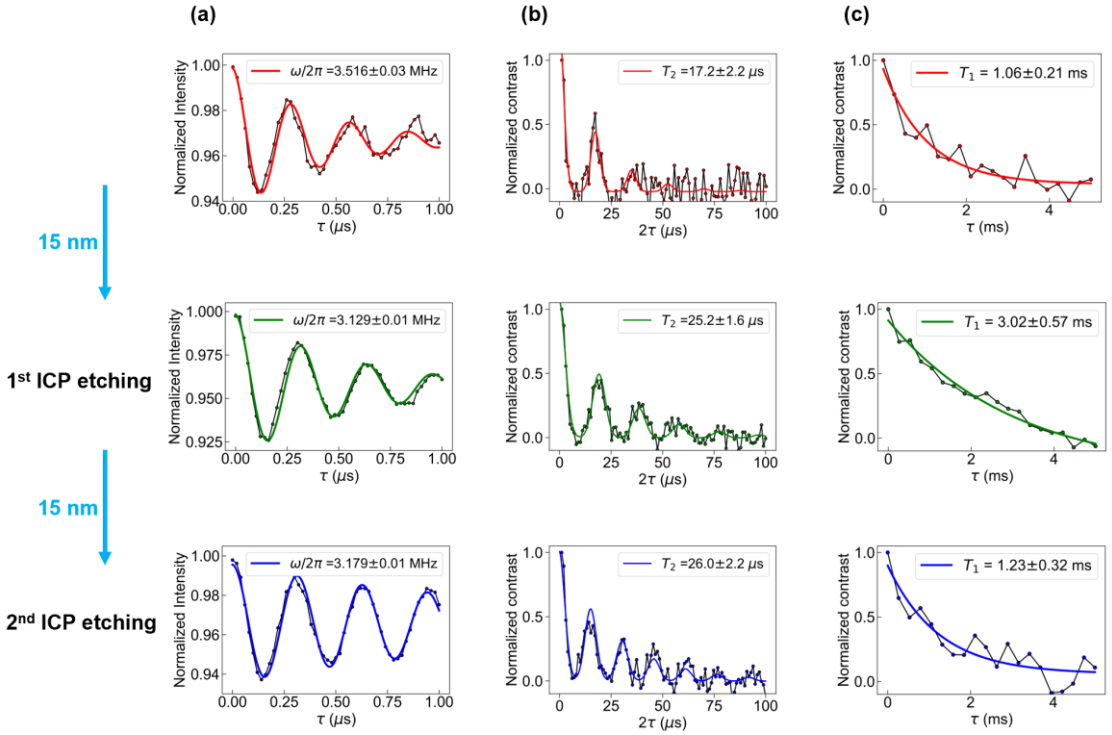

Fig. 3.15.(a) The Rabi oscillation spectra of 4.8 μm pillar before, after ICP etching with 15 nm, and after ICP etching with 30 nm. (b) The T_2 coherence time spectra of 4.8 μm pillar before, after ICP etching with 15 nm, and after ICP etching with 30 nm. (c) The T_1 relaxation spectra of 4.8 μm pillar before, after ICP etching with 15 nm, and after ICP etching with 30 nm.

From the spectra obtained after the measurements of the 4.8 μm pillar, we can know that the Rabi oscillation contrast becomes higher, and the T_2 coherence time, T_1 relaxation time become longer after the ICP etching process with 15 nm. However, after the 2nd ICP etching process, they become worse. Especially, the T_1 relaxation time becomes very short compared with the result of the 1st ICP etching process, from 3.02 ms to 1.23 ms.

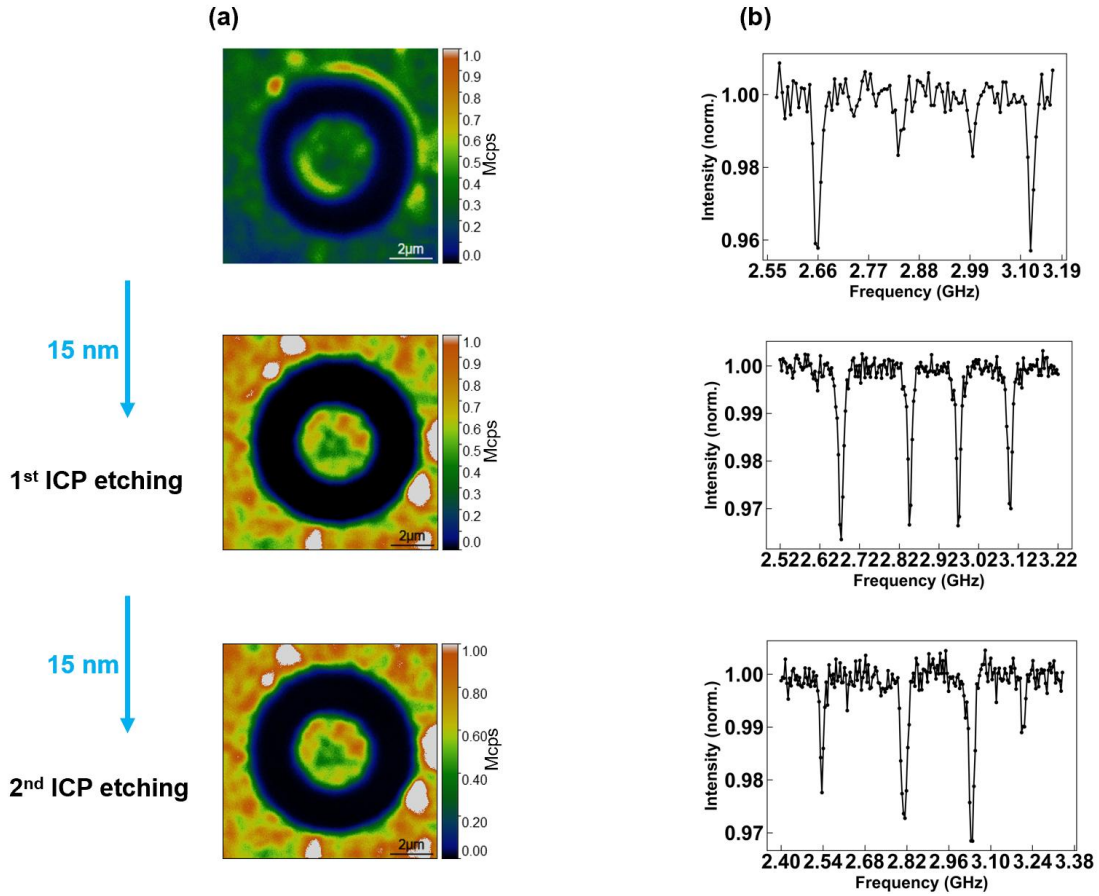

Fig. 3.16.(a) The PL images of 2.9 μm pillar before, after ICP etching with 15 nm, and after ICP etching with 30 nm. (b) The ODMR spectra of 2.9 μm pillar before, after ICP etching with 15 nm, and after ICP etching with 30 nm.

The same as 4.8 μm pillar, we can find that for the 2.9 μm pillar, after the ICP etching process with 15 nm, the PL counts become larger from 500 k counts/s to 1.1 M counts/s, and the bright rim feature at the edge of the pillar disappears.

The ODMR spectra condition is also the same as the 4.8 pillar.

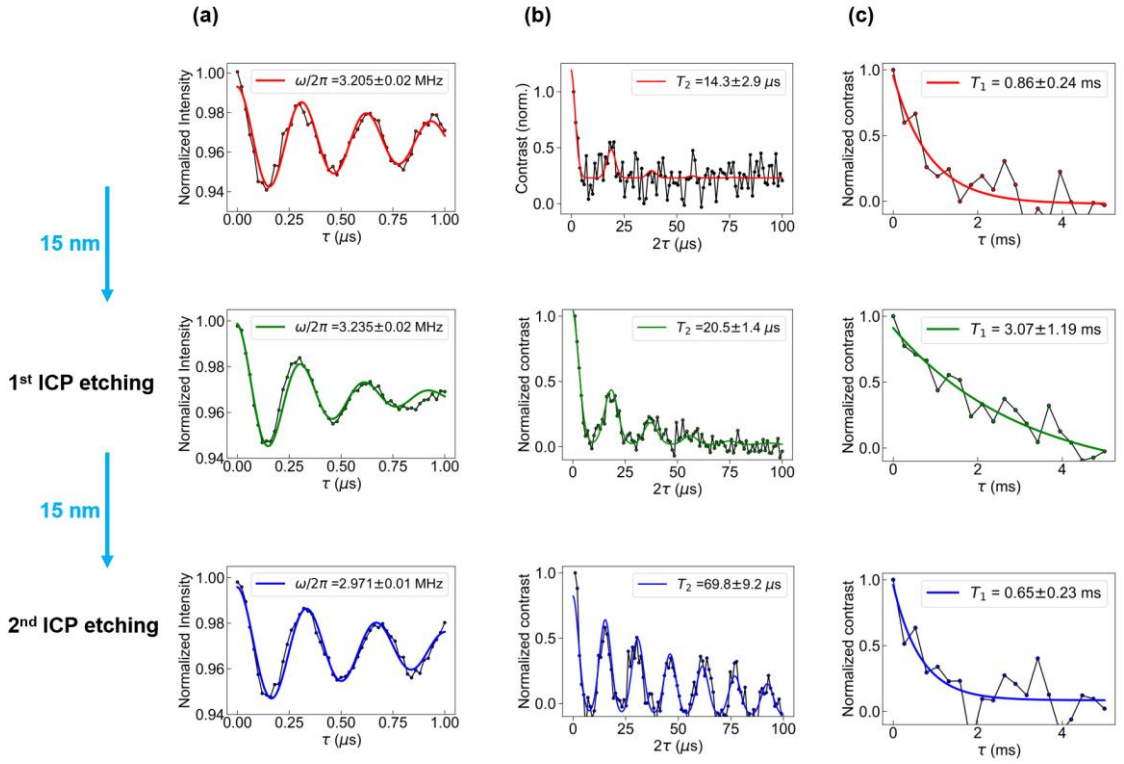

Fig. 3.17.(a) The Rabi oscillation spectra of 2.9 μm pillar before, after ICP etching with 15 nm, and after ICP etching with 30 nm. (b) The T_2 coherence time spectra of 2.9 μm pillar before, after ICP etching with 15 nm, and after ICP etching with 30 nm. (c) The T_1 relaxation spectra of 2.9 μm pillar before, after ICP etching with 15 nm, and after ICP etching with 30 nm.

From the spectra obtained after the measurements of the 2.9 μm pillar, we got the same results as the 4.8 μm pillar. The T_1 relaxation time becomes very long after the 1st ICP etching process.

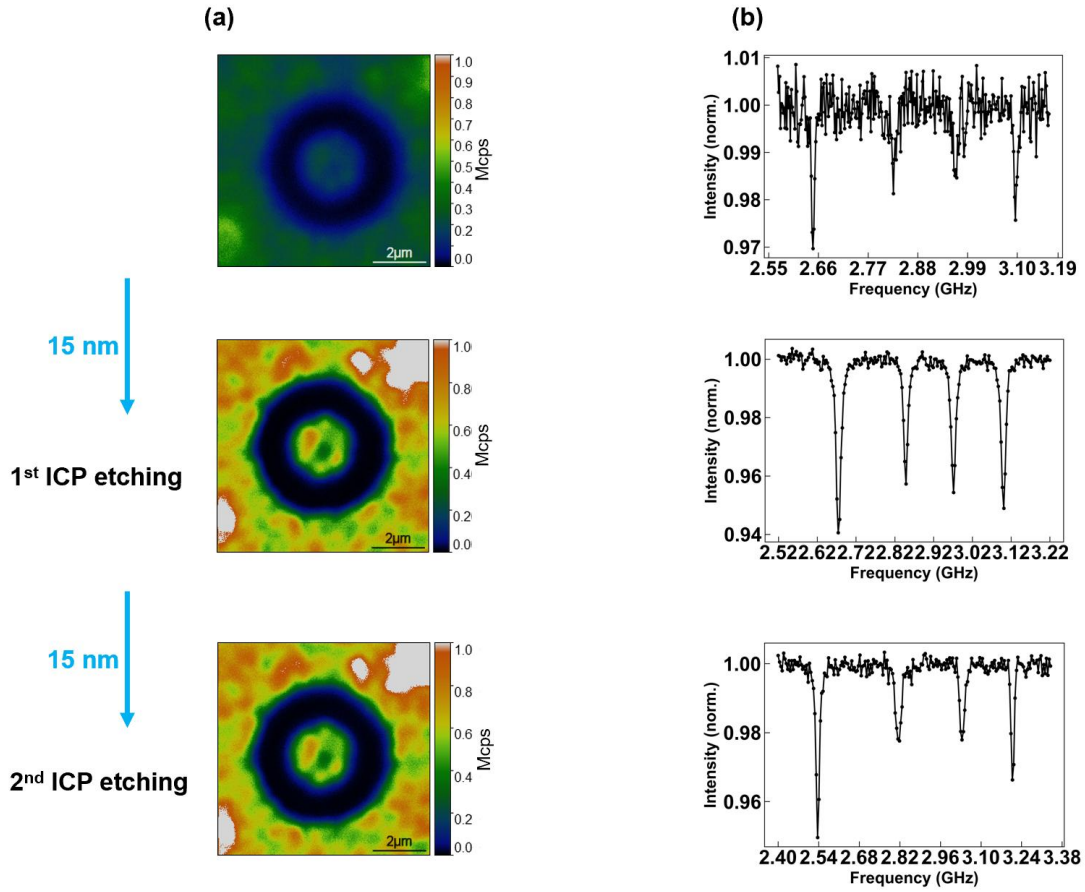

Fig. 3.18.(a) The PL images of 1.9 μm pillar before, after ICP etching with 15 nm, and after ICP etching with 30 nm. (b) The ODMR spectra of 1.9 μm pillar before, after ICP etching with 15 nm, and after ICP etching with 30 nm.

Although there is no bright rim feature on the 1.9 μm pillar, we can also get a count increase, similar to the 4.8 and 2.9 μm pillars.

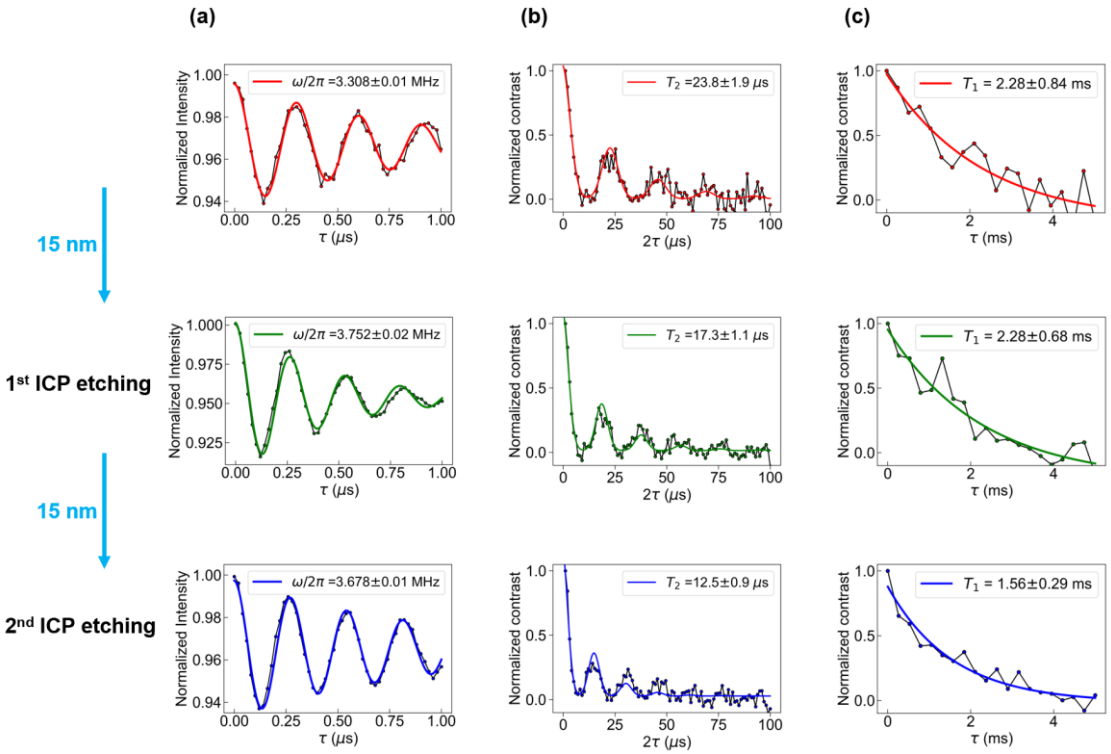

Fig. 3.19.(a) The Rabi oscillation spectra of 1.9 μm pillar before, after ICP etching with 15 nm, and after ICP etching with 30 nm. (b) The T_2 coherence time spectra of 1.9 μm pillar before, after ICP etching with 15 nm, and after ICP etching with 30 nm. (c) The T_1 relaxation spectra of 1.9 μm pillar before, after ICP etching with 15 nm, and after ICP etching with 30 nm.

For the 1.9 μm pillar, the change is not obvious after the 1st ICP etching process. However, after the 2nd ICP etching process, the T_1 relaxation time becomes shorter obviously.

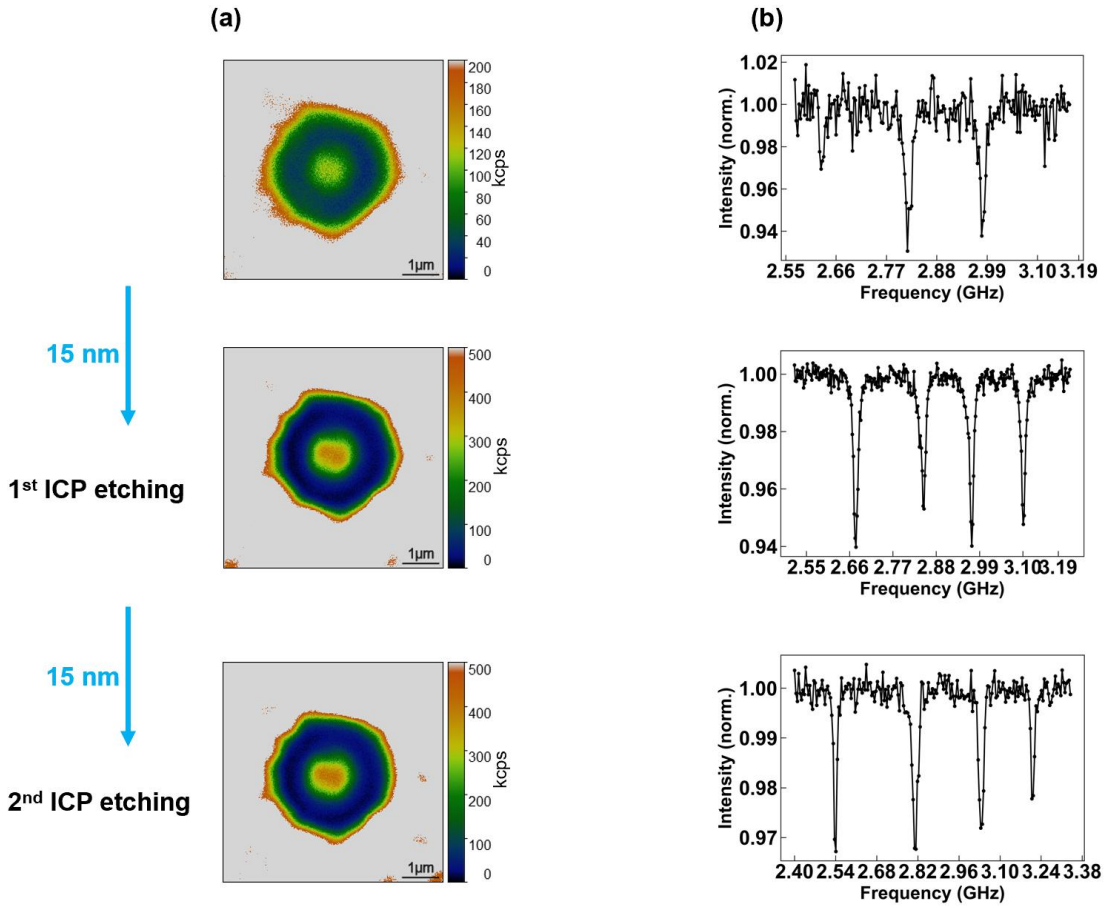

Fig. 3.20.(a) The PL images of 1 μm pillar before, after ICP etching with 15 nm, and after ICP etching with 30 nm. (b) The ODMR spectra of 1 μm pillar before, after ICP etching with 15 nm, and after ICP etching with 30 nm.

The PL and ODMR conditions of the 1 μm pillar are the same as 4.8, 2.9, and 1.9 μm pillars.

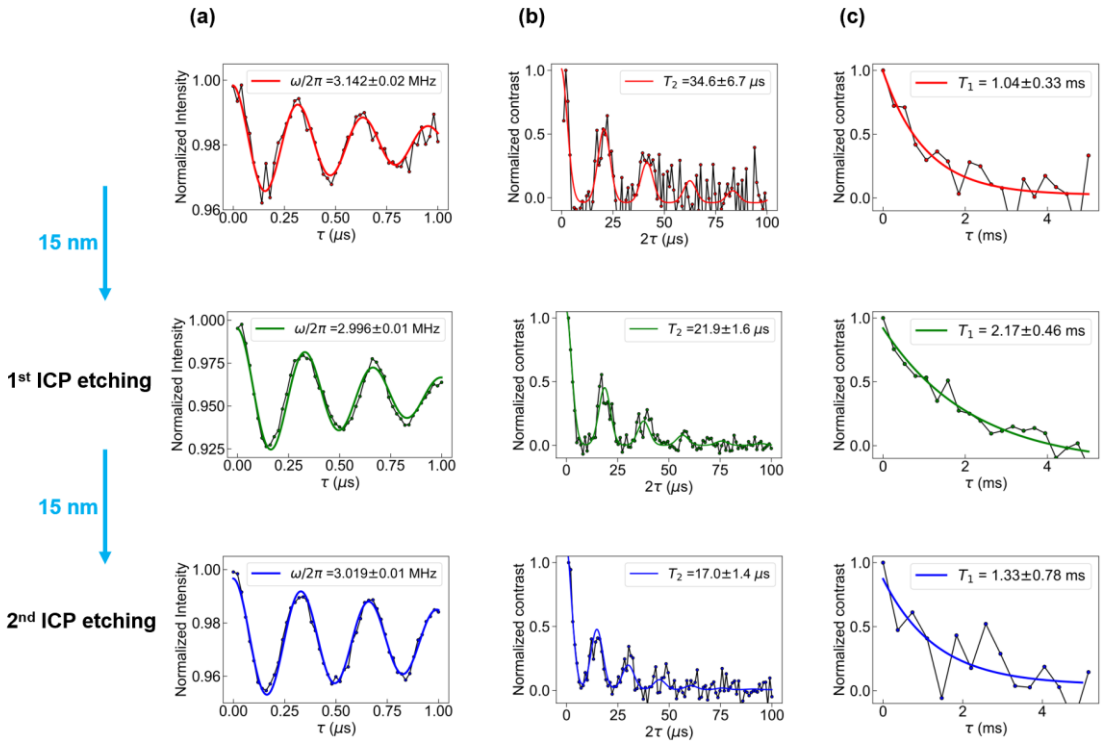

Fig. 3.21.(a) The Rabi oscillation spectra of 1 μm pillar before, after ICP etching with 15 nm, and after ICP etching with 30 nm. (b) The T_2 coherence time spectra of 1 μm pillar before, after ICP etching with 15 nm, and after ICP etching with 30 nm. (c) The T_1 relaxation spectra of 1 μm pillar before, after ICP etching with 15 nm, and after ICP etching with 30 nm.

For the 1.0 μm pillar, the T_2 time decreases after ICP etching, which is similar to the 1.9 μm pillar. The T_1 relaxation time becomes longer after the 1st ICP etching process, while shorter after 2nd ICP etching process.

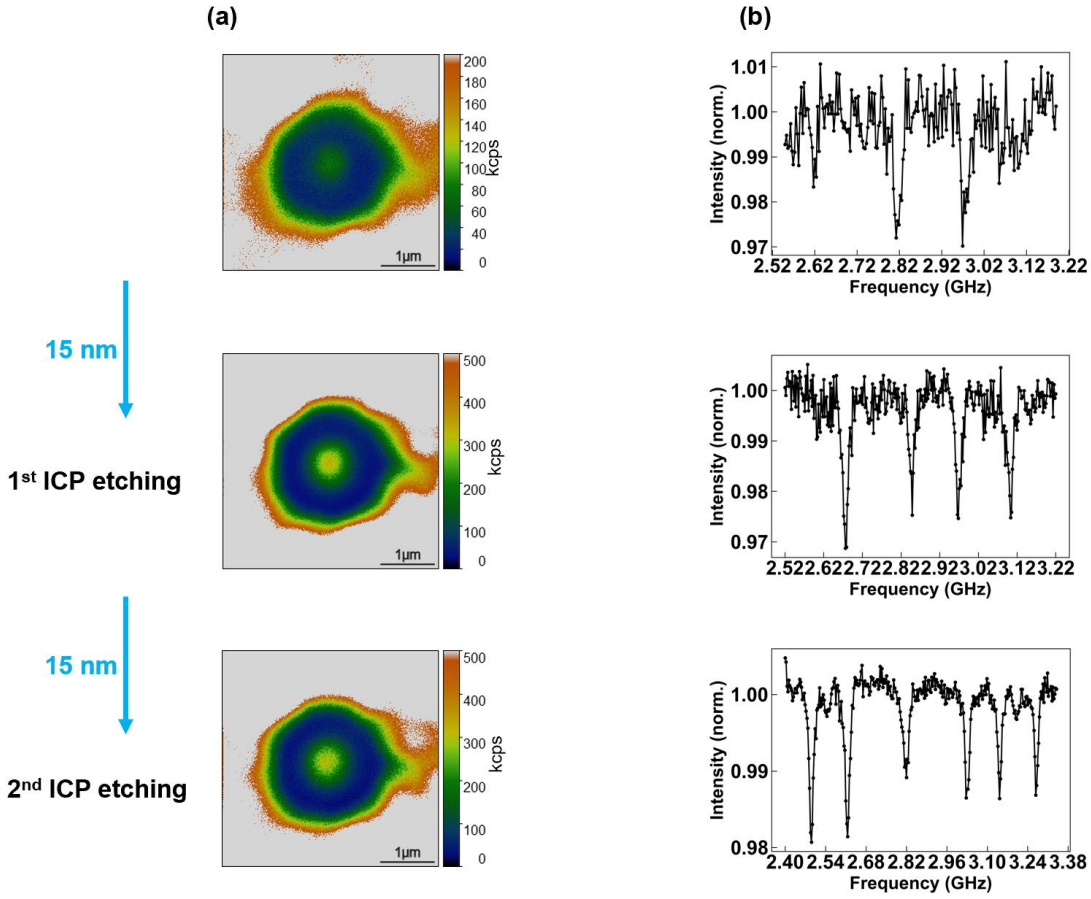

Fig. 3.22.(a) The PL images of 0.75 μm pillar before, after ICP etching with 15 nm, and after ICP etching with 30 nm. (b) The ODMR spectra of 0.75 μm pillar before, after ICP etching with 15 nm, and after ICP etching with 30 nm.

After the 1st ICP etching process, the results of the 0.75 μm pillar are the same as other pillars. However, after the 2nd ICP etching process, we find that there are more dips in the ODMR spectrum, which will influence the measurements of this pillar.

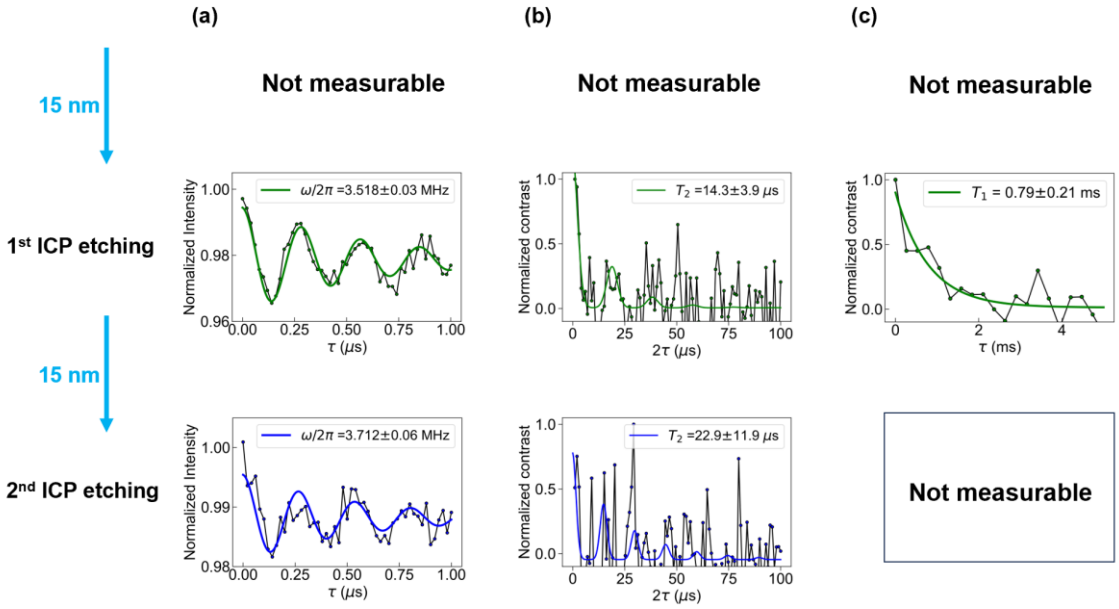

Fig. 3.23.(a) The Rabi oscillation spectra of 0.75 μm pillar before, after ICP etching with 15 nm, and after ICP etching with 30 nm. (b) The T_2 coherence time spectra of 0.75 μm pillar before, after ICP etching with 15 nm, and after ICP etching with 30 nm. (c) The T_1 relaxation spectra of 0.75 μm pillar before, after ICP etching with 15 nm, and after ICP etching with 30 nm.

Before the ICP etching process, the data of 0.75 μm pillar is too noisy to do the measurements, therefore we can't get the results. Fortunately, after the 1st ICP etching process, it's possible to do the measurement.

However, the results show that the T_1 relaxation time is not long enough as the other pillars with only 0.79 ms. And after the 2nd ICP etching process, the data of T_2 coherence time becomes noisy and we can't even get the result of T_1 relaxation time.

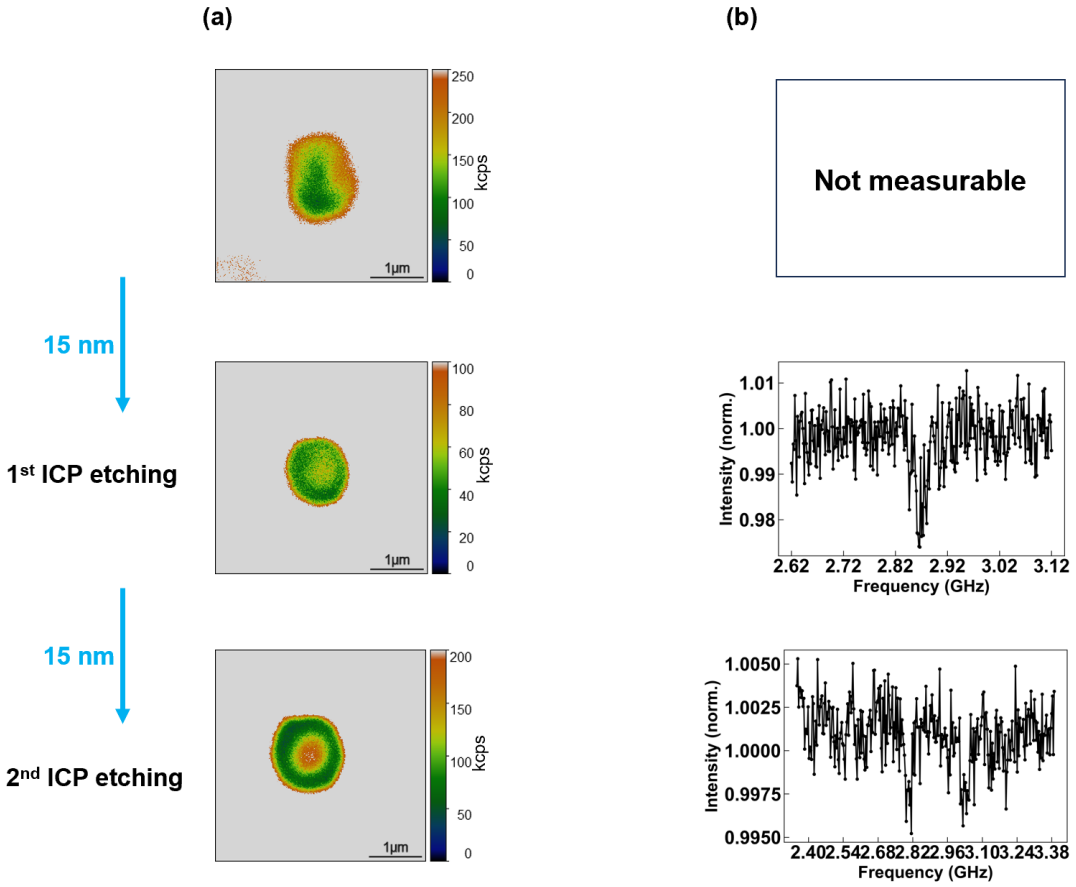

Fig. 3.24.(a) The PL images of 0.57 μm pillar before, after ICP etching with 15 nm, and after ICP etching with 30 nm. (b) The ODMR spectra of 0.57 μm pillar before, after ICP etching with 15 nm, and after ICP etching with 30 nm.

We couldn't find the pillar through the PL image before so that the ODMR of the 0.57 μm pillar is unmeasurable. After the ICP etching process, the PL images and ODMR spectra of the 0.57 μm pillar became measurable. However, the PL counts are extremely low with only 100 k counts/s, and the ODMR spectra are very noisy so that we still can't do other pulse measurements. The ODMR spectrum after the 1st ICP etching process only shows one dip, which is because we didn't apply the external magnetic field. The reason is that when we applied the external magnetic field, the spectrum became too noisy to observe the dip.

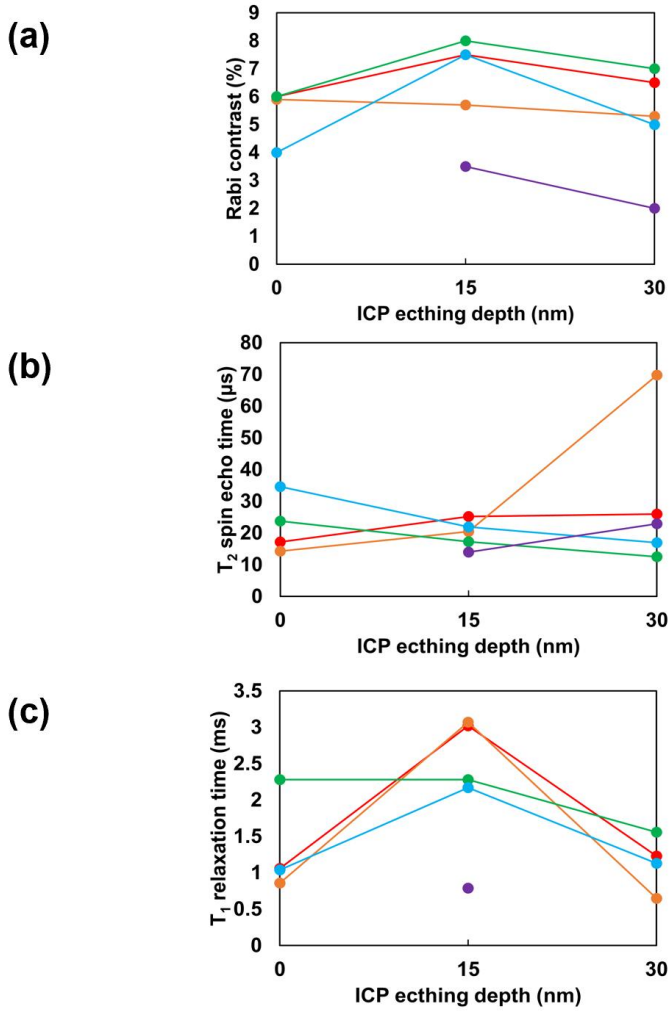

Fig. 3.25. Summary of (a) Rabi oscillation, (b)T_2 spin echo time, and (c)T_1 relaxation time results of 4.8 μm, 2.9 μm, 1.9 μm, 1 μm and 0.75 μm pillars.

The results of Rabi contrast, T_2 coherence time, and T1 relaxation time from 4.8, 2.9, 1.9, 1, and 0.75μm pillars are shown above. We can find a tendency that after the 1st ICP etching process, the Rabi contrast became stronger and the T_1 relaxation time became longer. However, after the 2nd CP etching process, they became worse, as well as T_2 time.

Although the spin properties of the pillars become worse after 30 nm ICP etching, the values are acceptable for applying them as scanning probes. Moreover, because the NV layer is closer to the diamond surface after ICP etching, it's possible to show a better scanning ability for the scanning probe.

For most of the pillars, the Rabi contrast increased after the first ICP etching process, but slightly or largely decreased after the second ICP etching. The increase of the Rabi contrast indicates an enhancement of the surface condition through the removal of the damaged layer (sp^2 hybridized amorphous carbon) and the termination of surface atoms by oxygen (in the form of ketone C=O or ether C–O–C bonds), which reduces the possibility of NV^- to NV^0 conversion. Rabi contrast is well known as an indicator of NV^- charge state stability. This is because the two charge states of NV, NV^- and NV^0, both emit fluorescence, but only NV^- is spin-dependent and can be coherently controlled by resonant MW irradiation. Therefore, the change in Rabi contrast indicates the change in the population of NV^- that is converted into NV^0, influenced by the charge environment condition at the surface of the diamond. A slight decrease in Rabi contrast after the second ICP etching may suggest that additional ICP etching could reintroduce damage to the diamond's surface.

T_2 spin echo time measured for the pillars shows a gradual increase or decrease after first and second ICP etching converging into the values between 12 – 25 μs, not showing strong etching depth dependence. Notably, at the small-size pillar with 0.75 μm after ICP etching, the T_2 spin echo signal recovered to a measurable quality. The observed less dependency for ICP etching depth as the NV centers come closer to the diamond pillar surface, and the diamond pillar sizes can be understood as the T_2 spin echo time serves as an indicator of the low-frequency (kHz – MHz) magnetic noise environment surrounding the NV centers, such as electron spins (P1 centers or defect-related $g \sim 2$ electron spins) and nuclear spins, which is more sensitive to the noise sources inside of the diamond pillar probe than the surface environment condition.

T_1 relaxation time measured for the pillars shows a rough trend that the T_1 value increases (from about 1 to 3 ms) after the first ICP etching (15 nm), and decreases to about 1 ms after the second ICP etching (30 nm) indicating strong dependence of surface condition and NV depth from the surface, similar to the case of Rabi oscillation contrast. Notably, at the small-size pillar with 0.75 μm after the first ICP etching, the T_1 value signal recovered to a measurable quality, while after the second ICP etching deteriorated again. These results may indicate NVs' sensitivity to an improvement in the surface defect condition due to the oxygen termination after the first ICP etching, and to the location depth at the near surface after the second ICP etching. T_1 is sensitive to rapidly fluctuating magnetic environments at the frequency of NV centers (~GHz). Such high-frequency noise may originate from lattice phonons, fluctuating electric and magnetic fields, or surface paramagnetic defects ascribed to dangling bonds with unpaired electron spins, resulting in a sensitive response surface condition.

As a result, diamond pillar probes with sizes larger than 1 μm were observed to have better or usable spin properties via the ICP etching process, which involved up to 30 nm removal of the diamond surface. However, for the smaller diameter pillar probes with 0.75 μm, the NVs condition to exhibit good values for all NV spin properties was not obtained after the second ICP etching process.

According to the results of small diameter pillars from TP1 diamond, they didn't have a good quality for measuring, which because the misalignment caused by thermal drift and significant damage due to the larger incident ion energy during FIB process. Therefore, we did FIB carefully for the TP2 diamond with small diameter 0.6 μm. Then, we did the ICP etching process on it with 25 nm and did the pulse measurement. The results of TP2 diamond are shown in Fig.3.26 and Fig.3.27.

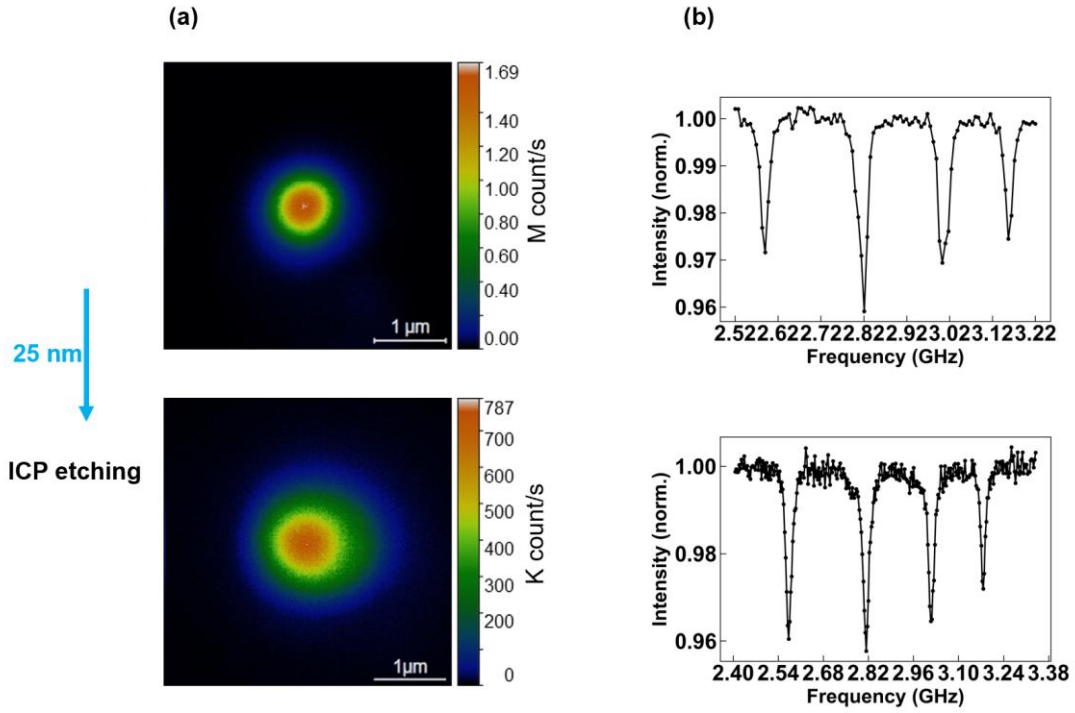

Fig. 3.26.(a) The PL images of the pillar from TP2 diamond before and after ICP etching with 25 nm. (b) The ODMR spectra of the pillar from TP2 diamond before and after ICP etching with 25 nm.

After the ICP etching process with 25 nm, the PL counts from the pillar of TP2 diamond decreased. This situation is similar to the results from pillars of TP1 diamond after the ICP etching process with 30 nm, because now the NV centers are close to the diamond surface.

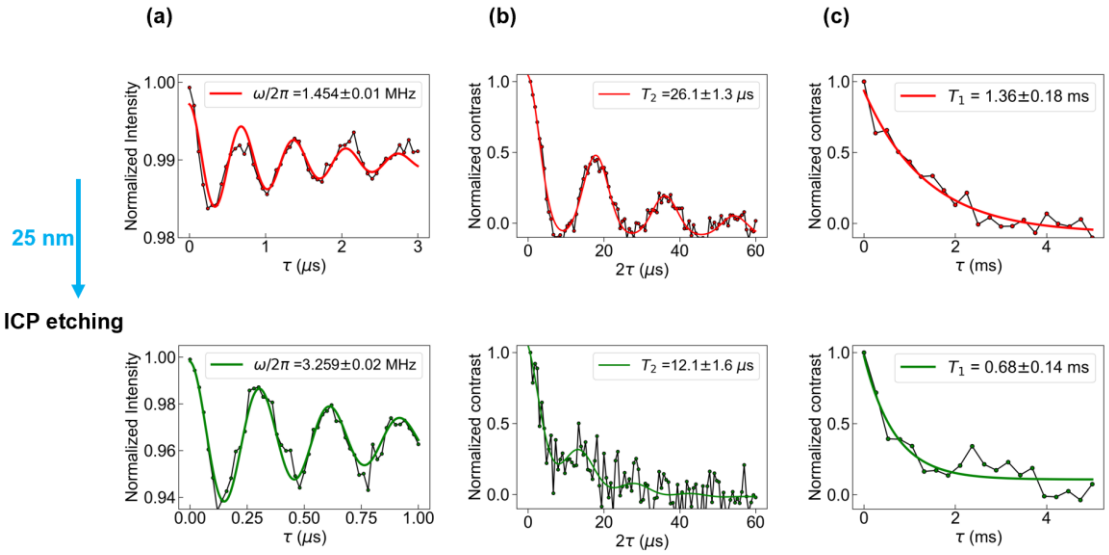

Fig. 3.27. (a) The Rabi oscillation spectra of the pillar from TP2 diamond before and after ICP etching with 25 nm. (b) The T_2 coherence time spectra of the pillar from TP2 diamond before and after ICP etching with 25 nm. (c) The T_1 relaxation spectra of the pillar from TP2 diamond before and after ICP etching with 25 nm.

This time we can measure the values with less noise for small diameter pillar. The results show that the T_2 coherence time and T_1 relaxation time of the pillar from TP2 diamond become shorter after the ICP etching process by 25 nm, which are similar to the results from pillars of TP1 diamond after the ICP etching process with 30 nm. The measured values keep good spin properties values before and after the 25 nm ICP etching, which gives us an expectation of high-quality NV pillar probes fabrication smaller diameter of less than 0.6 μm with a careful FIB-ICP etching process.

Chapter 4
Construction of a scanning NV probe microscopy

In Chapter 3, an NV center probe was fabricated by FIB. In Order to achieve the idea of using this probe to detect and image the magnetic structures from magnetic samples, an NV-AFM system was established. Therefore, Chapter 4 will introduce the details of this system.

4.1 Fabrication of printed circuit board (PCB)

To achieve the measurement for samples, the sample holder was designed and fabricated by printed circuit board (PCB) (Fig. 4.1.(a)) via the prototyping machine Eleven Lab (Fig. 4.1.(b)). A rectangular piece of the board (40 mm × 25 mm × 1.5 mm) was cut off from a big PCB with some drilling holes, and the copper of some parts from its surface was removed as designed (Fig. 4.1.(c)). The holes can be different according to the sample stage. The remaining copper would be used to connect by gold wire as a microwave microstrip line so that the microwave can be transported from one side to the other side and go through the sample, which is placed in the center of the board. Then, in order to receive the signal from the microwave generator, two subminiature version A (SMA) connectors were connected to the remaining copper by solder (Fig. 4.1.(d)).

(a) **(b)**

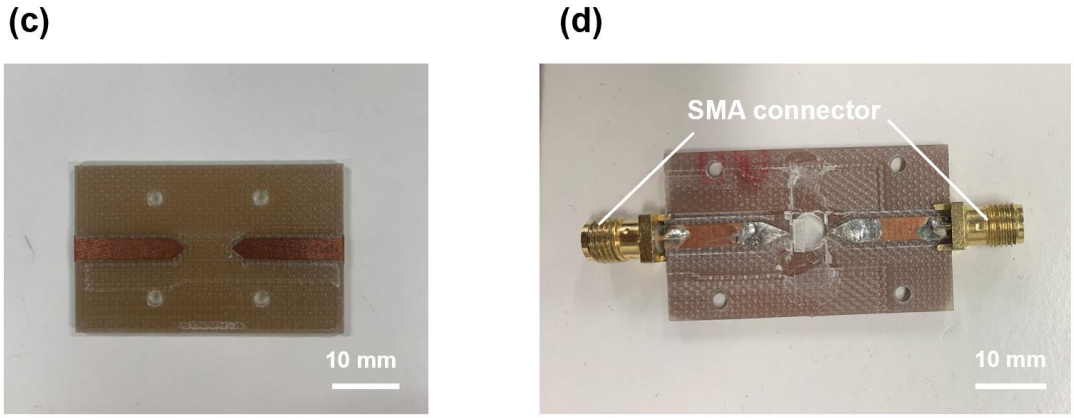

Fig. 4.1.(a) The PCB that is used for prototyping. (b) The prototyping machine Eleven Lab from An's lab. (c) The fabricated small PCB with holes and remaining copper serves as a sample holder. (d) The SMA connectors are soldered on the fabricated PCB.

Besides, in order to combine the fabricated NV center probe with AFM, a connecting PCB was also designed and cut off. We soldered three pin connectors on the PCB for connecting the board and AFM system (Fig. 4.2).

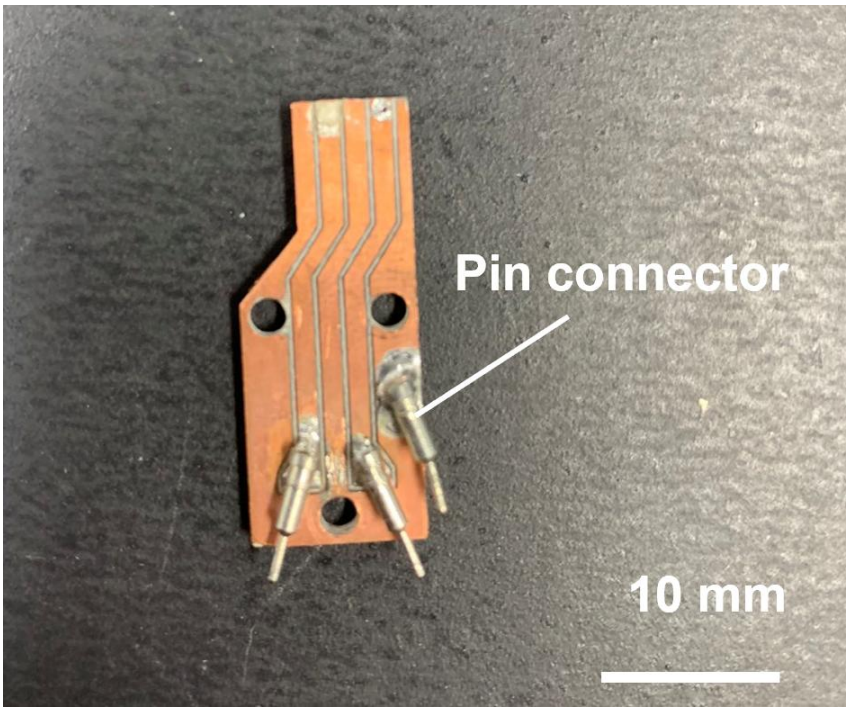

Fig. 4.2. The fabricated PCB soldered with three pieces of pin connectors.

4.2 The quartz tuning fork based atomic force microscopy (AFM)

The quartz tuning fork (Fig. 4.3) was used for AFM because of its high spring constant. The quartz tuning fork oscillates by electrical or mechanical excitation near its resonance frequency, and any interaction between the NV center probe and the surface of the magnetic sample shifts its oscillation, which can be detected and used to track surface topography with high sensitivity and spatial resolution [86] [87] [88].

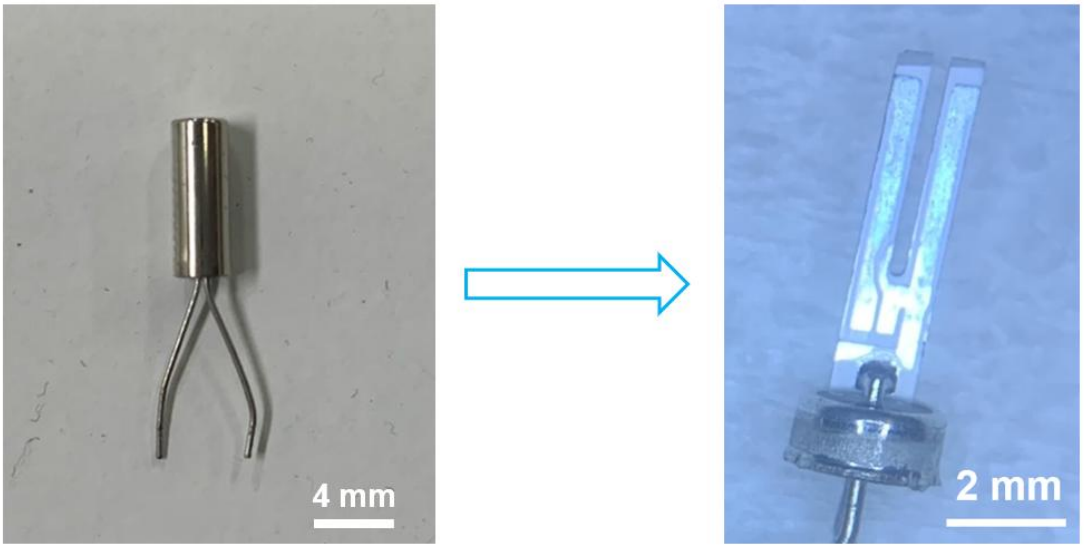

Fig. 4.3. The quartz tuning fork (AB38T-32.768KHZ from Abracon company) after removing the cap.

4.2.1 Fabrication of scanning NV center probe with a quartz tuning fork

A quartz tuning fork was soldered on the PCB that was fabricated in Chapter 4.1. A gold wire was used to connect position A and position B (Fig. 4.4.(a)). Then we stick this PCB that attaches the tuning fork to a small aluminum bulk (Fig. 4.4.(b)).

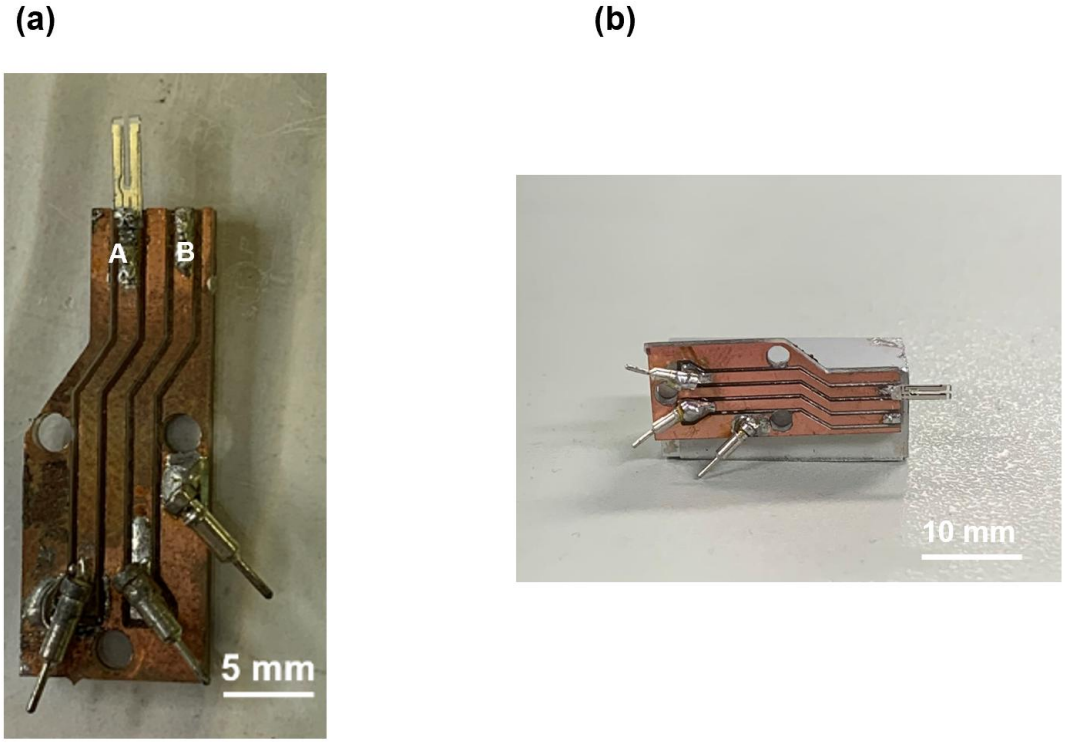

Fig. 4.4.(a) A tuning fork is soldered on a fabricated PCB. Position A and position B are connected by a gold wire. (b) The PCB is stuck to a small aluminum bulk.

For the fabrication of the scanning NV center probe, firstly, some silver paste was smeared on one cantilever's apex of the tuning fork. Then, an around 800 nm tungsten wire with 25 μm diameter was picked up by a tungsten-attached rod with a micromanipulator (Fig. 4.5.(a)) and put on the cantilever with paste. The apex of the 800 nm tungsten wire was also smeared with silver paste. Finally, the fabricated NV center diamond was picked up and attached to the apex of the 800 nm tungsten wire. Before the silver paste was hardened, we could adjust the angle and position of the diamond and 800 nm tungsten wire to make sure the diamond was parallel to the horizontal plane and the probe was at the lowest position (Fig. 4.5.(b)). When it was well-adjusted, we put the aluminum bulk into a heating box and heated it for 2 hours at 100 ℃. After that, we could add more silver paste around the diamond to reinforce it and heat it again.

(a)

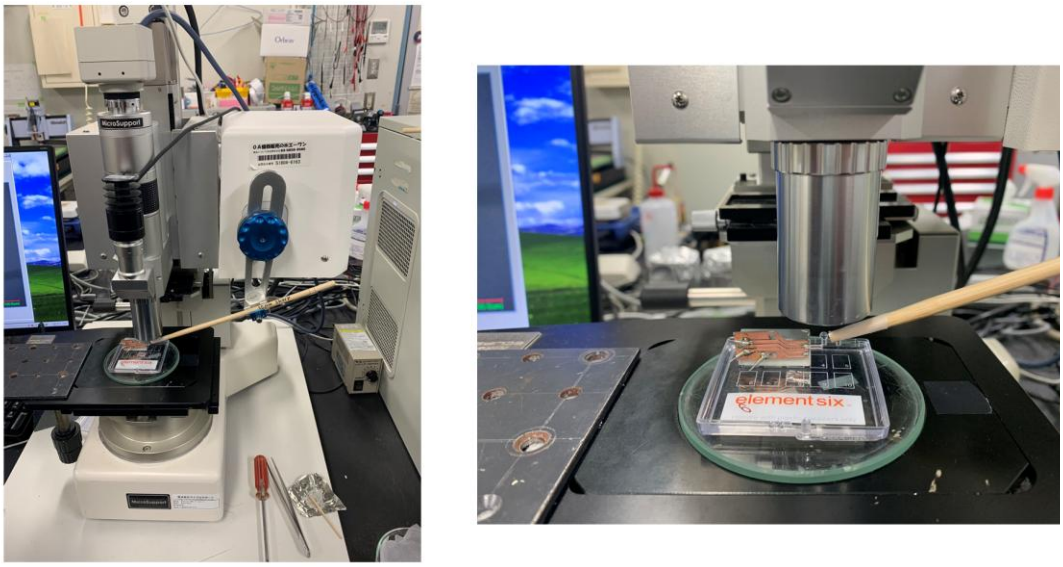

(b)

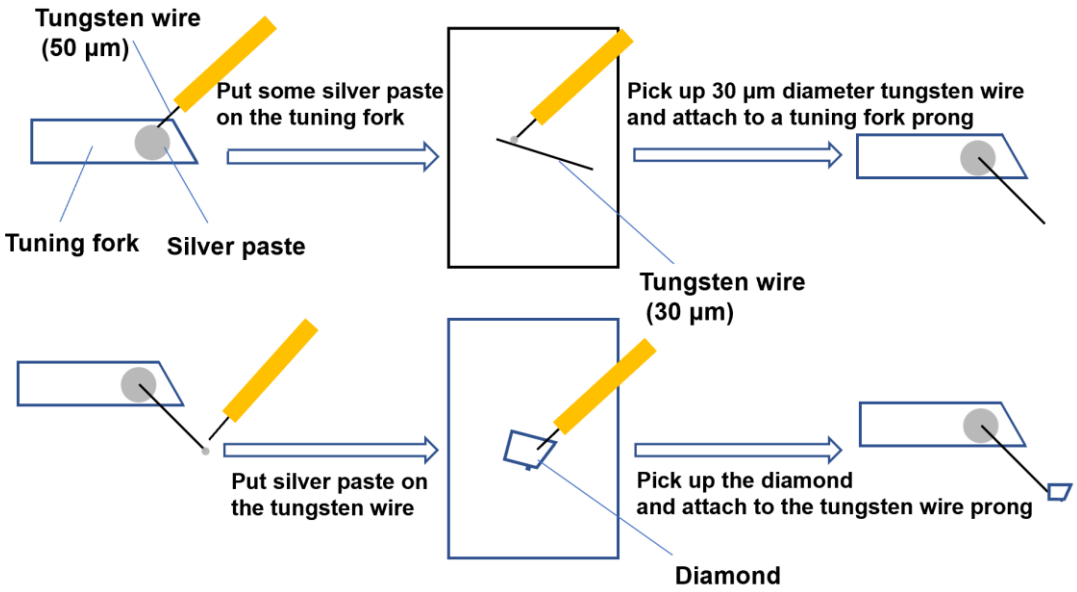

Fig. 4.5.(a) The micromanipulator AP-MC2 from MicroSupport company that used to fabricate the scanning probe. (b)The processing for fabrication of scanning NV center probe.

Until now, the fabrication of the scanning NV center probe has been finished. The fabricated NV center probe is shown in Fig.4.6. The pillar of the probe is located at the lowest position and is parallel to the horizontal line. We could connect this probe to the homemade AFM device and do the imaging measurements [89].

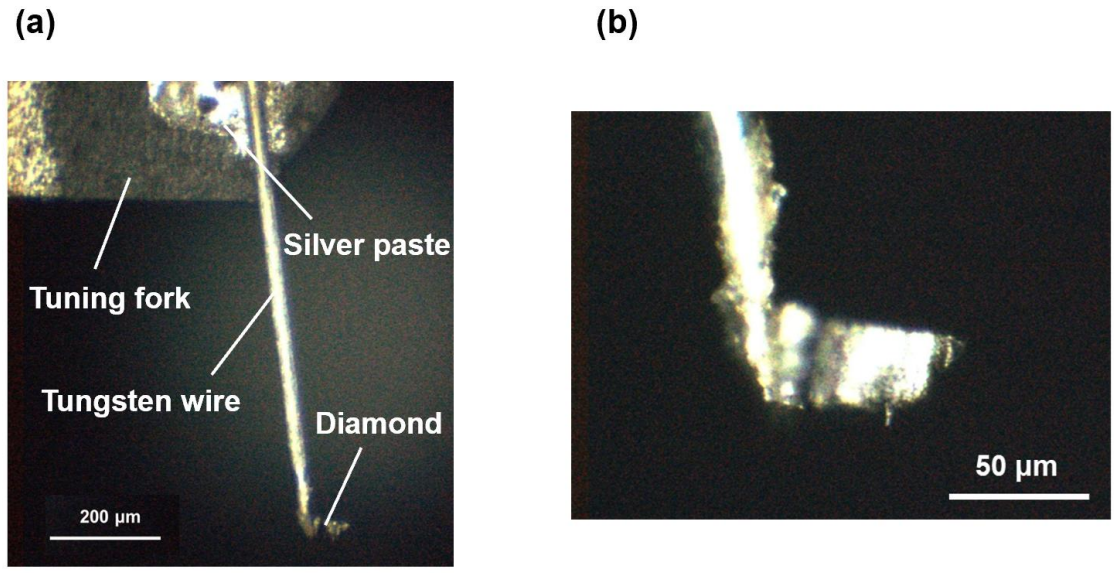

Fig. 4.6.(a) The diamond is attached to the wire and tuning fork. (b) The pillar on the diamond.

4.2.2 NV-AFM system

An AFM device with a confocal microscope was established by us. The microwave was generated by the signal generator (SG) and amplified by a radio-frequency (RF) amplifier.

The sample with a microwave microstrip line was placed on a tube scanner (Fig. 4.7.(a)), which can be controlled to move along the X, Y, and Z axes so that the scanning movement could be achieved. The fabricated scanning NV center probe was attached to a piezo motor (Fig. 4.7.(a)) which could also move along the X, Y, and Z axes. We controlled the motor through a high voltage source (Fig. 4.7.(b)) to make the scanning probe approach the sample surface according to the feedback signal from the tuning fork (Fig. 4.7.(c)) and determined the initial scanning position. The signal from the tuning fork could be increased by an amplifier (Fig. 4.7.(d)).

The laser was reflected by a dichroic mirror, and adjusted by a Galvano mirror and two achromatic lenses so that it was focused on the objective lens of the microscope and could irradiate the fabricated probe. After that, the generated fluorescence signal from the

scanning probe was received and detected by an avalanche photodiode (APD). This NV-AFM system is shown in Fig.4.8.

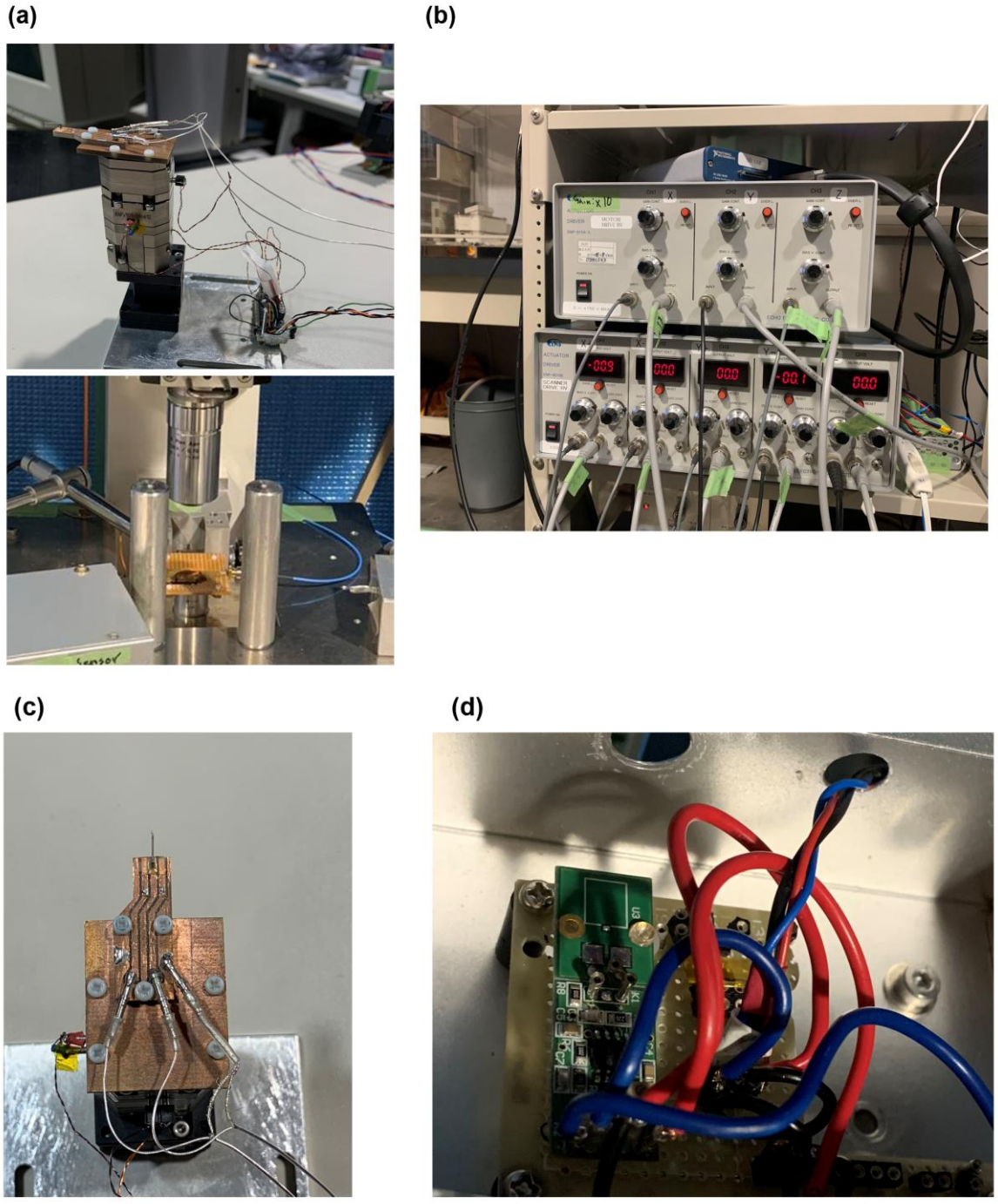

Fig. 4.7.(a) The piezo motor that can control the movement of the fabricated scanning NV probe, and the sample is connected with microwave and placed on a tube scanner. (b) The high voltage source to drive the piezo motor and tube scanner. (c) The wire on the PCB for transporting the signal from the tuning fork. (d) The pre-amplifier for increasing the tuning fork signal.

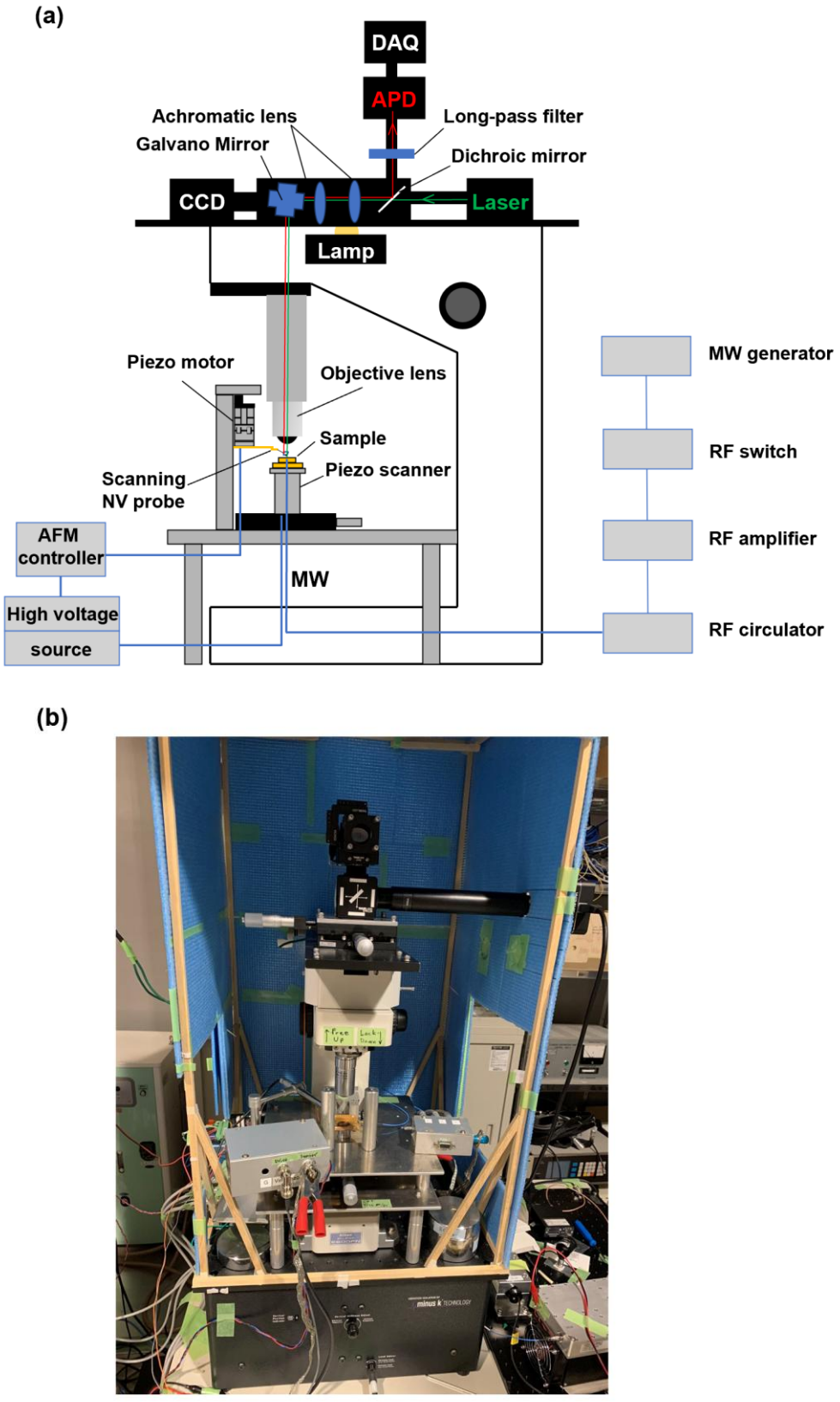

Fig. 4.8.(a) The NV-AFM system. (b) The NV-AFM device in An's lab.

Chapter 5
Magnetic domain imaging via a scanning NV probe

5.1 Experimental procedure

When we established the NV-AFM system, we could start to do the scanning experiment to image the magnetic structures from the magnetic samples. First, we observed the magnetic structures with the magneto-optic Kerr effect (MOKE) microscope to confirm the existence and shape of the magnetic structures. Then we can approach the scanning NV center probe to the surface of the magnetic samples and do the imaging.

5.1.1 Observation of magnetic structures

Before the imaging of magnetic samples, MOKE images were observed by microscope. MOKE is a technique used to visualize and study the magnetic properties of materials by detecting changes in the polarization of reflected light due to the magnetization of the magnetic material. It occurs when polarized light reflects off a magnetized surface and its polarization state changes when facing the magnetic field from the surface. MOKE imaging is widely used for observing magnetic domains, domain walls, and magnetization processes in thin films and magnetic materials [90]. To obtain the Kerr image, two polarizers (Fig. 5.1) were placed into the optical system before the objective lens, and when we rotated one of the polarizers, the Kerr images could be observed (Fig. 5.2) [91].

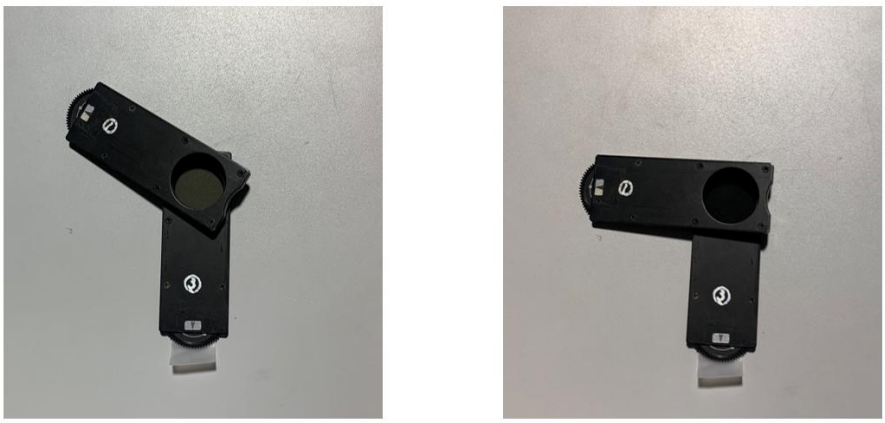

Fig. 5.1. Two polarizers with different polarization directions.

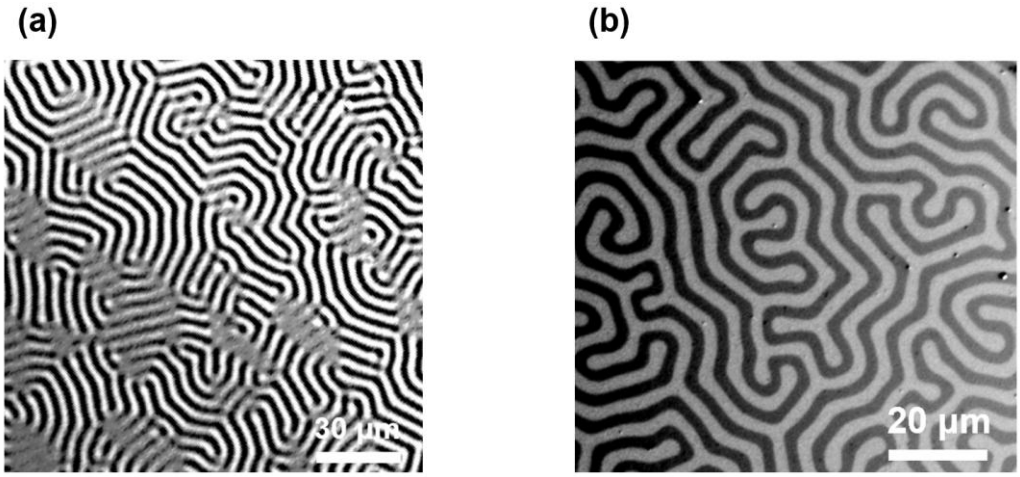

Fig. 5.2.(a) The Kerr image of a magnetic garnet sample. (b) The Kerr image of the Sm sample.

In this research, two kinds of magnetic samples called Bismuth Lutetium iron garnet (BLG) (Fig. 5.3.(a)) and Yttrium iron garnet (YIG) (Fig. 5.3.(b)) were observed by MOKE microscope, and the magnetic structures (magnetic domains) (Fig. 5.4) from them were shown to us.

Moreover, we tried to apply a scanning microwave during the observation of the magnetic samples, and the magnetic domains transformed like bubbles, which were called bubble domains (Fig. 5.5) [92]. In general, the magnetic moments in magnetic domains are aligned in opposite directions (up and down) to each other. When the external field is increased, the magnetic moment antiparallel to the magnetic field flips to the other one and finally becomes a uniform magnetic structure. Just before this, isolated domains like a circle shape can be formed where the direction of the magnetic moment inside the bubble is only opposite to that of the outside.

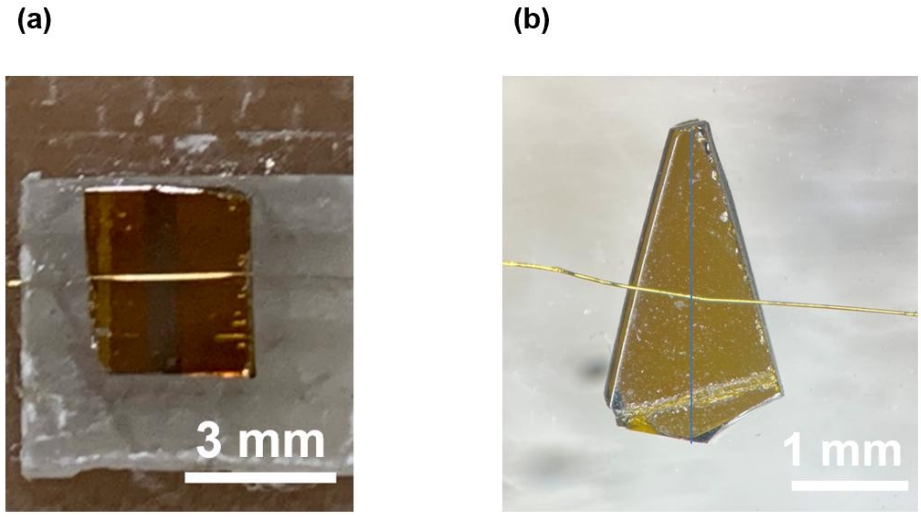

Fig. 5.3.(a) The BLG sample. (b) The YIG sample.

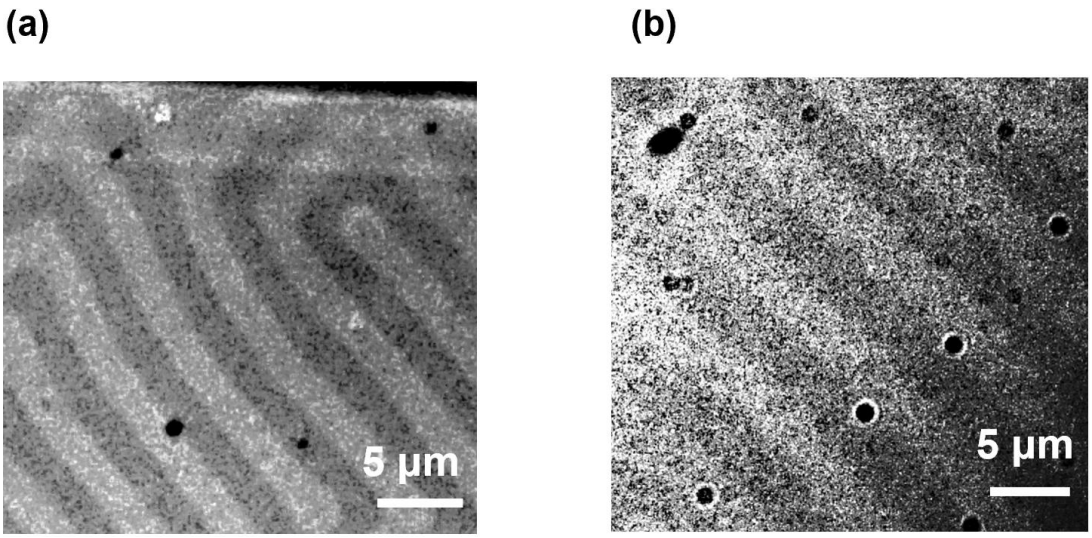

Fig. 5.4.(a) The magnetic domain Kerr image of BLG. (b)The magnetic domain Kerr image of YIG.

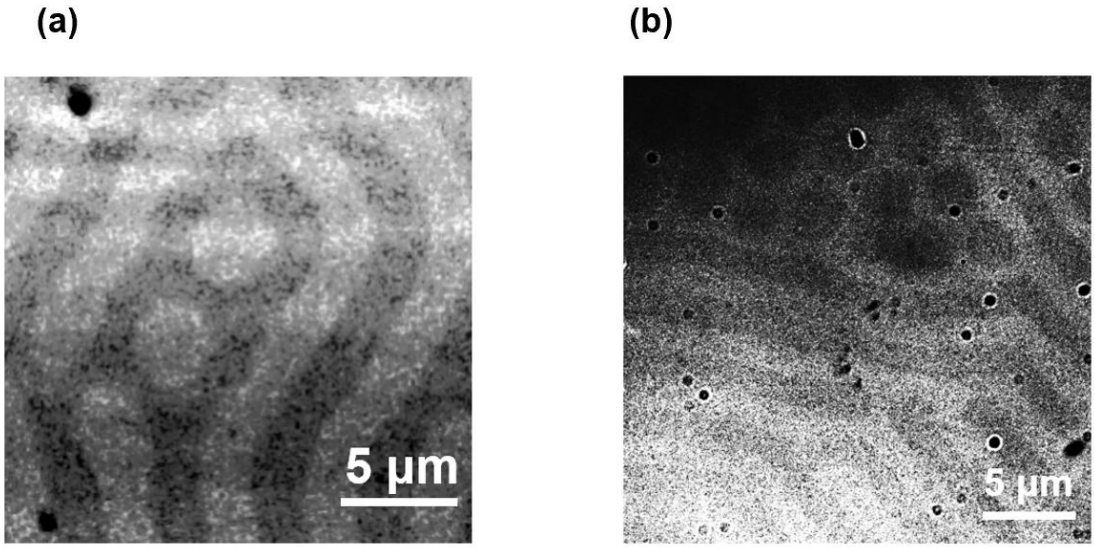

Fig. 5.5.(a) The magnetic bubble domain Kerr image of BLG. (b)The magnetic bubble domain Kerr image of YIG.

5.1.2 Imaging of magnetic domains by the scanning NV probe

After observing the magnetic domains from the sample, we chose a scanning area and approached the scanning NV center probe by controlling the Z-axis of the piezo motor (Fig. 5.6.(a)). The controller of the motor could get the feedback of the vibration signal from the quartz tuning fork, therefore, the approaching process stopped when the probe was maximum extent close to the sample surface. The feedback for the distance between the probe and the sample surface maintained a constant height during the measurements of both topography and PL images.

Then, the sample was moved through the tube scanner by applying a voltage to achieve the scanning process. When the scanning NV center probe scanned across the sample surface, the laser illuminated the probe and both topographic and magnetic information could be acquired at the same time (Fig. 5.6.(b)). For the topographic imaging, the interaction forces between the sample surface and the quartz tuning fork caused the cantilever of the tuning fork to deflect. The deflection in the cantilever changed the position of the reflected laser to achieve precise measurement of the interaction between the sample surface and the quartz tuning fork [93]. The feedback from the tuning fork provided information on the sample surface height at each point. Each position was recorded to create a topographic image with high resolution.

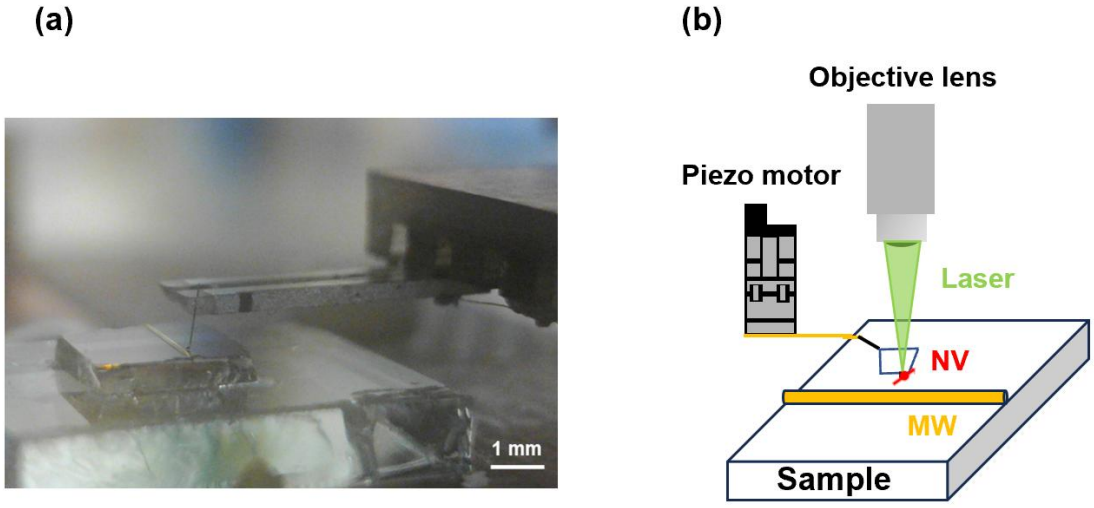

Fig. 5.6.(a) The CCD image that shows the NV center probe approaching the sample. (b) The schematic of sample scanning by an NV center probe.

As for imaging of magnetic domains, the stray fields from the magnetic samples were detected by the NV centers (Fig. 5.7.(b)). The direction of the stray field is uncertain at different positions of the sample. Therefore, when the scanning NV center probe scans across the sample, the angle between the stray field and NV centers is different for each point. When the NV center is parallel to the stray field, the fluorescence intensity is strong, while if they are perpendicular to each other, the fluorescence intensity will be extremely weak, which leads to the brightness and darkness in the PL images acquired by scanning (Fig. 5.7.(a)) [94].

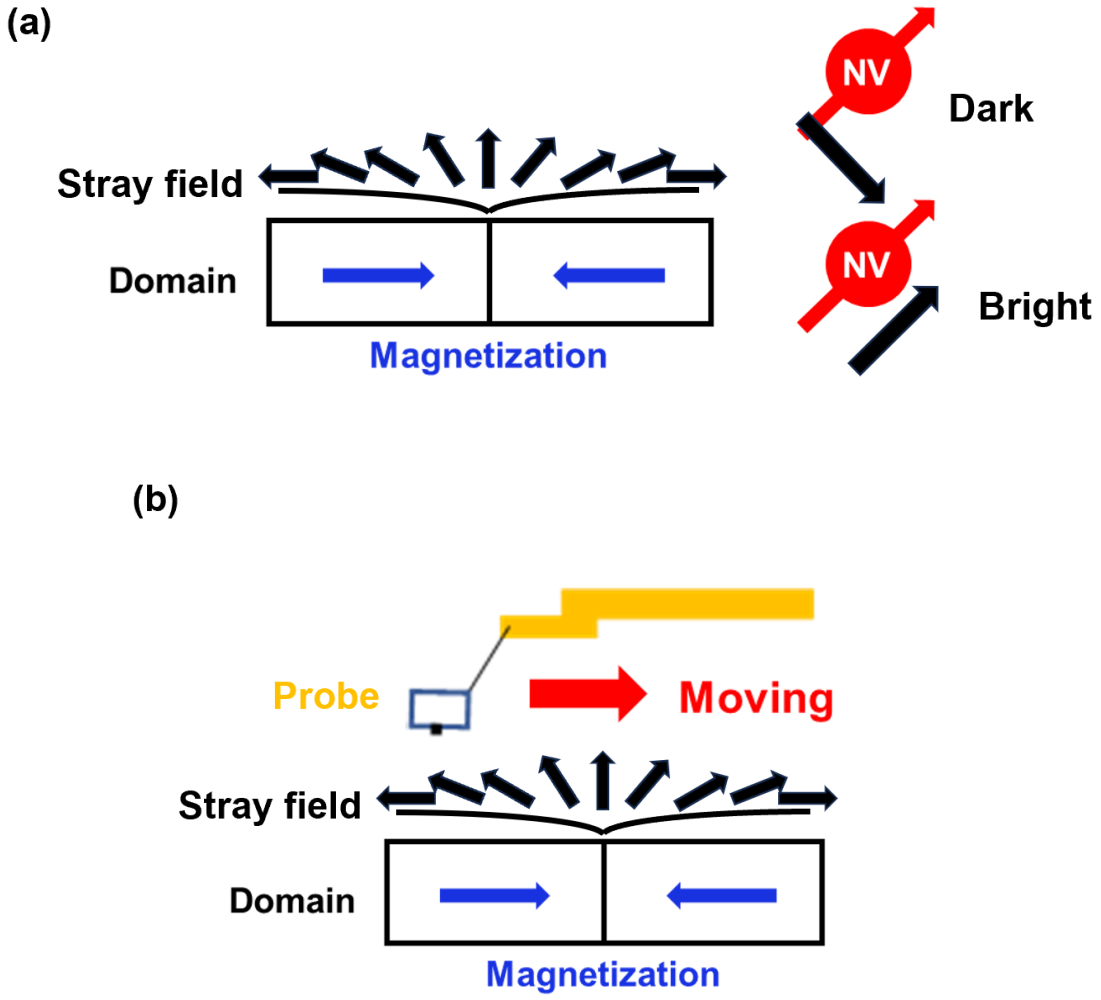

Fig. 5.7.(a) The direction between the NV center and the stray field from the magnetic sample. (b) The probe is scanning across the magnetic sample.

5.2 Results and discussion

We scanned the BLG and YIG samples via a fabricated scanning NV center probe, about which the information is shown in Fig. 5.8. This probe was combined with an AFM system so that the PL images and topographic images from BLG and YIG samples were acquired. (Fig. 5.9 and Fig. 5.10).

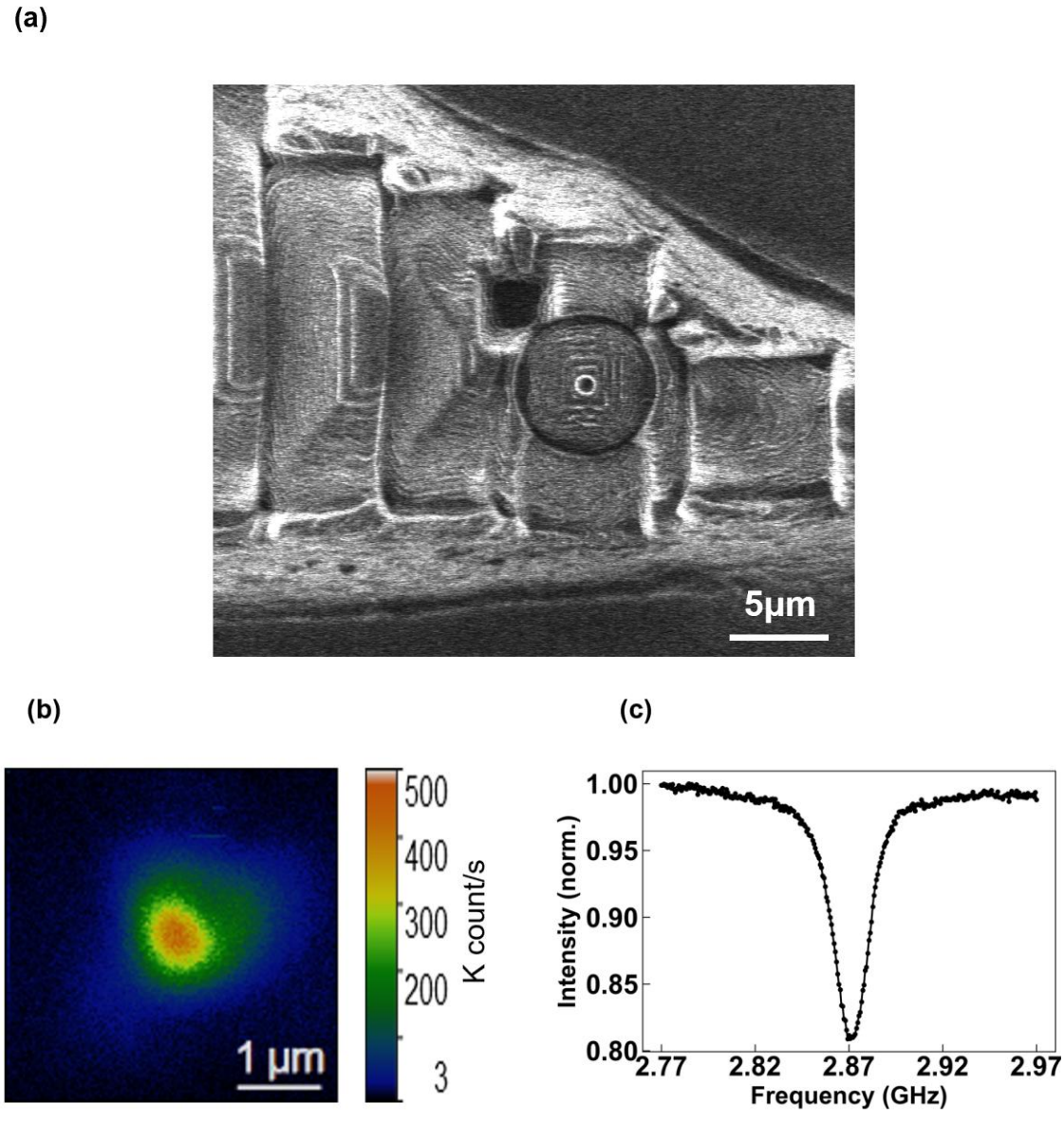

Fig. 5.8.(a) The SIM image of the fabricated diamond after the FIB process. The diameter of the pillar is around 0.8 μm. (b) The PL image of the pillar. (c) The ODMR spectrum of the pillar.

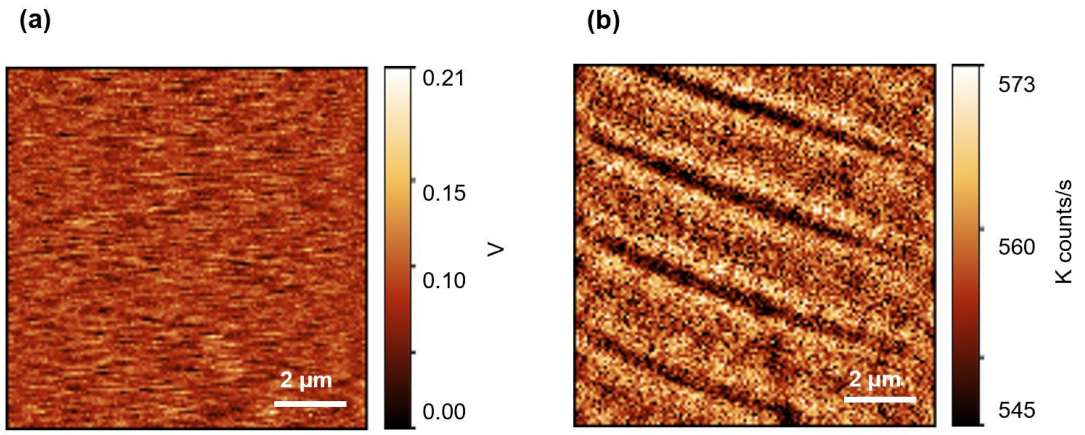

Fig. 5.9.(a) The topographic image of BLG. (b) The PL image of the domain from BLG.

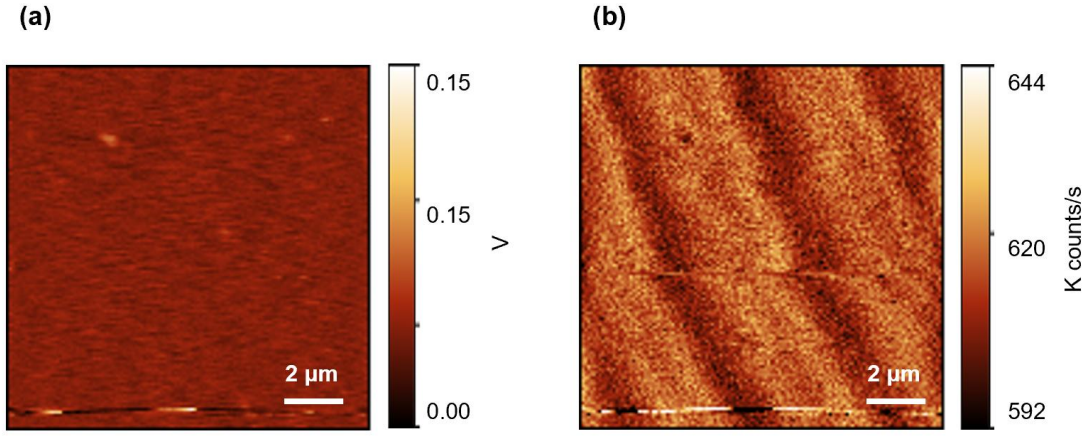

Fig. 5.10.(a) The topographic image of YIG. (b) The PL image of the domain from YIG.

For the normal magnetic domains, both of them showed clear PL images, and we can distinguish the shape of the domains from the images.

However, for created bubble domains (Fig. 5.11 and Fig. 5.12), we could only observe the domains from BLG, while the domains from the YIG were hard to identify. The reason may be that the stray field from YIG is much weaker than BLG, and the properties of the scanning NV probe are not good enough.

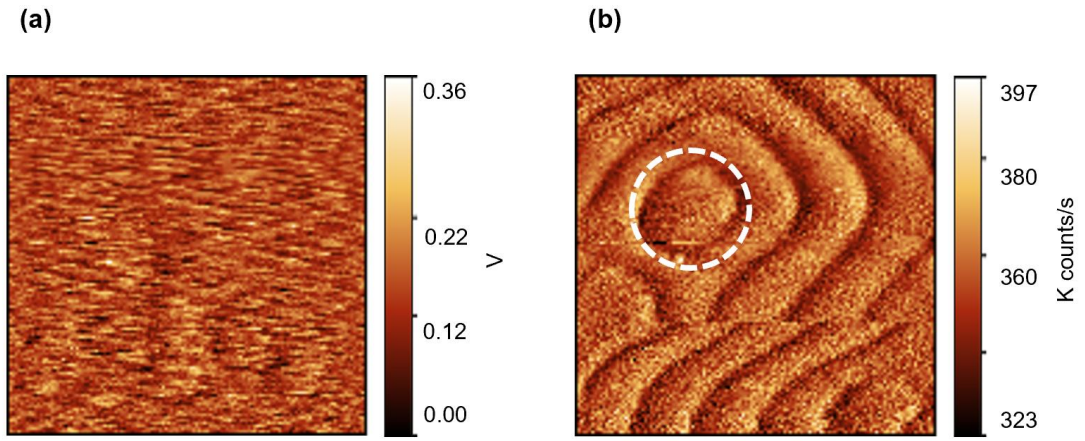

Fig. 5.11.(a) The topographic image of BLG. (b) The PL image of the created bubble domain (white circle part) from the BLG.

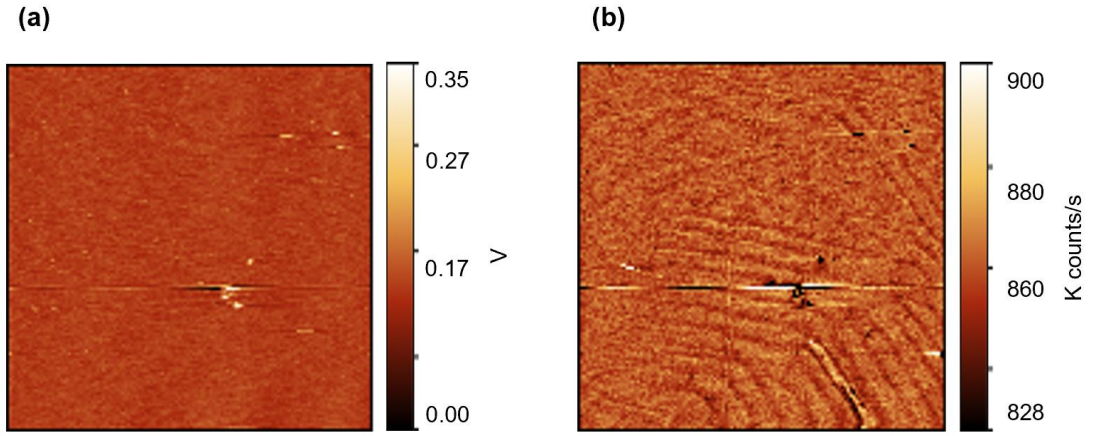

Fig. 5.12.(a) The topographic image of YIG. (b) The PL image of the created bubble domain (white circle part) from the YIG.

Therefore, we should improve the properties of the scanning NV center probe. After the ICP etching process, the elevated probe could image the sample more precisely.

Chapter 6
Summary and Outlook

6.1 Summary

We can summarize this research in three parts. The first part introduced the procedure for the fabrication of an NV center diamond. We implanted $^{14}N^{+}$ ions into the diamond to create NV centers and cut the diamond into triangular pieces. Then we did FIB on the diamond surface to fabricate a pillar with around 800 nm as a probe. We confirmed the NV centers were alive in the pillar by measuring the PL intensity and ODMR of the pillar. However, during the FIB process, some residual damage occurred and affected the properties of the NV centers in the pillar.

Therefore, the second part revealed the efforts we made to recover the properties of the NV in the pillar by ICP etching. We etched six pillars (with diameters 4.8 μm, 2.9 μm, 1.9 μm, 1 μm, 0.75 μm, and 0.57 μm) for 30 nm by soft ICP after FIB, and in order to verify the effect of the ICP etching, we did measurements of ODMR, Rabi oscillation, spin echo, and T_1 relaxation for each pillar before and after the ICP etching process. The results showed that after the ICP etching process with 15 nm, Rabi oscillation contrast was higher, T_1 relaxation was longer, and even the measurement for small diameter pillars could be achieved, confirming that the ICP etching process can improve the properties of the NV centers. Although after the ICP etching process with 30 nm, these spin properties become worse, the values are still acceptable for scanning probes and the closing to the diamond surface for NV layer makes it more sensitive during the scanning process. Moreover, we could achieve the spin properties recovery of smaller diamond pillars via ICP etching if we improve the skills for FIB process.

The third part explained the application for the fabricated NV center probe. We fabricated a scanning NV center probe by attaching the diamond pillar to a quartz tuning fork and combined it with a homemade AFM confocal microscope. By using this NV-AFM system, we achieved the measurement for imaging the magnetic domains, which could be observed via the MOKE microscope, from magnetic samples BLG and YIG. From the acquired PL images and the topographic images from the samples, we understood that the imaged domains were clear for BLG, while the domains were not clear for YIG. That meant our scanning NV center probe was not good enough for imaging samples with a weak magnetic field. Therefore, we did soft ICP etching on the scanning probe to improve the properties of the scanning probe so that we can achieve imaging the bubble domains.

6.2 Outlook

Based on this research, we can make further improvements to the scanning NV center probe in the future. For example, we can decrease the diameter of the pillar during the FIB process by using a smaller donut pattern. To avoid the drift of the milling, we can pause the process for a short time and adjust the milling position again. We could also reduce the energy of Ga^+ ions during the FIB process so that less damage will influence the diamond.

As for the ICP etching, we can continue trying different etching depths and find the optimal depth for the improvement of NV center properties. And also, we can try to do it without washing the Pt-Pd coating, and then etch the pillar for more nanometers.

Although after the ICP etching process with more than 30 nm, the properties of NV centers become worse, we can still use them as scanning NV center probes because the NV centers are closer to the diamond surface. We can try to scan some magnetic samples with weaker magnetic fields that are hard to image using the probe after the ICP etching process.

Acknowledgement

I would like to extend my deepest gratitude to many people who have supported and guided me throughout the process of completing this thesis. First and foremost, I am profoundly indebted to my supervisor, Assoc. Prof. Toshu An, whose unwavering support, insightful guidance, and invaluable feedback have been instrumental in shaping the direction and quality of my research on the fabrication of scanning NV center probes. And I'm grateful to Assoc. Prof. Jumpei Ueda, Prof. Yoshifumi Oshima, Prof. Yukiko Takamura, Assoc. Prof. Masashi Akabori from JAIST and Assoc. Prof. Hiroki Morishita from Tohoku University for providing me guidance and advice. Their dedication to academic excellence and personal mentorship has been instrumental in completing my thesis.

I also wish to extend my heartfelt thanks to Assoc. Prof. Abdelghani Laraoui and his students Rupak Timalsina, Adam Erickson, Suvechhya Lamichhane, Ben Hammons, and Tianlin Li from the University of Nebraska-Lincoln for helping me finish the wide-field NV center experiments. We spent three fulfilling and happy months in Lincoln, and I'm excited that our results from the experiment will be published. And also, thanks to Prof. Toshiharu Makino and his team for supporting me with the ICP etching process.

My sincere appreciation goes to my fellow classmates and friends Dwi Prananto, Kunitaka Hayashi, Kasane Noda, Thitinum Gas-osoth, Takashi Kageyama, Yuma Aoki, Shunsuke Uesugi, Akito Fukuoka from An's lab, for helping me do the experiments and solving the problems of life and research, and Cunjian Lin, Hirohisa Miyata, Yuki Shigemura from Ueda's lab, for studying and working together.

Finally, I would like to deeply gratitude to my family, my parents and my brother, for their unwavering support and understanding so that I could study and live in Japan. Their constant encouragement and belief in my abilities have been the bedrock upon which I have built my academic pursuits

To all who have contributed to this thesis, your support has been invaluable, and I am sincerely thankful.

Appendix A

List of instruments

For optical components:

1. Laser source: MLL-U-532B-50mW, Changchun New Industries.

2. Achromatic lens: AC254-200-A, Thorlabs.

3. Galvano mirror: GVS202, Thorlabs.

4. Mirrors: PF10-03-P01, Thorlabs.

5. Plano-Convex Lens: LA1509-YAG (200 mm and 100 mm), Thorlabs.

6. Dichroic filter: FF552-Di02-25x36, Thorlabs.

7. ND filter: FW2AND, Thorlabs.

8. Long pass filter: FELH0600, Thorlabs.

9. CCD camera: L-835, HOZAN.

10. Objective lens: LMPlanFL 100×/0.8 BD, OLYMPUS.

11. Single-mode fiber: 633- 780 nm, FC/PC, Ø3 mm Jacket, Thorlabs.

For pulse measurement:

1. Signal generator: SG6000F, DSI Instrument.

2. RF switch: ZYSWA-2-50DR, Mini-Circuits.

3. RF amplifier: ZVA-183-S+, Mini-Circuits.

4. Circulator: H02S01, Chengdu Bocen Microwave Technology.

5. Amplifier: ZHL-15W 422-S+, Mini-Circuits.

6. DAQ: USB-6210, National Instruments.

7. AOM: C1250, ISOMET.

8. APD: SPCM-AQRH 14, Excelitas Technologies.

Appendix B

Grid mapping of magnetic sample via NV-AFM system

During the AFM scanning of bubble domains from the YIG sample via a fabricated scanning NV center probe, we can do ODMR measurements at the same time. We chose 20 × 20 (20 for the X axis and 20 for the Y axis, a total of 400) points as a grid to measure the ODMR with a wide frequency range of 0.5 ~ 4 GHz, and the grid PL images were obtained. Here we pick up eight points of them (Fig. B.1), and their ODMR spectra are shown in Fig. B.2. The PL images at frequency f = 1.39 GHz, f = 1.39 GHz, and f = 1.39 GHz were shown in Fig. B.2.

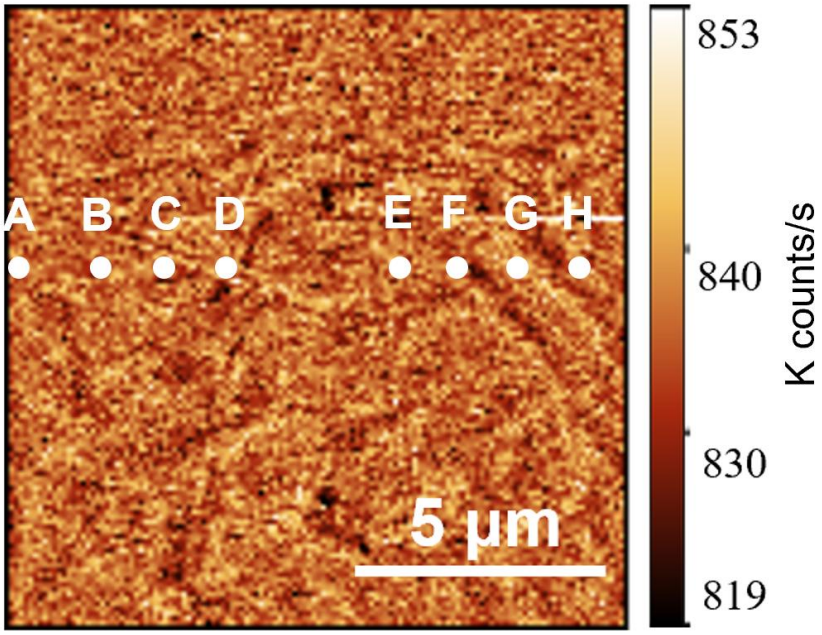

Fig. B.1. The PL image of the YIG sample. Eight points A, B, C, D, E, F, G, and H are marked on the PL image.

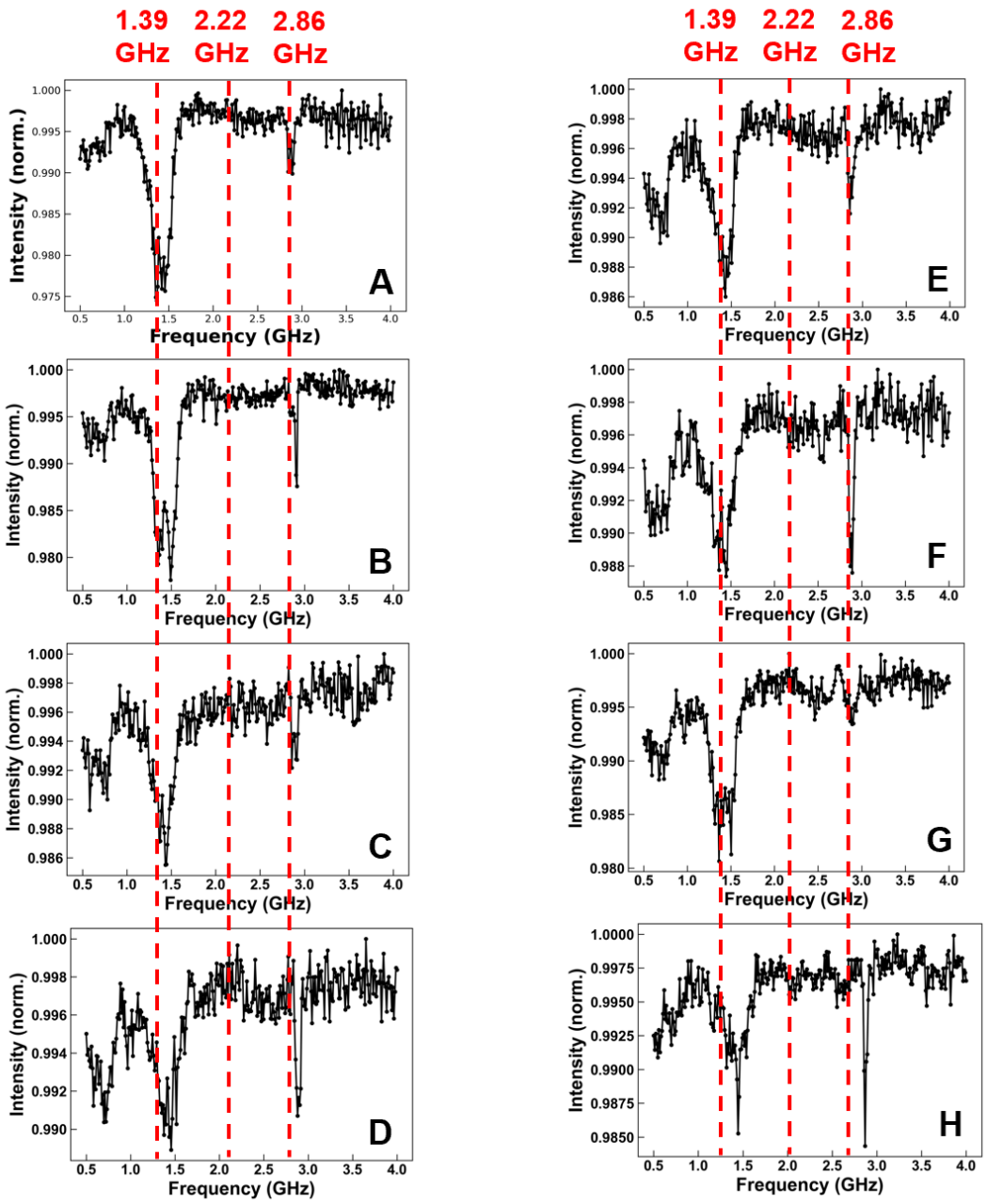

Fig. B.2. The ODMR spectra of eight points A, B, C, D, E, F, G, and H from Fig. B.1. We compare these spectra by adding three red lines at frequencies 1.39, 2.22, and 2.86 GHz.

The ODMR spectra of the eight points show different shape position dependence of scanning position, especially the frequency around 1.4 GHz and 2.9 GHz. Then, if we fix the frequency at 1.39, 2.22, and 2.86 GHz, we can clearly see the differences in the ODMR shape at each frequency, and the PL images at different frequencies are shown below.

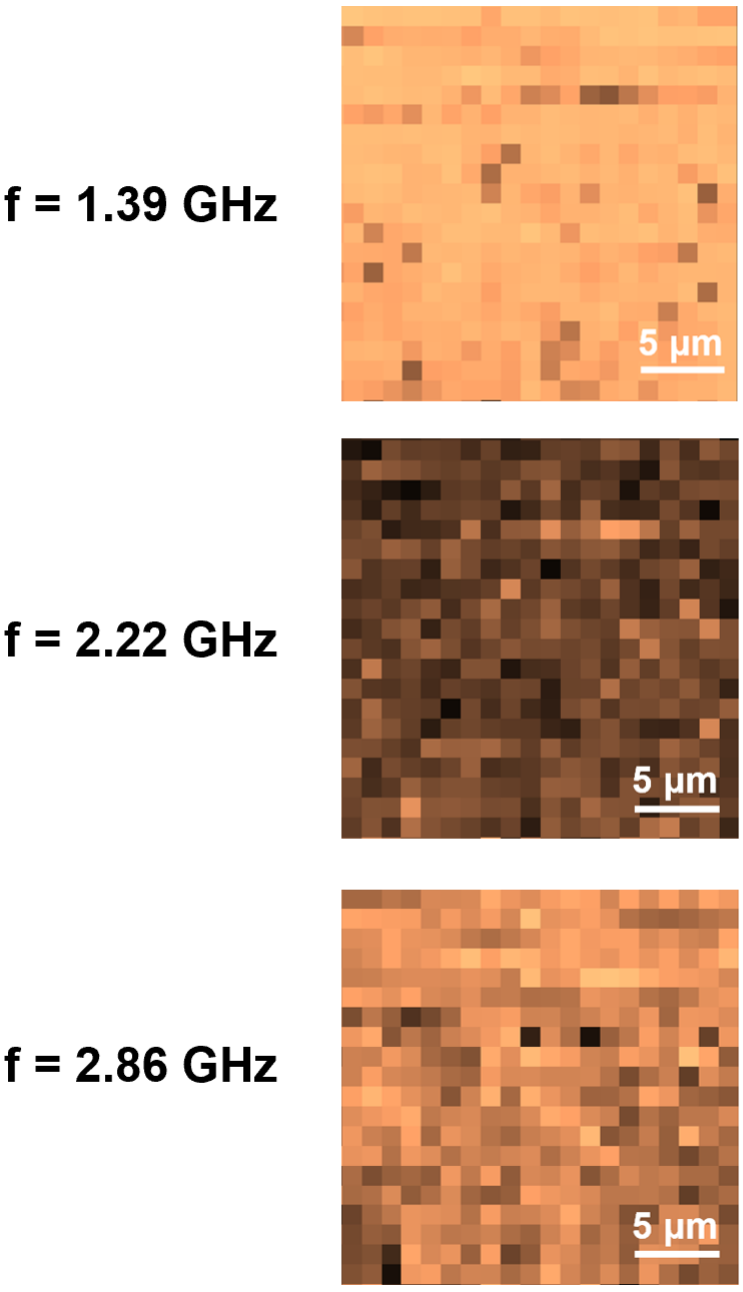

Fig. B.3. The PL images of grid mapping at 1.39, 2.22, and 2.86 GHz.

The PL images also show different intensities at different frequencies for every point, which means different magnetic field exists and the domains from the points are different. Therefore, we can make sure that the bubble domain exists and the fabricated scanning NV center probe is workable, although we can't image the domains from YIG clearly with the probe.

Appendix C

The direction between the NV axes and the external magnetic field

In Chapter 2, we introduced that in the NV center structure, the N-V axes could have four different directions, and according to the Zeeman split, if we apply an external field to the NV center, we can get an ODMR spectrum with eight dips (Fig. C.1) [95].

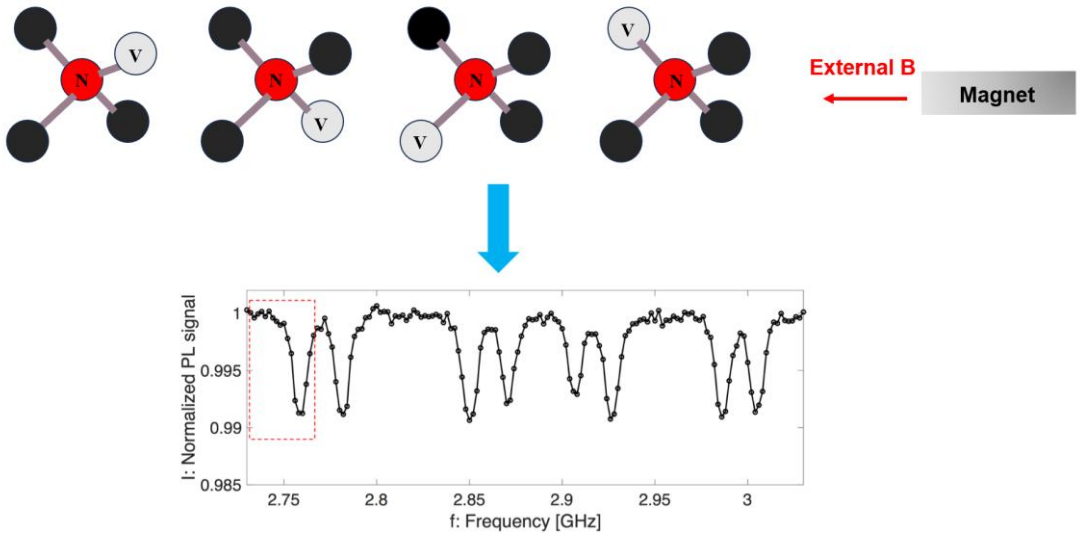

Fig. C.1. The ODMR spectrum with 8 dips by applying an external magnetic field to the NV center axes.

However, in Chapter 3, we adjusted the permanent magnet and made the magnetic field from the magnet parallel to one of the N-V axes so that we got ODMR spectra with only four dips. The center two dips are from the splitting of the parallel axis, and the outer two dips are from the splitting of the other three axes because the external magnetic field shows the same angle with the other three axes.

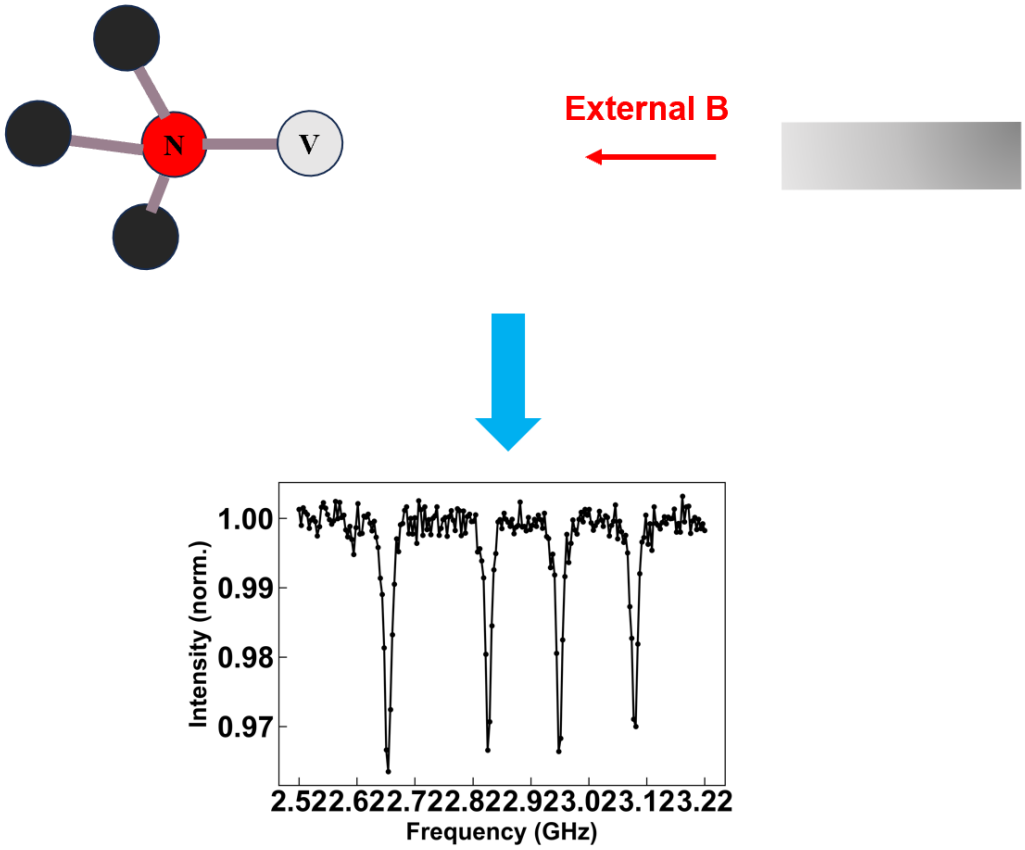

Fig. C.2. The ODMR spectrum with 4 dips by applying an external magnetic field parallel to one of the NV center axes.

Appendix D

The ICP etching process on NV center diamond

There are other etching techniques, such as reactive ion etching (RIE), for etching the diamond. However, the plasma density and ion energy of RIE are linked, while they are independently controlled during ICP etching, so that RIE needs a stronger ion bombardment. Due to the lower plasma density and ionization efficiency, RIE has less efficiency for diamond etching and provides more damage to the diamond surface. Therefore, we chose to use ICP etching for diamond etching with higher etching efficiency and less damage to the diamond surface. Moreover, the past normal ICP etching process still leaves some damage on the diamond surface, which may influence the properties of the NV centers. Recently, T. Makino and his group from AIST started to decrease the ion energy and power during the ICP etching, which is called soft ICP etching, to reduce the damage on the diamond surface, and we also followed this process.

In this research, we did soft ICP etching on the NV center diamond with a mixture of 95 sccm O_2 and 2 sccm CF_4 gas under lower power voltage (around 300 W) and zero bias voltage. In some other ICP etching process, H_2 is used instead of O_2. However, the H doesn't break the C-C bonds in diamond so that it takes a long time for the etching process. Moreover, the H proton on the diamond surface can provide a nuclear spin that influences the spin properties in NV centers. Usually, the negatively charged NV^- is sensitive to the magnetic field and affects the coherence time T_2 of NV centers. The H on the diamond surface may change the NV^- to NV^0 or generate NVH^- that causing the decoherence and shortening the coherence time T_2. Additionally, hydrogen terminated diamond surface shows band bending and the NV^- states become unstable to be converted to NV^0 Therefore, we chose O_2 as the ICP etching gas.

The O atom can combine with the C dangling bond and terminate the diamond surface. Oxygen radicals react with carbon in the diamond to form CO and CO_2, enabling material removal. Fluorine-based chemistry improves etching selectivity and smoothness while reducing unwanted surface roughness. The equations during the ICP etching process can be shown as:

O_2 drives the main etching reaction, reacts with carbon in the diamond to form volatile CO and CO_2:

$$C + O_2 \rightarrow CO_2$$
$$2C + O_2 \rightarrow 2CO$$

$$C + O_2^+ \rightarrow CO + O^+$$

CF_4 enhances the etching rate and surface smoothness, Fluorine radical reacts with carbon in diamond to form volatile CF_4:

$$CF_4 + e^- \rightarrow CF_3 + F^-$$

$$C + 4F \rightarrow CF_4$$

After the FIB fabrication process for diamond pillar and washing it with aqua regia, it is possible that H_2O, C-OH, C-O-C, and C=O will be present on the pillar surface. After ICP etching, because we used $O_2(O^+)$ plasma during the ICP etching, the O could make bonding with the C dangling bond on the diamond surface and terminate the surface, which was beneficial to the surface properties. It is expected that after the ICP etching process, the number of H_2O and C-OH decreases while that of C-O-C and C=O increases (Fig. D.1), where C-O-C stabilizes NV^- states. Moreover, by using the CF_4 plasma during the ICP etching, the etched surface could be smoother (Fig. 2)

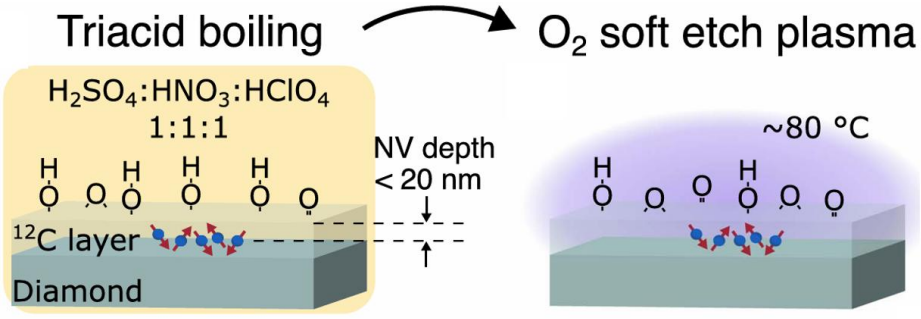

Fig. D.1. The surface condition before and after soft etching. (from J. Fuhrmann, et al., Mater. Quantum. Technol. 4, 041001 (2024))

Appendix E

Stray field imaging of WS_2 flakes by Nitrogen-vacancy center magnetometry

Two-dimensional (2D) magnets are emerging as platforms for novel physics and spintronic applications. Tungsten disulfide (WS_2) flakes, predicted to exhibit ferromagnetism, have yet to be extensively studied for their magnetic properties. In this work, we employ nitrogen-vacancy (NV) center magnetometry to investigate the magnetic behavior of Fe-implanted WS_2 flakes. The flakes, transferred onto a diamond substrate embedded with NV centers, were imaged using NV wide-field microscopy (NV-WFM) to map the magnetic stray fields. Our measurements confirmed the presence of stray fields at the edges of the flakes. These findings provide experimental evidence of the magnetic properties of WS_2 flakes, highlighting their potential for spintronic applications.

E.1 Introduction

2D materials are a class of materials characterized by a thickness of just one or two atomic layers, extending in two dimensions (length and width) while remaining extremely thin in the third dimension. These materials, particularly when arranged in heterostructures, exhibit unique physical, chemical, and mechanical properties due to their reduced dimensionality and high surface-area-to-volume ratio. Compared to bulk crystals, 2D magnets offer advantages such as easier, lower-cost fabrication and a wide range of control mechanisms, making them and their heterostructures promising candidates for next-generation spintronic devices [96].

2D materials attracted more and more attention after the discovery of graphene [97]. However, because of the lack of a nonzero bandgap, other 2D materials like transition metal dichalcogenides (TMDs) and hexagonal boron nitride (h-BN) were explored and studied

TMDs with common formula MX_2, where M is a transition metal and X is a chalcogen, have been widely studied because of their broad range of electronic properties. These TMDs have a hexagonal structure, with each monolayer comprising three stacked layers (X-M-X) [98].

2D van der Waals magnetic material WS_2 (Fig.E.1) [99], is one of the most representative TMDs that attracted increasing attention due to its direct bandgap and

semiconducting properties. However, the magnetic measurement of WS_2 is limited, especially for the flakes [100]. Therefore, this research focused on the imaging of magnetic field from WS_2 flakes.

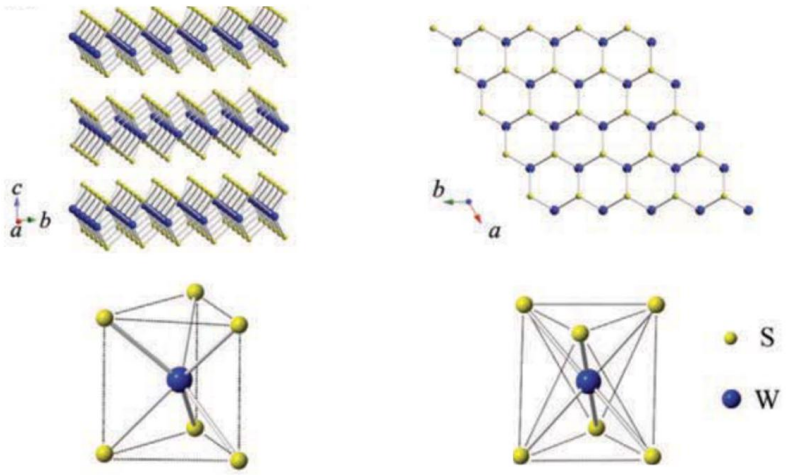

Fig. E.1. The crystal structure of WS_2.

E.2 Experiments

We used NV wide-field microscopy to image the magnetic stray fields from Fe-implanted WS_2 flakes. Prior to the NV measurements, the flakes were transferred from an Au-coated SiO_2/Si substrate to a diamond substrate. We then performed atomic force microscopy (AFM) scanning to determine the thickness of the flakes, providing crucial information for subsequent analysis.

We selected one of the WS_2 flakes, lifted it from the Au-coated SiO_2/Si substrate at room temperature, and transferred it onto the diamond substrate using the standard high-temperature dry transfer method with polypropylene carbonate (PPC) transfer stamps. The thin flake was accompanied by a protective top layer of hexagonal boron nitride (h-BN) on the PPC.

After being transferred to the diamond, the WS_2 flake was scanned by AFM to determine its height. Two regions (region A and B) were selected for scanning (Fig.E.2). We also did a line-cut on the AFM image of the WS_2 flake and found that the height for region A is around 70 nm, while the region B is around 45 nm (Fig.E.3).

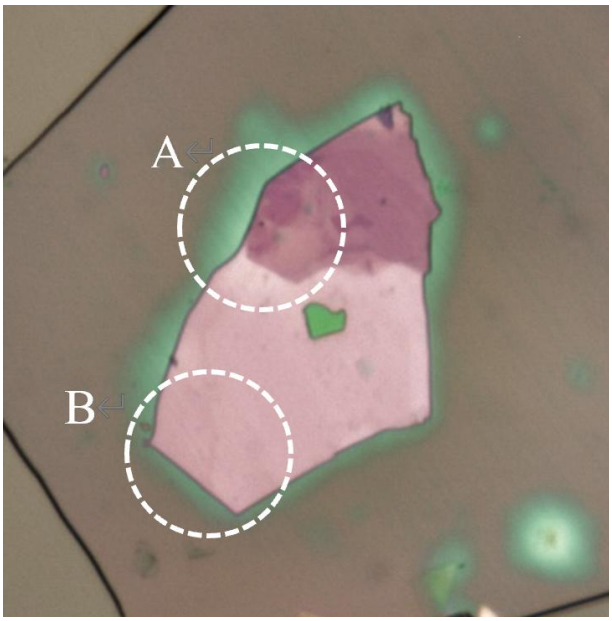

Fig. E.2. The flake of WS_2 covered by h-BN. We did AFM on region A and region B.

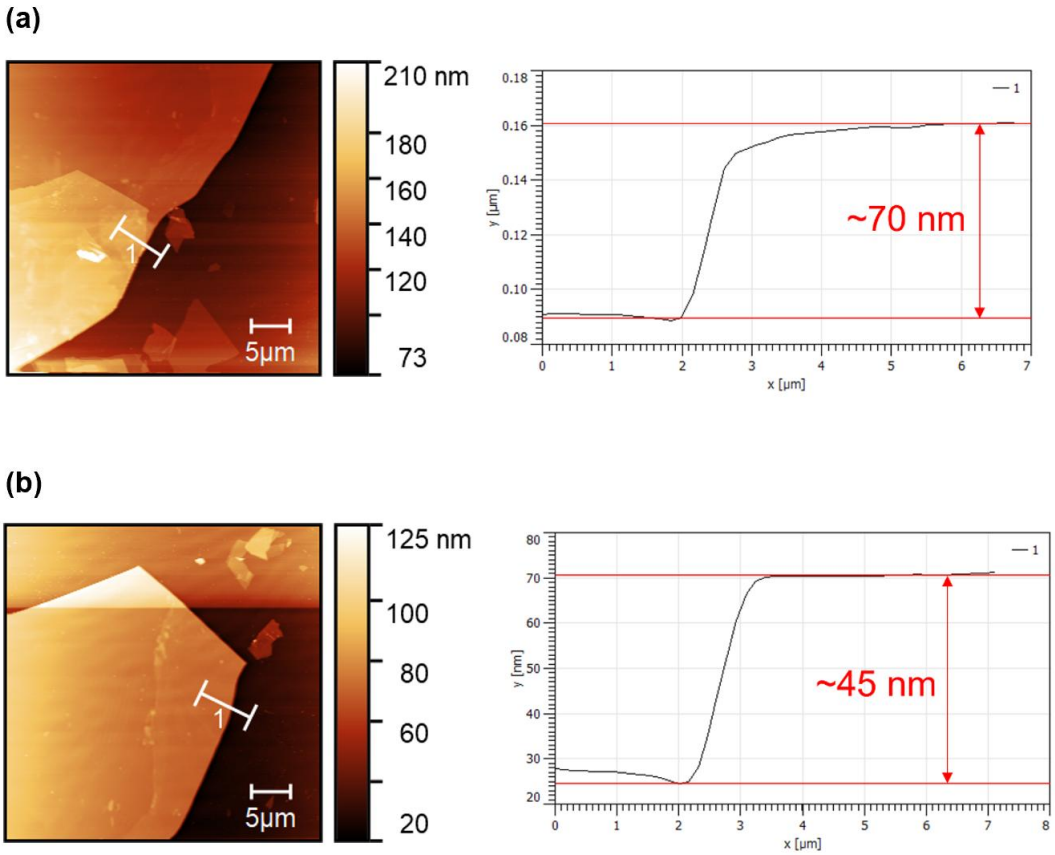

Fig. E.3.(a) The AFM and line-cut images of Region A. (b) The AFM and line-cut images of Region B.

After the AFM scan, we conducted NV magnetic mapping of the WS_2 flake to determine the stray field B_{st} from the flake's edge using NV-WFM (Fig.E.4(a)), employing a home-made ODMR system combined with an sCMOS camera. The diamond substrate with the WS_2 flake was fixed onto a glass coverslip with patterned gold loops (Fig.E.4(b)), which served for spin excitation. This assembly was mounted on an XYZ motorized stage. An objective lens positioned below the stage focused a 532 nm laser and collected the resulting fluorescence from the flake, directing it to the sCMOS camera. Microwaves were generated by a signal generator and passed through microwave amplifiers. These were swept across the f_- and f_+ spin transitions (where we define the $m_s = 0$ to $m_s = -1$ as f_-; $m_s = 0$ to $m_s = +1$ as f_+). The generated pulse was then sent to an oscilloscope for monitoring. Meanwhile, permanent magnets were positioned around the diamond to magnetize the WS_2 flake with an external magnetic field B_{ex} . The position and orientation of the magnets were adjusted to control the strength of B_{ex} and to align the magnetic field for optimal ODMR signal detection on the oscilloscope. In this study, we varied B_{ex} from a low field to a high field (5 mT to 60 mT) and imaged the WS_2 flake under different magnetic field strengths. As a result, the NV magnetic maps, which show the B_{st} from the WS_2 flake, were obtained by performing ODMR measurements.

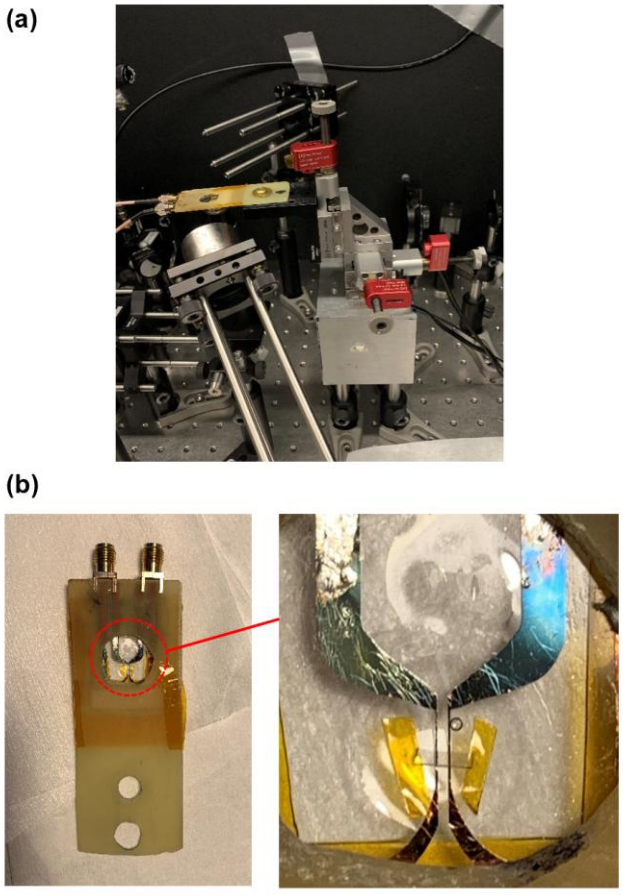

Fig. E.4.(a) The NV-WFM system. (b) The sample is fixed on a glass cover slip.

E.3 Results

For the hBN-covered Fe-implanted WS_2 flake, we selected three regions for the NV magnetic mapping (Fig. E.5). In each region, we adjusted the permanent magnets to apply external magnetic field B_{ex} of 5.5 mT, 11.6 mT, 24.1 mT, 33.5 mT, 44.9 mT and 63.2 mT. At each B_{ex} we swept the microwave frequency across the f_- and f_+ spin transitions to generate the NV magnetic maps, simultaneously capturing fluorescence images. Line-cuts (x is distance(μm), y is magnetic field (μT)) were performed on the NV magnetic maps along the edge of the WS_2 flake to determine the stray field B_{ex} from the flake's edge. (Fig. E.6).

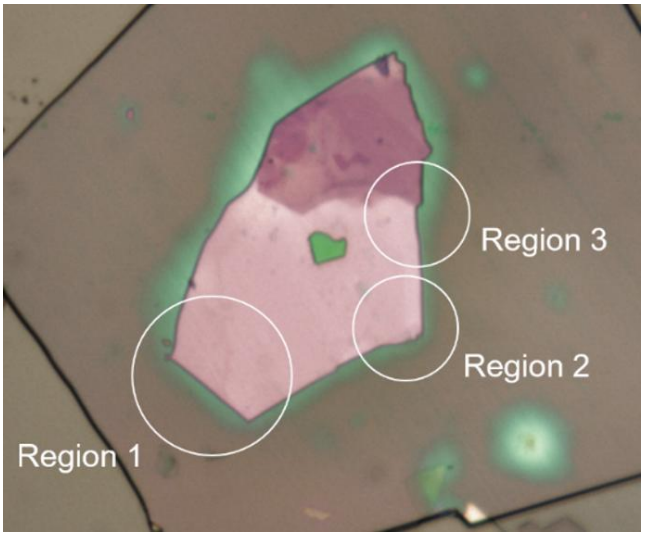

Fig. E.5. The three regions of the WS_2 flake that were chosen to do the measurements.

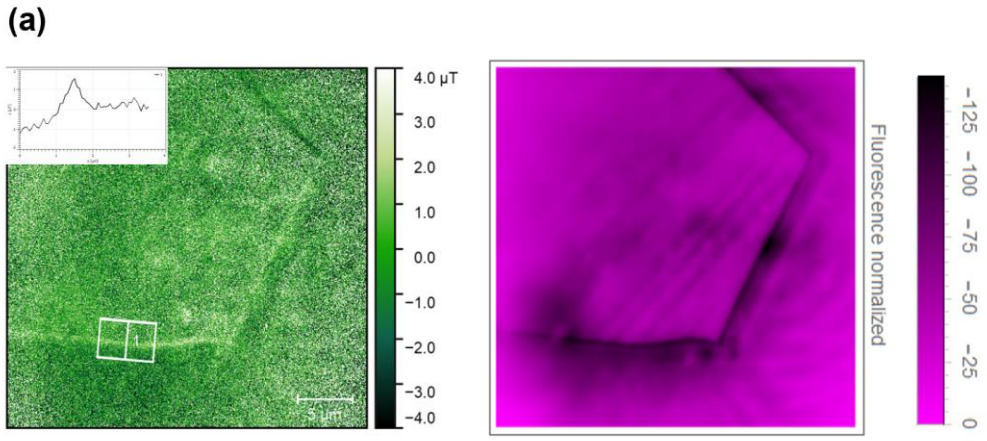

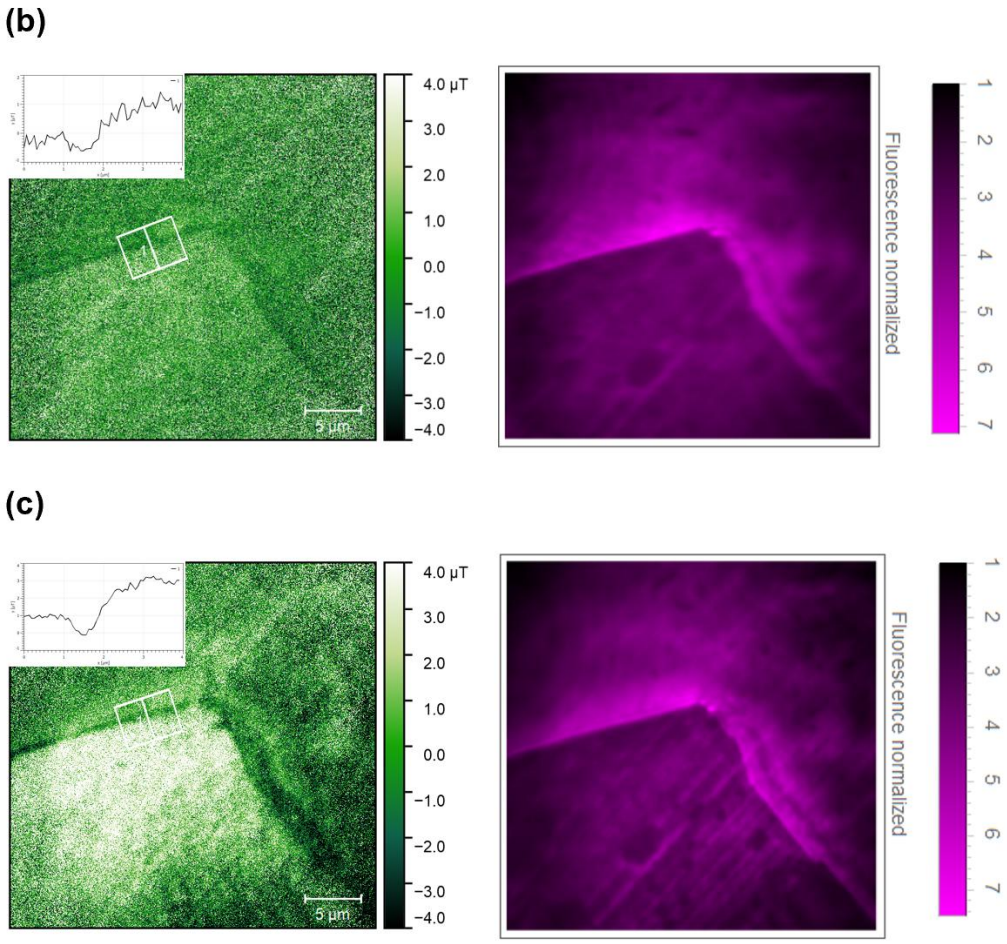

Fig. E.6. The NV magnetic images with line-cut (left) and fluorescence images (right) of region 1 (a), 2 (b), and 3 (c) at 11.6 mT.

From the line-cuts of the NV magnetic maps, we recorded the ΔB_{st} intensity (ranging from 0.5 to 4 μT) along the edge of the WS_2 flake under external magnetic fields B_{ex} of 5.5 mT, 11.6 mT, 24.1 mT, 33.5 mT, 44.9 mT, and 63.2 mT. In all the regions, an increasing trend in the ΔB_{st} was observed as the B_{ex} is increased (Fig. E.7).

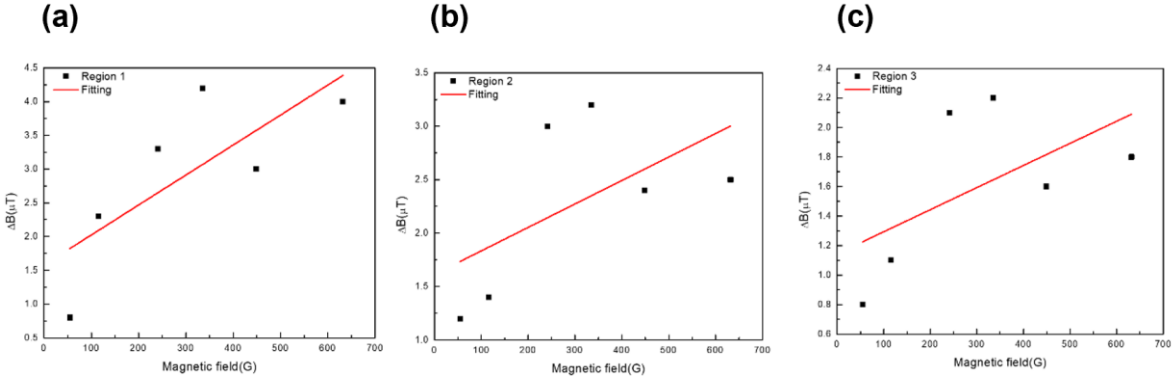

Fig. E.7. B_{ex} dependence of ΔB_{st} intensity from the edge of the WS_2 flake for 3 regions.

Additionally, we did T_1 relaxation measurements for fixed f_- and f_+ under external magnetic fields B_{ex} of 5.5 mT, 11.6 mT, 24.1 mT, 33.5 mT, 44.9 mT, and 63.2 mT. Then, we performed T_1 imaging for the f_- and f_+ separately under the same range of B_{ex} in region 1 and processed the line-cut data from the T_1 imaging spectra (Fig. E.8). The spectra clearly revealed the differences between the regions on the flake and off the flake.

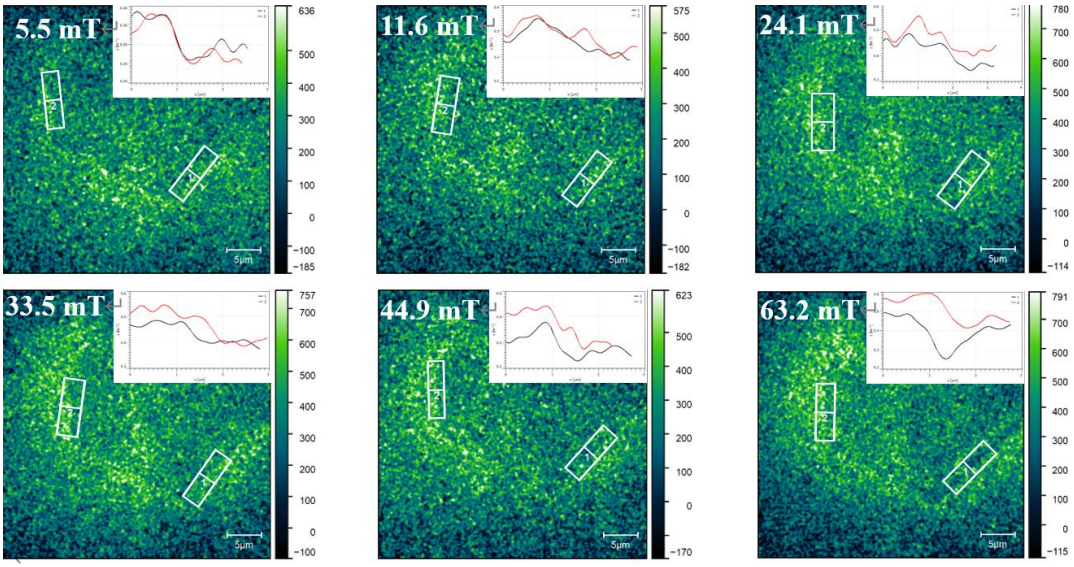

Fig. E.8. The T_1 imaging spectra with line-cut for f_- spin transition under different B_{ex} (Y axis unit: s^{-1}).

Similar to the NV magnetic maps, we recorded the $1/T_1$ value (ranging from 0.1 to 0.2 $\times 10^3$/s) at the edge of the WS_2 flake under external magnetic fields B_{ex} of 5.5 mT, 11.6 mT, 24.1 mT, 33.5 mT, 44.9 mT, and 63.2 mT, obtaining the same B_{ex} dependence spectra (Fig. E.9). However, we found that the T_1 imaging spectra were unclear, which affected the results. Therefore, we plan to repeat these measurements in future work.

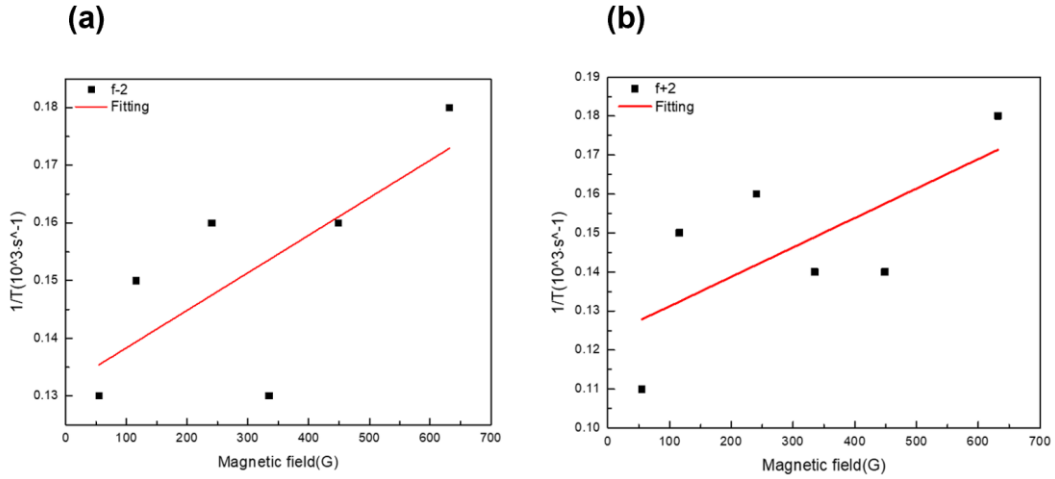

Fig. E.9. B_{ex} dependence of $1/T_1$ for f_- spin transitions from the edge of the WS_2 flake region 1.

E.4 Conclusion

The NV center technique, specifically NV-WFM, proved to be an effective method for detecting nanoscale magnetic fields, offering a powerful tool for future studies of 2D materials and their potential spintronic applications. This research successfully demonstrated the magnetic properties of WS_2 flakes using NV center magnetometry, providing experimental evidence of weak magnetic stray field (a few μT) in Fe-implanted WS_2 flakes. By conducting NV magnetic mapping and observing stray fields across various regions of the flakes under increasing external magnetic fields (5.5 mT to 63.2 mT), we confirmed the magnetic behavior predicted by theoretical models. Our analysis showed that the magnetic stray field strength increases with the applied external magnetic field, and the results align well with simulated magnetostatic models. Future work will involve improving the clarity of T_1 imaging spectra and further exploring the magnetic dynamics of WS_2.

Bibliography

[1] S. M. Salapaka, and M. V. Salapaka, IEEE Control Systems Magazine 28, no. 2: 65-83 (2008).

[2] K. Bian, C. Gerber, A. J. Heinrich, D. J. Müller, S. Scheuring and Y. Jiang, Nat. Rev. Methods Primer 1, 36 (2021).

[3] S. Liu, Y. Wang, Scanning, 32(2), pp.61-73 (2010).

[4] O. Kazakova, R. Puttock, C. Barton, H. Corte-León, M. Jaafar, V. Neu, and A. Asenjo, J. Appl. Phys. 125, 060901. (2019)

[5] G. Binning, H. Rohrer, C. Gerber, and E. Weibel, Phys. Rev. Lett. 49, 57. (1982)

[6] E. Marchiori, L. Ceccarelli, N. Rossi, L. Lorenzelli, C. L. Degen, and M. Poggio, Nat. Rev. Phys. 4, 49. (2022)

[7] D. Vasyukov, Y. Anahory, L. Embon, D. Halbertal, J. Cuppens, L. Neeman, A. Finkler, Y. Segev, Y. Myasoedov, M. L. Rappaport, M. E. Huber, and E. Zeldov, Nat. Nanotechnol. 8, 639. (2013)

[8] R. Wiesendanger, "Spin mapping at the nanoscale and atomic scale," Rev. Mod. Phys. 81, 1495. (2009)

[9] S.-W. Cheong, M. Fiebig, W. Wu, L. Chapon, and V. Kiryukhin, "Seeing is believing: Visualization of antiferromagnetic domains," npj Quantum Mater. 5, 3. (2020)

[10] Hung, T. Q.; Terki, F.; Kamara, S.; Dehbaoui, M.; Charar, S.; Sinha, B.; Kim, C.; Gandit, P.; Gural'skiy, I. A.; Molnar, G.; Salmon, L.; Shepherd, H. J.; Bousseksou, Angew. Chem., Int. Ed., 52 (4), 1185−1188. (2013)

[11] F. Casola, T. van der Sar, and A. Yacoby, "Probing condensed matter physics with magnetometry based on nitrogen-vacancy centres in diamond," Nat. Rev. Mater. 3(1), 17088. (2018)

[12] T. Hache, A. Anshu, T. Shalomayeva, G. Richter, R. Stöhr, K. Kern, and A. Singha, Nano Lett. 25, 5. (2024)

[13] G. Balasubramanian, I. Y. Chan, R. Kolesov, M. Al-Hmoud, J. Tisler, C. Shin, C. Kim, A. Wojcik, P. R. Hemmer, A. Krueger, T. Hanke, A. Leitenstorfer, R. Bratschitsch, F. Jelezko, and J. Wrachtrup, Nature 455, 648. (2008)

[14] H. J Mamin, M. Kim, M. H. Sherwood, C. T. Rettner, K. Ohno, D. D. Awschalom, and D. Rugar, Science, 339(6119), 557-560. (2013)

[15] F. Dolde1, H. Fedder1, M. W. Doherty, T. Nöbauer, F. Rempp, G. Balasubramanian, T. Wolf, F. Reinhard, L. C. L. Hollenberg, F. Jelezko and J. Wrachtrup, Nature Physics, Volume 7, Issue 6, pp. 459-463. (2011)

[16] G. Liu and X. Pan, Chinese Phys. B 27 020304. (2018)

[17] I. V. Soldatov, J. Zehner, K. Leistner, T. Kang, D. Karnaushenko, and R. Schäfer. Journal of Magnetism and Magnetic Materials 529: 167889. (2021)

[18] P. Maletinsky, S. Hong, M. S. Grinolds, B. Hausmann, M. D. Lukin, R-L. Walsworth, M. Loncar, and A. Yacoby, arXiv preprint arXiv:1108.4437. (2011)

[19] K. Wagner, A. Kákay, K. Schultheiss, A. Henschke, T. Sebastian, and H. Schultheiss, Nat. Nanotechnol, vol. 11, no. 5, pp. 432-436. (2016)

[20] A. Finco, A. Haykal, R. Tanos, et al, Nat Commun 12, 767. (2021)

[21] Y. Dovzhenko, F. Casola, S. Schlotter, T. X. Zhou, F. Büttner, R. L. Walsworth, and A. Yacoby, Nature communications, 9(1), 2712. (2018)

[22] R. Schirhagl, K. Chang, M. Loretz, and C. L.Degen, Annual review of physical chemistry, 65(1), 83-105. (2014)

[23] S. Hong, M. S.Grinolds, L. M Pham, D. Le Sage, L. Luan, R. L. Walsworth, and A. Yacoby, MRS bulletin, 38(2), 155-161. (2013)

[24] Website: https://qnami.ch/ for Qnami company.

[25] Q. Sun, et al., Nature Communications, 12, No. 1. (2021)

[26] A. Finco, et al., Nature Communication, 12, 767. (2021)

[27] B. G. Konoplev, O. A. Ageev, V. A. Smirnov, A. S. Kolomiitsev, and N. I. Serbu, Russ. Microelectron. 41, 41. (2012)

[28] W. R, McKenzie, et al., Diam. Rel. Matter. 20, 1125. (2011)

[29] C. J. Widmann, C. Giese, M. Wolfer, D. Brink, N. Heidrich, C. E. Nebel,Diamond and Related Materials,Volume 54. (2015)

[30] W. H. Bragg, W. L. Bragg, Proceedings of the Royal Society of London. Series A, Containing Papers of a Mathematical and Physical Character, 89(610), 277-291. (1913)

[31] G. Adam, F. Maria and K. Efthimios, Phys. Rev. B, vol 77,15. (2008)

[32] B. Chen, et al., *Nano Letters,* 20.11: 8267-8272. (2020)

[33] S. Felton, A. M. Edmonds, M. E. Newton, P. M. Martineau, D. Fisher, and D. J. Twitchen, Phys. Rev. B - Condens. Matter Mater. Phys. , vol. 77, no. 8. (2008)

[34] S. Benjamin, C. Lilian, and G. Adam, New J. Phys. **13** 025021. (2011)

[35] V. Ivády, T. Simon, J. R. Maze, I. A. Abrikosov, and A. Gali, Physical Review B, 90(23), 235205. (2014)

[36] A. Gruber, A. Drabenstedt, C. Tietz, L. Fleury, J. Wrachtrup, C. von Borczyskowski, Science 276, 2012 (1997).

[37] A. V. Zvyagin, and N. B. Manson,Nanodiamonds, and Proximity to Surfaces. In O. A. Shenderova, & D. M. Gruen (Eds.), Ultrananocrystalline Diamond: Synthesis, Properties and Applications: Second Edition 2nd ed., pp. 327-354. (2012)

[38] G. Adam, Nanophotonics, vol. 8, no. 11, 2019, pp. 1907-1943. (2019)

[39] L. Robledo, H. Bernien, T. van der Sar and R. Hanson, New J. Phys. 13, 025013 (2011).

[40] J. Kohler,Physics Reports,Volume 310, Issues 5–6. (1999)

[41] L. J. Rogers, S. Armstrong, M. J. Sellars, and N. B. Manson, New J. Phys. , vol. 10, (2008)

[42] Gu, L., Fang, H., Li, J., Fang, L., Chua, S. J., Zhao, J.,and Gan, X, Nanophotonics, *8*(5), 841-848. (2019)

[43] R. Schirhagl, K. Chang, M. Loretz, C. L. Degen, Annual Review of Physical

Chemistry. (2014)

[44] Dolde, F., Fedder, H., Doherty, M. et al, Nature Phys **7**, 459–463. (2011)

[45] I. Duck, W. Pauli, and E. C. G. Sudarshan, World Scientific. (1997)

[46] G. G. Scott, Rev. Mod. Phys., vol. 34,1. (1962)

[47] V. M. Acosta, E. Bauch, M. P. Ledbetter, A. Waxman, L. S. Bouchard, and D. Budker, Phys. Rev. Lett. vol. 104. (2010)

[48] M. W. Doherty et al., Phys. Rev. Lett., vol. 112. (2014)

[49] T. Mittiga et al., Phys. Rev. Lett. 121, no. 24. (2018)

[50] A. Z. Chaudhry, Physical Review A, 91(6), 062111. (2015)

[51] T. Lu, X. Miao, and H. Metcalf, Physical Review A—Atomic, Molecular, and Optical Physics, 71(6), 061405. (2005)

[52] I. Glendinning, In QIA Meeting (pp. 3-18). (2005, February)

[53] T. H. Stievater, X. Li, D. G. Steel, D. Gammon, D. S. Katzer, Park, and L. J. Sham, Physical Review Letters, 87(13), 133603. (2001)

[54] H. Fedder, F. Dolde, F. Rempp, T. Wolf, P. Hemmer, F. Jelezko, and J. Wrachtrup, Appl. Phys. B 102, 497. (2011)

[55] N. B. Manson, J. P. Harrison, and M. J. Sellars, Phys. Rev. B 74, 104303 (2006).

[56] J. M. Choi, G. N. Kim, and D. Cho, Physical Review A—Atomic, Molecular, and Optical Physics, 77(1), 010501. (2008)

[57] Z. Q. Yin, T. Li, X. Zhang, and L. M. Duan, Physical Review A—Atomic, Molecular, and Optical Physics, 88(3), 033614. (2013)

[58] G. Balasubramanian, P. Neumann, D. Twitchen, M. Markham, R. Kolesov, N. Mizuochi, J. Isoya, J. Achard, J. Beck, J. Tissler, V. Jacques, P. Hemmer, F. Jelezko and J. Wrachtrup, Nat. Mater., 8, 383. (2009)

[59] M. Schlosshauer, Physics Reports, 831, 1-57. (2019)

[60] L. Cywinski, M. L. Roman, P. N. Cody and S. D. Sarma, Phys. Rev. B, vol 77, 17. (2008)

[61] C. L. Degen, F. Reinhard, and P. Cappellaro, Rev. Mod. Phys., vol 89, 3. (2017)

[62] J. F. Barry, J. M. Schloss, E. Bauch, M. J. Turner, C. A. Hart,L. M. Pham, and R. L. Walsworth, Rev. Mod. Phys. 92, 015004. (2000)

[63] G. D. Fuchs, V. V. Dobrovitski, D. M. Toyli, F. J. Heremans, C. D. Weis, T. Schenkel, and D. D. Awschalom, Nature Physics, 6(9), 668-672. (2010)

[64] T. Yamamoto, T. Umeda, K. Watanabe, S. Onoda, M. L. Markham, D. J. Twitchen, and J. Isoya, Physical Review B—Condensed Matter and Materials Physics, 88(7), 075206. (2013)

[65] A. O. Sushkov, N. Chisholm, I. Lovchinsky, M. Kubo, P. K. Lo, S. D. Bennett, D. Hunger, A. Akimov, R. L Walsworth, H. Park, M. D. Lukin, Nano Lett., 14 (11), 6443−6448. (2014)

[66] A. Jarmola, V. Acosta, K. Jensen, S. Chemerisov, and D. Budker, Physical review let ters, vol. 108, no. 19, p. 197601. (2012)

[67] Mzyk, A., Sigaeva, A., & Schirhagl, R. Relaxometry with nitrogen vacancy (NV) centers in diamond. Accounts of Chemical Research, *55*(24), 3572-3580. (2022)

[68] T. Rosskopf, A. Dussaux, K. Ohashi, M. Loretz, R. Schirhagl, H. Watan abe, S. Shikata, K. M. Itoh, and C. L. Degen, Phys. Rev. Lett. 112, 147602. (2014)

[69] C. Santori, P. E. Barclay, K. M. C. Fu, and R. G. Beausoleil, Phys. Rev. B 79, 125313. (2009)

[70] J. F. Ziegler, M. D. Ziegler and J. P. Biersack, Nucl. Instrum. Methods Phys. Res. Sect. B Beam Interact. Mater. At. 268,11–12. (2010)

[71] V. Petráková, A. Taylor, I. Kratochvílová, F. Fendrych, J. Vacík, J. Kučka, and M. Nesládek, Advanced Functional Materials, 22, 4. (2012)

[72] I. Bayn, A. Bolker, C. Cytermann, B. Meyler, V. Richter, J. Salzman and R. Kalish, Appl. Phys. Lett. 99, 18. (2011)

[73] B. G. Konoplev, O. A. Ageev, V. A. Smirnov, A. S. Kolomiitsev, and N. I. Serbu, Russ. Microelectron, 41, 41. (2012)

[74] J. P. Hadden, J. P. Harrison, A. C. Stanley-Clarke, L. Marseglia, Y.-L. D. Ho, B. R. Patton, J. L. O'Brien and J. G. Rarity, Appl. Phys. Lett. 97, 24. (2010)

[75] Y. Kainuma, K. Hayashi, C. Tachioka, M. Ito, T. Makino, N. Mizuochi and T. An, J. Appl. Phys. 130, 24. (2021)

[76] R. Wirth, Chemical Geology, 261(3-4), 217-229. (2009)

[77] S. Rubanov, A. Suvorova, V. P. Popov, A. A. Kalinin and Yu. N. Pal'yanov, Diam. Relat. Mater. 63, 143 (2016).

[78] I. Bayn, B. Meyler, J. Salzman and R. Kalish, New J. Phys. 13, 2. (2011)

[79] Y. Wang, Y. Yang, J. Qu, and C. Cui, International Journal of Electrochemical Science, 19(2), 100451. (2024)

[80] C.J. Widmann, C. Giese, M. Wolfer, D. Brink, N. Heidrich, C.E. Nebel, Diamond and Related Materials, vol 54. (2015)

[81] H. Uetsuka, T. Yamada, S. Shikata, Diam. Relat. Mater., 17, 728. (2008)

[82] S. Xiao, P. Xiao, X. Zhang, D. Yan, X. Gu, F. Qin, and K. Ostrikov, Scientific reports, 6, 1. (2016)

[83] Y. Kato, H. Kawashima, T. Makino, M. Ogura, A. Traoré, N. Ozawa, and S. Yamasaki, Phys. Status Solidi A. (2017)

[84] T. Mittiga, S. Hsieh, C. Zu, B. Kobrin, F. Machado, P. Bhattacharyya, N. Z. Rui, A. Jarmola, S. Choi, D. Budker, and N. Y. Yao, Phys. Rev. Lett., vol121,24. (2018)

[85] K. Sasaki, Y. Monnai, S. Saijo, R.Fujita, H. Watanabe, J. Ishi-Hayase, K. M. Itoh, and E. Abe; Rev. Sci. Instrum., 87, 5. (2016)

[86] F. J. Giessibl, F. Pielmeier, T. Eguchi, T. An, and Y. Hasegawa, Physical Review B-Condensed Matter and Materials Physics, 84, 12. (2011)

[87] T. An, T. Nishio, T. Eguchi, M. Ono, A. Nomura, K. Akiyama, and Y. Hasegawa, Rev. Sci. Instrum. 79 (2008).

[88] H. Hida, M. Shikida, K. Fukuzawa, S. Murakami, Ke. Sato, K. Asaumi, Y. Iriye, and Ka. Sato, Sensors and Actuators A: Physical, vol. 148, 1. (2008)

[89] P. Maletinsky, S. Hong, M. S. Grinolds, B. Hausmann, M. D. Lukin, R. L. Walsworth, M. Loncar, and A. Yacoby, Nat. Nanotechnol. 7, 320 (2012).

[90] A. Stupakiewicz, A. Chizhik, M. Tekielak, A. Zhukov, J. Gonzalez, and A. Maziewski, Review of Scientific Instruments, 85, 10. (2014)

[91] I. V. Soldatov, J. Zehner, K. Leistner, T. Kang, D. Karnaushenko, and R. Schäfer, Journal of Magnetism and Magnetic Materials, 529. (2021)

[92] I. Kornev, H. Fu, and L. Bellaiche, Phys. Rev. Lett. vol 93, 19. (2004)

[93] H. Edwards, L. Taylor, W. Duncan, and A. J. Melmed, Journal of applied physics, 82, 3. (1997)

[94] J-P. Tetienne, L. Rondin, P. Spinicelli, M. Chipaux, T. Debuisschert, J-F. Roch, and V. Jacqueset, New J. Phys. 14. (2012)

[95] A. Kuwahata, T. Kitaizumi, et al., Scientific Reports. 10. (2020)

[96] V. P. Ningrum, B. Liu, W. Wang et al., Research, 1768918. (2020)

[97] K. S. Novoselov et al., Science, 306, 666-669. (2004)

[98] K. S. Novoselov et al., Science, 353, aac9439. (2016)

[99] C. Lan, et al., Advanced Electronic Materials, 7.7, 2000688. (2021)

[100] X. Mao, Y. Xu, Q. Xue, et al., Nanoscale Research Letters, 8, 430. (2013)

List of publication

Journals

1. **Y. Wang**, D. Prananto, K. Hayashi, and T. An, Effective removal of focused ion beam-induced damage in diamond nitrogen-vacancy pillar probes via inductively coupled plasma etching. (Accepted by Japanese Journal of Applied Physics (regular paper))

2. D. Prananto, **Y. Wang**, Y. Kainuma, K. Hayashi, M. Tomitori, and T. An, Spin properties recovery of a focused ion beam-fabricated scanning nitrogen-vacancy probe via ultraviolet/ozone treatment. (Submitted to APL Materials)

3. T. Gas-Osoth, **Y. Wang**, R. Kumar, S. Lamichhane, I. Fescenko, T. Li, T. Delord, A. Erickson, C. Cress, J. F. Vega, S. Liou, X. Hong, T. An, C. A. Meriles, and A. Laraoui, Nitrogen-vacancy Magnetometry of Weak Ferromagnetism in Pristine WS_2 Flakes. (In preparation)

Academic conference

1. Yifei Wang, Dwi Prananto, Kunitaka Hayashi, Toshu An, Position dependence of ODMR spectra imaging by NV center diamond probe, JAIST International Symposium of Nanomaterials and Devices Research Area, KS Lecture Hall, JAIST, Ishikawa, Japan, Dec. 14, 2022. (Poster Presentation)

2. Yifei Wang, Dwi Prananto, Kunitaka Hayashi, Toshu An, Optimization of scanning diamond NV center probes fabricated by using FIB, the 9th International Symposium on Organic and Inorganic Electronic Materials and Related Nano technologies (EM-NANO 2023), Ishikawa Industrial Promotion Center, Kanazawa, Japan, June 5-8, 2023. (Oral Presentation)

3. Yifei Wang, Dwi Prananto, Kunitaka Hayashi, Toshu An, Stray field imaging via diamond NV center probes fabricated by using Focused Ion Beam, International Symposium on Nano-Materials for Novel Devices (JAIST-NMND2023), Kanazawa

Chamber of Commerce and Industry Hall, Kanazawa, Japan, Jan. 12, 2024. (Poster Presentation)

4. Yifei Wang, Dwi Prananto, Kunitaka Hayashi, Toshu An, Bubble domain imaging via scanning NV center probe microscope, the 85th JSAP Autumn Meeting 2024, TOKI MESSE Niigata Convention Center, Niigata, Japan, Sept. 16-20, 2024. (Poster Presentation)